

UNCLASSIFIED

AD NUMBER: AD0883521

LIMITATION CHANGES

TO:

Approved for public release; distribution is unlimited.

FROM:

Distribution authorized to US Government Agencies and their contractors; Administrative/Operational Use; 1 Dec 1964. Other requests shall be referred to US Air Force, Washington, DC 20330.

AUTHORITY

DAC ltr dtd 9 Apr 1974

AD883521

**COMPARISON OF EXPERIMENTAL PRESSURE DISTRIBUTIONS WITH
THOSE CALCULATED BY THE DOUGLAS NEUMANN PROGRAM**

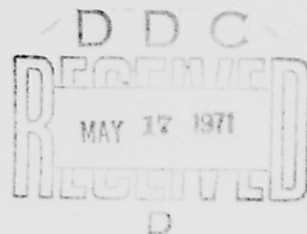
By

**Sue Faulkner, John L. Hess, and
Joseph P. Giesing**

Report No. LB 31831

1 December 1964

**This report summarizes work performed at the Aircraft Division
under sponsorship of the Independent Research and Development
Program of Douglas Aircraft Company, Inc.**



MCDONNELL DOUGLAS 

COMPARISON OF EXPERIMENTAL PRESSURE DISTRIBUTIONS WITH
THOSE CALCULATED BY THE DOUGLAS NEUMANN PROGRAM

By

Sue Faulkner, John L. Hess, and
Joseph P. Giesing

Report No. LB 31831

1 December 1964

This report summarizes work performed at the Aircraft Division
under sponsorship of the Independent Research and Development
Program of Douglas Aircraft Company, Inc.



2.0 TABLE OF CONTENTS

	<u>Page No.</u>
1.0 Abstract	1
2.0 Table of Contents	2
3.0 Index of Figures	3
4.0 Introduction	9
5.0 Axisymmetric Bodies at Zero Angle of Attack	12
5.1 Single Closed and Semi-Infinite Bodies	12
5.2 Inlets and Propeller Shrouds	13
5.3 Bodies at High Subsonic Mach Number	13
6.0 Axisymmetric Bodies at Angle of Attack	15
6.1 Single Semi-Infinite Bodies	15
6.2 Inlets and Cowlings	17
6.3 Bodies at High Subsonic Mach Number	18
7.0 Two-Dimensional Lifting Airfoils	19
7.1 Single Airfoil	20
7.2 Multiple Airfoils	20
7.3 Correction for Viscous Effects	21
7.4 Airfoils at High Subsonic Mach Number	22
7.5 Infinite Cascades of Airfoils	23
7.6 Hydrofoils. Motion beneath a Free Surface	23
8.0 Three-Dimensional Bodies	24
8.1 Single Closed and Semi-Infinite Bodies	24
8.2 Intersecting Wings	26
8.3 Fuselage-Pylon-Nacelle Interference	26
8.4 Destroyer Sonar Dome	27
8.5 Interference at High Subsonic Mach Number. Wing-Fuselage and Wing-Pylon-Nacelle	27
9.0 References	30

3.0 INDEX OF FIGURES

<u>No.</u>	<u>Title</u>	<u>Page No.</u>
1.	Comparison of calculated and experimental pressure distributions on a sharp and a blunted cone-cylinder.	32
2.	Comparison of calculated and experimental pressure distributions on two ogive-cylinders.	33
3.	Comparison of calculated and experimental pressure distributions on two blunted ogive-cylinders.	34
4.	Comparison of calculated and experimental velocity distributions on a flat-nosed body.	35
5.	Comparison of calculated and experimental velocity distributions on a prolate spheroid with an annular bump.	36
6.	Comparison of calculated and experimental pressure distributions on the exteriors of two inlet lips at finite mass-flow ratios.	37
7.	Comparison of calculated and experimental pressure distributions on a propeller shroud with centerbody in static operation.	38
8.	Comparison of calculated and experimental pressure distributions on a propeller shroud with dual rotation propeller in static operation.	39
9.	Comparison of calculated and experimental pressure distributions on a parabolic-arc body with a bump for a Mach number of 0.8.	40
10.	Comparison of calculated and experimental pressure distributions on a parabolic-arc body with a bump for a Mach number of 0.9.	41
11.	Comparison of calculated and experimental pressure distributions on a parabolic-arc body with a bump for a Mach number of 0.95.	42
12.	Comparison of calculated and experimental pressure distributions on an indented parabolic-arc body for a Mach number of 0.8.	43

<u>No.</u>	<u>Title</u>	<u>Page No.</u>
13.	Comparison of calculated and experimental pressure distributions on an indented parabolic-arc body for a Mach number of 0.9.	44
14.	Comparison of calculated and experimental pressure distributions on an indented parabolic-arc body for a Mach number of 0.95.	45
15.	Comparison of calculated and experimental velocity distributions on a prolate spheroid of fineness ratio 6 for various Mach numbers.	46
16.	Comparison of calculated and experimental pressure distributions on a Skybolt missile at a Mach number of 0.8.	47
17.	Comparison of calculated and experimental circumferential pressure distributions on an ogive-cylinder at angle of attack.	48
18.	Comparison of calculated and experimental circumferential pressure distributions on an ellipsoid-cylinder at angle of attack.	49
19.	Comparison of calculated and experimental pressure distributions on a 15° cone-cylinder at 0° and 20° angle of attack.	50
20.	Comparison of calculated and experimental pressure distributions on a blunted 15° cone-cylinder with nose radius equal to one-fourth final radius at 0° and 20° angle of attack.	51
21.	Comparison of calculated and experimental pressure distributions on a blunted 15° cone-cylinder with nose radius equal to one-half final radius at 0° and 20° angle of attack.	52
22.	Comparison of calculated and experimental pressure distributions on a 30° cone-cylinder at 0° and 20° angle of attack.	53
23.	Comparison of calculated and experimental pressure distributions on a blunted 30° cone-cylinder with nose radius equal to one-fourth final radius at 0° and 20° angle of attack.	54
24.	Comparison of calculated and experimental pressure distributions on a blunted 30° cone-cylinder with nose radius equal to one-half final radius at 0° and 20° angle of attack.	55

<u>No.</u>	<u>Title</u>	<u>Page No.</u>
25.	Comparison of calculated and experimental pressure distributions at various circumferential locations on a 30° cone-cylinder at 20° angle of attack.	56
26.	Comparison of calculated and experimental circumferential pressure distributions on a 30° cone-cylinder at 20° angle of attack.	57
27.	Comparison of calculated and experimental pressure distributions on the exterior of an inlet lip at 6° angle of attack for a mass flow ratio of 0.44.	58
28.	Comparison of calculated and experimental pressure distributions on the exterior of an inlet lip at 6° angle of attack for a mass flow ratio of 0.52.	59
29.	Comparison of calculated and experimental pressure distributions on the exterior of an inlet lip at 6° angle of attack for a mass flow ratio of 0.73.	60
30.	Comparison of calculated and experimental pressure distributions at 6° angle of attack on an NACA 1-60-060 spinner in an NACA 1-70-100 cowling.	61
31.	Comparison of calculated and experimental pressure distributions at 6° angle of attack on an NACA 1-40-060 spinner in an NACA 1-70-100 cowling.	62
32.	Comparison of calculated and experimental circumferential pressure distributions at two Mach numbers on a slender body at angle of attack. $x/L = 0.017$.	63
33.	Comparison of calculated and experimental circumferential pressure distributions at two Mach numbers on a slender body at angle of attack. $x/L = 0.100$.	64
34.	Comparison of calculated and experimental pressure distributions on a DSMA 387 airfoil at $C_L = 1.0765$.	65
35.	Comparison of calculated and experimental pressure distributions on an NACA 23012 airfoil with fixed slot and deflected slotted flap at angle of attack. Flap deflection 20°, angle of attack 0°.	66

<u>No.</u>	<u>Title</u>	<u>Page No.</u>
36.	Comparison of calculated and experimental pressure distributions on an NACA 23012 airfoil with fixed slot and deflected slotted flap at angle of attack. Flap deflection 20° , angle of attack 8° .	67
37.	Comparison of calculated and experimental pressure distributions on an NACA 23012 airfoil with a deflected external 23012 airfoil flap. Flap deflection 30° , angle of attack -4.02° .	68
38.	Comparison of calculated and experimental pressure distributions on an NACA 23012 airfoil with a deflected external 23012 airfoil flap. Flap deflection 30° , angle of attack -9.42° .	69
39.	Comparison of calculated and experimental pressure distributions on an 11.8 percent thick symmetric Joukowski airfoil at 6° angle of attack.	70
40.	Comparison of calculated and experimental pressure distributions on a DSMA 299 symmetric airfoil at 0° angle of attack and at a Mach number of 0.680.	71
41.	Comparison of calculated and experimental pressure distributions on a DSMA 299 symmetric airfoil at 0° angle of attack and at a Mach number of 0.757.	72
42.	Comparison of calculated and experimental pressure distributions on a horizontal tail with deflected elevator at a lift coefficient of -0.07 and Mach number of 0.5.	73
43.	Geometrical arrangement of a typical infinite cascade showing stagger angle and an inlet angle of attack of 30° .	74
44.	Comparison of calculated and experimental pressure distributions on a symmetrical NACA 65-010 airfoil in cascade at an inlet angle of attack of 30° and stagger angle of -33° .	75
45.	Comparison of calculated and experimental pressure distributions on a symmetrical NACA 65-010 airfoil in cascade at an inlet angle of attack of 30° and stagger angle of -15° .	76

<u>No.</u>	<u>Title</u>	<u>Page No.</u>
46.	Comparison of calculated and experimental pressure distributions on a 12 percent thick symmetric Joukowski hydrofoil at 5° angle of attack, Froude number of 0.95 and a depth of 1 chord. Depth measured from trailing edge.	77
47.	Comparison of calculated and experimental pressure distributions on a 12 percent thick symmetric Joukowski hydrofoil at 5° angle of attack, Froude number of 0.95 and a depth of 1.8 chord. Depth measured from trailing edge.	78
48.	Comparison of calculated and experimental isobars on Wing A at zero lift.	79
49.	Comparison of calculated and experimental isobars on Wing B at zero lift.	80
50.	Comparison of calculated and experimental isobars on Wing C at zero lift.	81
51.	Comparison of calculated and experimental spanwise pressure distributions on Wing A at zero lift.	82
52.	Comparison of calculated and experimental spanwise pressure distributions on Wing B at zero lift.	83
53.	Comparison of calculated and experimental spanwise pressure distributions on Wing C at zero lift.	84
54.	Comparison of calculated and experimental pressure distributions on the aft end of a clean DC-9 fuselage.	85
55.	Comparison of calculated and experimental pressure distributions on a nonlifting symmetric 10 percent thick wing which intersects a nonlifting symmetric 20 percent thick wing.	86
56.	Comparison of calculated and experimental pressure distributions on a nonlifting symmetric 20 percent thick wing which intersects a nonlifting symmetric 10 percent thick wing.	87
57.	Comparison of calculated and experimental pressure distributions on a DC-9 pylon in the presence of the fuselage and nacelle.	88
58.	Destroyer sonar dome showing orifice location.	89

<u>No.</u>	<u>Title</u>	<u>Page No.</u>
59.	Comparison of calculated and experimental pressure distributions in the symmetry plane of a destroyer sonar dome.	90
60.	Comparison of calculated and experimental pressure distributions along the maximum horizontal section of a destroyer sonar dome.	91
61.	Comparison of calculated and experimental isobars on an NACA wing mounted on a fuselage at zero lift for a Mach number of 0.6.	92
62.	Comparison of calculated and experimental pressure distributions at three spanwise locations on an NACA wing mounted on a fuselage at zero lift for a Mach number of 0.6.	93
63.	Calculated two-dimensional pressure distributions on a 6 percent thick symmetric airfoil at zero lift.	94
64.	Adjusted DC-8 wing-pylon-nacelle combination.	95
65.	Comparison of calculated and experimental pressure distributions on a DC-8 nacelle in the presence of the pylon and wing at a Mach number of 0.825 for the zero-lift condition.	96
66.	Comparison of calculated and experimental pressure distributions on a DC-8 pylon in the presence of the nacelle and wing at a Mach number of 0.825 for the zero-lift condition.	97

4.0 INTRODUCTION

The Douglas Neumann Program is actually a set of digital computer programs that can calculate with high accuracy the potential flow about arbitrary body shapes under a variety of flow conditions. The various aspects of the method are described in references 1, 2, 3, 4, and 5. The various component programs handle different geometrical situations: axisymmetric bodies at zero or nonzero angle of attack; two-dimensional lifting airfoils, including infinite cascades and hydrofoils moving beneath a free surface; and truly three-dimensional bodies. Lift can be accounted for only in two-dimensional cases.

At various times the results of calculations performed by the present method have been compared with experimental data. Such comparisons were made both by the authors who developed the method and by others who were interested in using the method for design purposes. These latter include both Douglas personnel and personnel of other agencies. Such comparisons are severe tests of the usefulness of the present method, because they determine not only how accurately potential flow is calculated but also how well potential flow agrees with real flow. The examples presented here show good agreement between calculated and experimental results for a number of rather extreme body shapes under a variety of flow conditions. Thus the usefulness of the Douglas Neumann Program as a design tool is exhibited. The comparisons also show that in many situations of interest the effects of viscosity and compressibility may either be ignored or taken into account in a simple way.

As a result of comparing the calculations with experiment, it is concluded that for ordinary aircraft and marine applications viscosity has a negligible effect on the surface pressure distribution except in or near regions of catastrophic separation. Local regions of separation and reattachment do not significantly affect the pressure distribution. This is illustrated by several examples in this report for which calculated and experimental pressure distributions agree despite the presence of obvious local separation. Even on bodies where catastrophic separation does occur, examples of which are the axisymmetric bodies at angles of attack up to 20° shown in Section 6.0,

the pressure distribution on the portion of the body ahead of the separation point is not greatly affected. The method can be refined by using the calculated pressure distribution to obtain the boundary-layer displacement thickness, which is then added to the body shape (including an assumed wake if desired) and the calculation repeated. In nonlifting cases, this procedure is straightforward, but it is rarely necessary, and it was not done for any of the examples shown in this report. In lifting cases, the procedure is somewhat more complicated, as described in Section 7.0. A single example of the use of this refinement is given in that section.

For the types of bodies encountered in aircraft applications, compressibility effects may be safely ignored for free-stream Mach numbers below about 0.3 or 0.4. For higher Mach numbers, the calculations still agree with experiment if a suitable compressibility correction is used. In axisymmetric and three-dimensional cases the well-known Göthert transformation is used to account for compressibility. For axisymmetric bodies at angle of attack, Mach number effects on the cross-flow terms are ignored, and the axial component of the flow is handled in the same manner as an axisymmetric flow. Two-dimensional lifting flows use other Mach number corrections, as described in Section 7.0. If these corrections are used, the calculated and experimental pressure distributions agree for all entirely subsonic flows. That is, the method gives good results except near stagnation points for all free-stream Mach numbers that do not give rise to local regions of supersonic flow. This is illustrated by several examples in this report.

The remaining sections of this report present graphical comparisons of calculated and experimental pressure distributions with brief discussions of the results. All pressures are presented in terms of pressure coefficient C_p . Some of the comparisons are rather similar and may seem repetitious. Such cases were included for completeness. This report contains essentially every comparison of the calculations of the Douglas Neumann Program with experiment that has ever been made. The examples have not been selected to show the method in a favorable light.

The calculations have been compared with analytic solutions in references 1, 2, and 3. Any disagreement between the two is always far less than plotting accuracy for two-dimensional and axisymmetric bodies, while for ordinary three-dimensional bodies the errors in the calculations are barely plottable. Thus at low speeds any disagreement between calculated and experimental pressure distributions is due to the non-potential nature of the real flow. At higher speeds the compressibility correction is an additional source of error.

Wind tunnel walls are not taken into account in any of the calculations. The experimental data may or may not have been corrected for such effects.

Reference 6 was a report similar to this one. It presented all comparisons of calculated and experimental pressure distributions that were available in May, 1960. This report contains all the examples of reference 6 plus all comparisons that have been made since that time. Thus this report replaces reference 6.

5.0 AXISYMMETRIC BODIES AT ZERO ANGLE OF ATTACK

The majority of examples shown in this section exhibit pressure distributions of rather extreme nature. Thus they provide severe tests of the present method, and also they represent configurations to which ordinary flow-calculation methods cannot be applied.

5.1 Single Closed and Semi-Infinite Bodies

Figure 1 shows calculated and experimental pressure distributions on a sharp and on a blunted cone-cylinder. Even though both bodies have sharp corners, the present method accurately predicts experimental pressures, even in the vicinity of the corners. Figures 2 and 3 show calculated and experimental pressure distributions on two ogive-cylinders for both sharp and blunted configurations. The blunted configurations of figures 1 and 3 illustrate the fact that in some cases pressure distributions calculated by the present method may actually be superior to experimental ones. Since the calculations agree with the data everywhere there are data points, it seems reasonable to conclude that the magnitudes of the calculated forward pressure peaks for the blunted configurations are also correct. These peaks were missed by the tests simply because there were no pressure orifices at the proper locations. The data of figures 1, 2, and 3 were obtained in the Douglas Aircraft Company El Segundo Division Low Speed Wind Tunnel.

Figure 4 compares calculated and experimental velocity distributions on a flat-nosed body of revolution consisting of a flat disk followed by a streamline fairing. The body is cavitation model D-116 of David Taylor Model Basin, and the data were taken from reference 7. (Figures 4, 5, and 15 show velocity distributions. All other figures show pressure distributions.)

Reference 8 contains the experimental velocity distribution on a body of revolution consisting of a prolate spheroid with an annular bump. Figure 5 compares this velocity distribution with those computed by two methods: the present method and a conventional flow-calculation method described in reference 9. The conventional method breaks down completely for this case,

but the present method agrees very closely with experiment.

5.2 Inlets and Propeller Shrouds

Inlets and propeller shrouds are special cases, because it is necessary to specify the flow through them, i.e., the mass-flow ratio. To accomplish this, the present method calculates the flow about an altered configuration consisting of the desired inlet or shroud lip shape followed by a semi-infinite afterbody (having constant inner and outer final diameters). Despite the necessary alteration of the body shape, the calculated results are quite satisfactory. In fact, inlets represent the type of body that occurs most frequently in design applications of the present method.

Comparisons of calculated and experimental pressure distributions on the exteriors of two inlet lips are shown in figure 6. A sketch of the second inlet lip is given in the figure. In both cases distance is measured from the front of the lip. The mass-flow ratios are labeled MFR. The tests were conducted in the Douglas Aircraft Company Santa Monica Division Low Speed Tunnel.

Figures 7 and 8 compare calculated and experimental pressure distributions on the forward portions of two propeller shrouds in static operation (infinite mass-flow ratio). The centerbody of the first shroud and the propeller shaft of the second shroud were accounted for in the calculations, but the propellers themselves were of course ignored. Distances are measured from the leading edges of the shrouds. Both shrouds have small chord-to-diameter ratios, but were calculated as semi-infinite bodies as described above. The agreement of calculated and experimental pressures on the inside and outside of both shrouds is good. The data of figure 8 were taken from reference 10, and those of figure 7 were obtained by Douglas personnel.

5.3 Bodies at High Subsonic Mach Number

Compressibility effects are accounted for by using a Göthert transformation. The calculated pressures appear to be accurate except near a stagnation point and in regions where the flow is locally supersonic.

Reference 11 presents the results of tests at high subsonic Mach number of certain slender bodies of revolution. The basic body was a parabolic-arc body of fineness ratio 14. Two additional bodies were tested. These were identical with the basic body except for a region around midchord whose length was equal to three maximum body diameters. In this region, one body was indented and the other expanded to form a bump. The indentation and the bump have similar shapes. The maximum deviation of diameter from the basic body was equal to one-fifth of the maximum diameter of the basic body. Tests were run at Mach numbers of 0.8, 0.9, and 0.95.

Comparisons of calculated and experimental pressure distributions for these Mach numbers are shown in figures 9, 10, and 11 for the body with a bump and in figures 12, 13, and 14 for the indented body. The value of pressure for which the flow is locally sonic is indicated by the horizontal line labeled " C_p for $M = 1.0$ ". Only for the Mach number of 0.8 is the flow subsonic everywhere. For this Mach number (figures 9 and 12) the differences between calculated and experimental pressures are less than the tunnel-wall effects discussed in reference 11. At the higher Mach numbers the agreement between calculated and experimental pressures is also good, except in the regions where the flow is actually supersonic. No doubt this is partly fortuitous, but it also reflects the fact that local effects are of chief importance in determining surface pressures.

Blunt bodies provide a more severe test of the validity of using the Göthert transformation with the present method than do pointed ones, because the region near the nose where the perturbation velocity is not small is much larger. Calculated pressures near the stagnation point are meaningless, but are usually quite good over the remainder of the body where the perturbation velocity is not too large. A usable result is obtained by fairing the calculated pressures to the known pressure at the stagnation point. Figure 15 compares calculated and experimental pressure distributions on a prolate spheroid of fineness ratio 6. The data were taken from reference 8. As an example of a pressure distribution with more character, figure 16 shows the calculated and experimental pressure distributions on a Skybolt missile at a Mach number of 0.8. The agreement is good even near the corners. The data of figure 16 were obtained in the Douglas Aircraft Company Aerophysics Laboratory.

6.0 AXISYMMETRIC BODIES AT ANGLE OF ATTACK

The flow about axisymmetric bodies at angle of attack always separates somewhere on the body, and accordingly it might be expected that the present method of flow calculation would not give useful results for such cases. However, it has been found that calculated and experimental pressure distributions agree quite satisfactorily forward of the separation point. It is also remarkable how large the angle-of-attack effect on the pressure may be in some cases.

The present method calculates a pure crossflow (90° angle of attack) about the body in question and combines this with the axisymmetric flow (zero angle of attack) to obtain the flow at any angle of attack. The calculated crossflow may be combined with either the calculated or the experimental axisymmetric flow. In some of the following comparisons, experimental zero angle-of-attack pressure distributions were used with the calculated crossflow, and in others calculated zero angle-of-attack pressure distributions were used. In view of the agreement of calculation and experiment shown in Section 5.0, it does not appear to matter which is used.

For some bodies, data were available for several angles of attack. In such cases, the data at the largest angle of attack were selected for comparison with the calculations.

6.1 Single Semi-Infinite Bodies

Figure 17 compares experimental pressure distributions on an ogive cylinder at angle of attack with those calculated by the present method and also with those calculated by linear theory. Figure 18 gives a similar comparison for an ellipsoid-cylinder. In both cases pressures are plotted versus circumferential angle measured from the upper (leeward) side of the body, and comparisons were made at two axial locations: 25 percent of the nose length from the front and 100 percent of the nose length at the start of the constant-diameter section. The experimental zero angle-of-attack pressure, which is simply a constant for each body at each axial location, was used with both calculated cross-flows.

It is evident from these comparisons that the present method is considerably more accurate than linear theory. The data of figures 17 and 18 were taken from reference 12.

Reference 13 is the Master's Thesis of Mr. Wesley E. Johnson from the University of Washington. This thesis compared pressure distributions computed by the Douglas Neumann Program with experimental data for a series of sharp and blunted cone-cylinders at zero angle of attack and at plus and minus 20° angle of attack. This rather high angle of attack is an extreme test of the present method. Six configurations were tested: a 15° semi vertex-angle cone-cylinder with a pointed nose and with two blunt noses and a 30° semi vertex-angle cone-cylinder with a pointed nose and with two blunt noses. The blunt noses were spherical segments tangent to the basic conical nose. For each cone, one blunt nose had a radius of one-fourth the final radius of the body, and the other had a radius equal to one-half the final radius of the body. The cylindrical afterbody for all configurations had a length equal to 1.45 times its diameter. In the calculations, however, all bodies were assumed to be semi-infinite. This difference between the bodies tested and the bodies calculated leads to discrepancies between calculated and experimental pressures on the aft portions of the afterbodies, but its effect should be negligible over the nose regions. In the comparisons, the calculated zero angle-of-attack pressures are used with the calculated crossflow. Figures 19 through 24 compare calculated and experimental pressure distributions on the six configurations. Pressures are compared along the upper sides of the bodies at 0° , 20° , and -20° angles of attack (except for figure 19, which has no data at 20° angle of attack). Thus comparisons are made on both the leeward and windward sides of the body, i.e., circumferential angles of 0° and 180° . In all cases agreement is good over the nose portions of the bodies at 0° and -20° angle of attack (windward side). For 20° angle of attack (leeward side), the agreement is also fairly good over the nose portions of the bodies, except in the case of figure 24. Undoubtedly, flow separation occurs on the leeward side at this high angle of attack. Agreement is less satisfactory over the afterbodies. On the forward portions of the afterbodies, effects of flow separation around the sharp corners are important; on the aft portion of the afterbodies the effect of the finite length of the bodies is significant.

Figure 25 compares calculated and experimental pressure distributions on the pointed 30° cone-cylinder for other circumferential locations at 20° angle of attack. Figure 26 compares calculated and experimental circumferential pressure distributions at two axial locations on the pointed 30° cone-cylinder at 20° angle of attack. The effect of separation on the leeward side at the more aft location can be seen. The following is a quotation from the author's conclusions in reference 13: "As a result of the correlation, it is seen that the theoretical method studied (Neumann Program of Douglas Aircraft Company) produces such excellent agreement with experiment that it seems to be unnecessary to perform wind tunnel tests on bodies of revolution when very low speed pressure distributions are desired. This could result in considerable savings in time and money."

6.2 Inlets and Cowlings

Tests were conducted in the Douglas Aircraft Company Santa Monica Division Low Speed Wind Tunnel on an inlet consisting of an NACA 1-70-100 cowling rounded to a constant inner diameter. Calculated and experimental pressure distributions were compared on the upper (leeward) side of the exterior surface of the inlet lip at 6° angle of attack. The comparisons are shown in figures 27, 28, and 29 for three different values of mass-flow ratio. The experimental zero angle-of-attack pressure distributions, which were used with the calculated crossflow, are also shown to exhibit the magnitude of the angle-of-attack effects. Agreement is good in all cases. The calculations correctly predict the presence of large negative pressure peaks at the two smaller mass-flow ratios and the absence of such a peak at the highest mass-flow ratio.

Reference 14 presents the results of wind-tunnel tests on a series of cowlings with spinners. Two of these were selected as examples of multiple-body problems. Figures 30 and 31 compare calculated and experimental pressure distributions on the upper (leeward) side of the two spinners at 6° angle of attack. Also shown are the body shapes and the zero angle-of-attack pressure distributions, which were used with the calculated crossflow. The calculated and experimental pressures are in good agreement. Over the forward portion of the spinners, the pressures at 6° angle of attack are more negative than those at 0° angle of attack, as would be expected on the upper side of a body. On the downstream portions of

the spinners, however, the effect of the cowlings reverses the situation, and the change of pressure dues to angle of attack is positive near the cowlings. This somewhat surprising behavior is accurately predicted by the present method.

6.3 Bodies at High Subsonic Mach Number

To calculate pressure distributions on bodies of revolution at angle of attack for Mach numbers at which compressibility effects are significant, the calculated incompressible crossflow is used with the zero angle-of-attack pressure distribution at the proper Mach number. This latter pressure distribution may be calculated or experimental. Reference 15 presents results of wind-tunnel tests on a body of fineness ratio 12 at various angles of attack. Figures 32 and 33 compare calculated and experimental circumferential pressure distributions on this body. Each figure shows results for two Mach numbers at one axial location along the body. The zero angle-of-attack pressure, which is simply a constant for each Mach number at each axial location, was used with the calculated crossflow.

7.0 TWO-DIMENSIONAL LIFTING AIRFOILS

Experimental and theoretical airfoil lift-curve slopes and pressure distributions at zero Mach number differ from each other because of the viscous boundary layer. The experimental lift-curve slope is always less than the theoretical. Thus for a given angle of attack, the experimental lift is always smaller than the theoretical, and the difference between the two increases as the angle of attack increases. The deviation of the experimental lift-curve slope from the theoretical varies from airfoil to airfoil making a generalized theoretical correction difficult to obtain. The experimentally obtained and theoretically calculated pressure distributions differ from each other in the region of the airfoil trailing edge. The deviation is due to the displacement-thickness effect of the boundary layer. This thickness becomes comparable to the airfoil thickness in the trailing edge region.

The question now arises as to how a valid pressure-distribution comparison can be obtained, when it is known that the theoretical lift-curve slope is incorrect and that the boundary layer will affect the pressure distribution at the trailing edge. For a single airfoil an effective approach in the elimination of the lift-curve slope error is to compare experimental and theoretical pressure distributions at equal values of lift rather than at equal angles of attack, thus eliminating the need for any knowledge of the lift curve slope. When this approach is used the boundary-layer displacement effect on the pressure distribution at the trailing edge is usually neglected. Likewise, for multiple airfoils it would be desirable to set each component (slat, airfoil, flap) at its experimental value of lift separately. However, this would ordinarily necessitate changes in flap and slat deflection. Any change in deflection would change the character of the pressure distribution thus defeating the primary purpose. Therefore for multiple airfoils comparisons must be made at equal angles of attack.

Another method of handling the two viscous effects is to simulate the effect of the boundary layer on the airfoil. This is done by first adding a boundary-layer displacement thickness to the airfoil and then applying the Kutta condition at the edge of the boundary layer at the trailing edge. This

procedure is very effective, as one of the examples will show. However, it is also very lengthy. The procedure was applied to a single isolated airfoil. (See figure 39.)

In addition to the viscous effects mentioned above, some special cases occur where the flow separates over a portion of the airfoil. In this case, the potential-flow model is not strictly applicable. Nevertheless, reasonable agreement is still obtained for the unseparated part of the airfoil if the separation region is small enough.

7.1 Single Airfoil

Shown in figure 34 is a comparison of the calculated and experimental pressure distributions on a DSMA 387 airfoil at a lift coefficient of 1.0765. The experimental data were taken from a three-dimensional model along a section located 40 percent of the semispan from the wing's plane of symmetry. The test was run by Douglas personnel at the Ames 12-foot wind tunnel.

As is noted on the figure, the experimental data and theoretical calculation are compared at the same lift coefficient and not at the same angle of attack.

The present method and experimental data show very good agreement except near the trailing edge. As is explained in Section 7.0, this is due to the effect of the boundary-layer displacement thickness in this region.

7.2 Multiple Airfoils

Shown in figures 35 and 36 are comparisons of calculated and experimental pressure distributions on an NACA 23012 airfoil with fixed slot and slotted flap at two angles of attack. The experimental data were obtained from reference 16. The slotted flap is deflected 20° .

The agreement in both figures is quite good except for the lower surface of the slat. At 0° angle of attack, and to a lesser extent at 8° , the flow is separated in this region. It can be seen from the geometrical arrangement

of the airfoil system illustrated in the upper right-hand corner of the figures that in both cases the slat is at a high negative angle of attack, indicating probable separation. The calculation also indicates that separation will occur here because of the sharp rise in predicted pressure. It should be noted that the slat, airfoil, and flap arrangement is given in the small drawing and not as shown below the pressure comparisons.

Figures 37 and 38 are comparisons of calculated and experimental pressure distributions on an NACA 23012 airfoil with an NACA 23012 external-airfoil flap at two angles of attack. The external-airfoil flap is at a deflection angle of 30° . The illustration in the upper section of the figure shows the configuration. The data were taken from reference 17. The comparisons show that this airfoil-flap configuration is inefficient. Viscous effects on the Kutta condition, as discussed in Section 7.0, have markedly reduced the lift on both the airfoil and the flap.

It can be seen that the calculated values follow the experimental data qualitatively, but indicate a lift that is too large.

7.3 Correction For Viscous Effects

Figure 39 shows a comparison of the calculated and experimental pressure distributions on an 11.8-percent-thick symmetric Joukowski airfoil at 6° angle of attack. The experimental data were obtained from reference 18. Experimental boundary-layers and wake characteristics were used for the calculation. Specifically, in the manner outlined in Section 7.0, the displacement thickness of the boundary layer was added to the basic Joukowski profile and the Kutta condition applied at the trailing edge at the outer edge of the boundary layer. The pressures were calculated at the edge of the boundary layer. Agreement with the experimental data is good, especially at the nose and trailing edge of the airfoil.

As was stated above, the experimental data and the theoretical calculations are compared at the same angle of attack and not at the same lift coefficient. In this case an attempt was made to eliminate the theoretical lift-curve-slope

error by simulating viscous effects on the airfoil. A measure of the success of this procedure is the difference in lift coefficients as obtained experimentally and as obtained by the present method. The experimental lift coefficient is 0.620 and the calculated lift coefficient is 0.602.

7.4 Airfoils at High Subsonic Mach Number

Figures 40 and 41 show comparisons of the calculated and experimental pressure distributions on a DSMA 299 symmetric airfoil tested at zero angle of attack and at Mach numbers of 0.680 and 0.757, respectively. The experimental data were obtained by Douglas personnel at the United Aircraft Corporation wind tunnel.

Since the present method calculates only incompressible flow, a modified Kármán-Tsien correction was applied to the incompressible pressure coefficient. The Kármán-Tsien correction was modified to give the correct relation between compressible and incompressible pressure coefficient at the stagnation point.

The comparisons of figures 40 and 41 show good agreement in the subcritical regions.

Tests were run in the Southern California Co-operative Wind Tunnel on a three-dimensional model of a horizontal tail with a deflected elevator. The elevator was a distinct body separated by a gap from the stationary portion of the horizontal tail. The tests were conducted at a Mach number of 0.5. For purposes of comparison with the calculations of the program, the three-dimensional effects were ignored, the pressures were transformed to zero Mach number by the method of Laitone, and the gap was eliminated by arbitrarily assuming a fairing between the elevator and the stationary portion of the horizontal tail. The comparison for one set of conditions is shown in figure 42. Despite all the approximations, the agreement is quite satisfactory.

7.5 Infinite Cascades of Airfoils

The present method for calculating the pressure distributions on isolated airfoils has been extended to calculate the flow about infinite cascades of airfoils. A typical cascade is shown in figure 43. The cascade capability is described in detail in reference 5.

Shown in figures 44 and 45 are calculated and experimentally obtained pressure distributions for an NACA 65-010 cascade blade at two values of stagger angle. The experimental data were taken from reference 19. The calculated and experimental distributions agree quite well, except for a small region near the trailing edge. The discrepancies near the trailing edge are probably due to the boundary-layer-thickness effects described in Section 7.0.

7.6 Hydrofoils. Motion Beneath a Free Surface

The Douglas Neumann Program is being extended to calculate the pressure distributions on hydrofoils in the presence of a free surface. It is assumed that the free surface is perturbed only slightly by the body.

Preliminary calculations are presented in figures 46 and 47. The figures show comparisons of calculated and experimental pressure distributions on a 12-percent thick Joukowski hydrofoil at two depths. The hydrofoil is running at a Froude number of 0.95, 5° angle of attack, and depths of 1 and 1.8 chords, respectively. The experimental data, taken from reference 20, were given only for the upper surface of the hydrofoil. The agreement between the calculation and the experiment is generally good. However, there are some differences. These slight differences are due to nonlinear free-surface effects, viscous effects on lift, or experimental inaccuracies.

8.0 THREE-DIMENSIONAL BODIES

Because of limitations imposed by the storage capacity of the digital computer and considerations of economy in the use of computing time, the program for three-dimensional bodies is less accurate than those for axisymmetric and two-dimensional bodies. (These limitations are discussed in reference 3) The results are very satisfactory for single bodies of fairly simple shape. For complicated bodies, and in particular for multiple-body interference problems, the calculations give useful information in the sense that a fair approximation of experiment is obtained, but the high degree of accuracy that is apparent in the comparisons of Sections 5.0, 6.0, and 7.0 cannot be realized. At present, the three-dimensional method is being reprogrammed to greatly increase its capacity by circumventing the machine storage limits. It is believed that this will enable fairly complex multiple-body problems to be calculated with the same accuracy that simple bodies are now calculated. Computing times will be quite long if this extra capacity is utilized.

8.1 Single Closed and Semi-Infinite Bodies

Reference 21 presents the results of low-speed wind-tunnel tests on a set of three symmetric delta wings, which are designated Wing A, Wing B, and Wing C. All three wings are of aspect ratio 1.0 and have 12-percent-thick parabolic-arc airfoil sections in their midplanes. They differ in planform and in the way in which the section shape varies across the span. Wing A has a gothic planform, and its thickness varies linearly with distance perpendicular to its midplane. Thus both the section shape and section thickness ratio vary across the span. Wing B and Wing C both have triangular planforms, and both have section shapes that are constant across the span. For Wing B the section thickness ratio is constant across the span, but for Wing C the section thickness ratio decreases linearly across the span. Sketches of the wings are given in figures 48, 49, and 50, which also show the isobars on the wings for the case of zero angle of attack. The solid isobars on the upper half of the planforms are those calculated by the present method, and the dotted isobars on the lower half of the planform are those obtained experimentally. The calculated and

experimental isobar patterns are essentially identical for Wing A and Wing B and only slightly different for Wing C. More precise comparisons are contained in figures 51, 52, and 53, which show calculated and experimental spanwise pressure distributions on the three wings for three chordwise locations in the midplane, i.e., pressures are plotted versus distance perpendicular to the midplane at three stations along the midplane chord. Experimental data are shown for both the upper surfaces and the lower surfaces of the wings. By symmetry, the pressure at any location should be identical on the upper and lower surfaces, so that the differences between these pressures give a measure of the experimental error. The calculated and experimental pressures agree to within experimental error for Wing A and Wing B, but differ somewhat on Wing C, particularly at the most aft location.

Comparisons were made of calculated and experimental pressures on the aft end of a DC-9 fuselage. In this case the fuselage was clean, i.e., there were no wings, pylons, or nacelles, and the calculation considered the body semi-infinite in the forward direction. If the same geometric shape were taken as the forward portion of a semi-infinite body, the calculated pressures would be expected to match experiment very well. Since this is the aft end of a semi-infinite body (for which the potential flow is the same as on the same shape as a forward end), viscous effects are significant. In particular, the boundary layer is relatively thick, and separation occurs. Figure 54 shows a sketch of the body shape and compares calculated and experimental pressure distributions along the side and bottom of the fuselage. The presence of flow separation on the bottom of the fuselage is clearly evident. The agreement is only fair; but the general trends and levels of the pressure are predicted by the calculations. Part of the disagreement is due to the fact that only a fraction of the program's capability was used in calculating the body. This was done because a pylon and nacelle were to be added to the fuselage later, as shown in figure 57, and the excess capability was reserved for these. The data of figure 54 were obtained by Douglas personnel from tests in the GALCIT wind tunnel at the California Institute of Technology.

8.2 Intersecting Wings

Mr. Wilburn L. Moore of the David Taylor Model Basin, Carderock, Maryland used the present method to calculate the pressure distribution on a pair of intersecting wings. The wings were straight and untapered, and each had an airfoil section that did not vary along the span. The airfoil section shape for both wings was a symmetric one and was identical to that of DTMB Series 58 Model 4162 as described in David Taylor Model Basin Report No. 1669. One wing had a 20-percent-thick section shape, and the other had a 10-percent-thick section shape. The wings, which were considered to be infinite in both spanwise directions, intersected at a right angle, and thus the complete configuration had two perpendicular planes of symmetry. The direction of the onset flow was parallel to both symmetry planes, and thus both wings were nonlifting. Tests of this configuration were conducted in the David Taylor Model Basin Low Speed Wind Tunnel. Comparison of the calculated and experimental pressure distributions were made and furnished the authors by Mr. Moore in a private communication. The comparisons are shown in figures 55 and 56. The effect on the pressures of the thickening of the boundary layer in the intersection is quite evident from the data on the aft portion of the wings in the intersection and at the nearest spanwise station to the intersection (0.2 chord). At these locations, calculated and experimental pressures agree only over the forward half of the wings. At the spanwise stations farther from the intersection, the agreement is fairly good over the entire chord, with calculated pressures generally less negative than experimental ones. The pressure distribution on both wings are identical in the intersection and approach two-dimensional results far out along the span. The variations of pressure with distance along the span are quite different for the two wings, since their thicknesses, which determine their two-dimensional pressure distributions, differ by a factor of two. The spanwise variation of pressure distribution is predicted fairly well by the calculations.

8.3 Fuselage-Pylon-Nacelle Interference

The present method was used to calculate pressure distributions on the DC-9 fuselage-pylon-nacelle combination. The fuselage shape is sketched in

figure 54, and detail views of the pylon-nacelle installation are given in figure 57. (Notice the interior surface of the nacelle, which was accounted for in the calculations.) Of particular interest were pressures on the pylon where the interference effects of the fuselage and nacelle are expected to give rise to rather high velocities. Figure 57 shows a comparison of calculated and experimental pressure distributions along the middle of the pylon. Agreement is good. The data of figure 57 were obtained by Douglas personnel from tests in the GALCIT wind tunnel at the California Institute of Technology.

8.4 Destroyer Sonar Dome

Mr. Stephen B. Denny of the David Taylor Model Basin used the present method to calculate the pressure distribution on the sonar dome of a destroyer and compared the results with experimental data obtained from tests in the towing basin at the David Taylor Model Basin. A complete description of his work is contained in reference 22, from which the figures of this section were taken. Figure 58 is a photograph of the sonar dome. The numbers in this figure denote the orifice locations at which experimental measurements were made. (The nomenclature here is changed from that of reference (22), which denoted orifice locations as pitot tube locations.) Comparisons of calculated and experimental pressure distributions on the sonar dome are shown in figure 59 and 60. The pressures are plotted versus orifice number as given in figure 58. The agreement is generally satisfactory. The "wiggle" in the calculated pressure distribution near orifice 30 in figure 60 is unexplained. The body is perfectly smooth there, and the local input data were checked for smoothness. No similar result has ever been obtained on such a smooth body. It is felt that there must be some explanation for the wiggle and that the effect will not recur. Fairing through the wiggle in the obvious way gives a good result.

8.5 Interference at High Subsonic Mach Number.

Wing-Fuselage and Wing-Pylon-Nacelle

For three-dimensional bodies, as for the axisymmetric bodies of Section 5.3, compressibility effects are accounted for by using a Göthert transformation.

The present method was used to calculate the pressure distribution on an NACA wing-fuselage combination at a Mach number of 0.6. The fuselage is a pointed axisymmetric body, and the swept tapered wing, which is mounted as a midwing on the fuselage, has a symmetric airfoil section 6 percent thick. The configuration is described in reference 23, which also contains experimental pressure distributions on the wing. Figure 61 compares calculated and experimental isobars on this configuration and shows a sketch of the shape. The isobars on the left wing are those calculated by the present method (calculated isobars on the fuselage are also shown); the isobars on the right wing are those obtained experimentally. The two patterns are similar over most of the wing, with corresponding isobars on the two sides differing slightly in pressure level. Discrepancies occur near the leading and trailing edges. A more precise comparison is given in figure 62, which compares calculated and experimental chordwise pressure distributions at three spanwise locations for the condition of zero lift. Since the airfoil section is identical at all spanwise locations, the variation of pressure distribution with position along the span exhibits the magnitude of the three-dimensional effects. The calculated pressures agree well with the experimental pressures except very near the trailing edge, where the boundary layer has affected the experimental pressures, and very near the leading edge, where the calculated pressure distributions have small, sharp negative peaks that are absent from the experimental curves, especially at the two outboard locations. To investigate this latter phenomenon further, the airfoil section was considered a two-dimensional body, and the flow was calculated by the two-dimensional program. In view of the comparison shown in Section 7.1, great confidence can be placed in the accuracy of this calculation, particularly for the simple nonlifting case. Calculated two-dimensional pressure distributions on this airfoil are shown in figure 63 for Mach numbers of zero and 0.6. These pressure distributions exhibit the same small, sharp negative peak near the leading edge that is observed in figure 62. It is accordingly concluded that this peak is real and was correctly predicted by the present method for the three-dimensional case. Why the experimental pressure distributions fail to show such peaks is not known. It is known, however, that the pressure distribution near the leading edge of a thin airfoil is extremely sensitive to the body shape in that region. A very small discrepancy in the coordinates of the wind-tunnel model could lead to the absence of a peak.

Probably the most extreme case to which the present method has been applied is the calculation of the mutual interference between the wing, pylon, and nacelle of the DC-8. The configuration about which the flow was calculated is sketched in figure 64. It consists of a portion of the DC-8 wing to which are attached the inboard pair of nacelles and pylons. The configuration was adjusted somewhat from that of the actual airplane. Only the portion of the wing near the pylon-nacelle was included in the calculations. Thus the two pylon-nacelles are much closer together in the calculated configuration than in the actual one. It was hoped that the resulting increase in mutual interference between the pylon-nacelles would partially compensate for the omission of the fuselage. In any event such an effect should be small. The pressure distribution is chiefly determined by the local wing-pylon-nacelle geometry. The calculations were performed for the nonlifting condition. This very complicated geometry, which includes both upper and lower wing surfaces and inner and outer nacelle surfaces, taxes the capacity of the method very severely. Moreover, the test data with which the calculations were compared were obtained at the very high Mach number of 0.825, which resulted in the presence of local regions of supersonic flow on the body surface. The tests were conducted by Douglas personnel in the Southern California Cooperative Wind Tunnel. The model tested was a complete DC-8 and thus differed from the body calculated, by the presence of the fuselage, outboard wing, and outboard nacelles. Figure 65 compares calculated and experimental pressure distributions on the nacelle, and figure 66 compares calculated and experimental pressure distributions on the pylon. As is indicated in figure 66, the calculated and experimental pressures that are compared on the pylon were obtained at slightly different locations. In all plots the pressure level for locally sonic conditions is indicated, and the regions of supersonic flow are evident. It is felt that the agreement of calculated and experimental pressures is remarkably good under the circumstances.

9.0 REFERENCES

1. Smith, A. M. O., and Pierce, J.: Exact Solution of the Neumann Problem. Calculation of Non-Circulatory Plane and Axially Symmetric Flows about or within Arbitrary Boundaries. Douglas Aircraft Company Report No. ES 26988, April, 1958. Also in Proceedings of the Third U.S. National Congress of Applied Mechanics, Brown University, 1958.
2. Hess, J. L.: Calculation of Potential Flow about Bodies of Revolution Having Axes Perpendicular to the Free Stream Direction. Journal of the Aerospace Sciences, Vol. 29, No. 6, June 1962.
3. Hess, J. L., and Smith, A. M. O.: Calculation of Non-Lifting Potential Flow about Arbitrary Three-Dimensional Bodies. Journal of Ship Research, Vol. 8, No. 2, September, 1964.
4. Smith, A. M. O., Giesing, J. P., and Hess, J. L.: Calculation of Waves and Wave Resistance for Bodies Moving on or beneath the Surface of the Sea. Douglas Aircraft Company Report No. 31488A, November, 1963.
5. Giesing, J. P.: Extension of the Douglas Neumann Program to Problems of Lifting Infinite Cascades. Douglas Aircraft Company Report No. LB 31653, July, 1964.
6. Hess, J. L.: Comparison of Experimental Pressure Distributions with Those Calculated by the Neumann Program. Douglas Aircraft Company Report No. ES 29813, May, 1960.
7. Eisenberg, P.: A Cavitation Method for the Development of Forms Having Specified Critical Cavitation Numbers. David Taylor Model Basin Report No. 647, 1947.
8. Matthews, C. W.: A Comparison of the Experimental Subsonic Pressure Distributions about Several Bodies of Revolution with Pressure Distributions Computed by Means of Linearized Theory. NACA RM L9F28, September 12, 1949.
9. Young, A. D., and Owen, P. R.: Simplified Theory for Streamline Bodies of Revolution and Its Application to the Development of High-Speed Low-Drag Shapes. British R and M No. 2071, July, 1943.
10. Platt, R. J., Jr.: Static Tests of a Shrouded and an Unshrouded Propeller. NACA RM L7H25, February, 1948.
11. Taylor, R. A.: Pressure Distributions at Transonic Speeds for Bumpy and Indented Midsections of a Parabolic-Arc Body. NASA Memo 1-22-59A.

12. Campbell, I. J., and Lewis, R. G.: Pressure Distributions: Axially Symmetric Bodies in Oblique Flow. British C.P. No. 213, 1955.
13. Johnson, W. E.: Experimental Investigation and Correlation with Theory of the Surface Pressure Distribution on Several Sharp and Blunted Cones for Incompressible Flow. Master's Thesis, Department of Aeronautics and Astronautics, University of Washington, 1963.
14. Nichols, M. R., and Keith, A. L., Jr.: Investigation of a Systematic Group of NACA 1-Series Cowlings with and without Spinners. NACA TR 950, 1949.
15. Swihart, J. M., and Whitcomb, C. F.: Pressure Distributions on Three Bodies of Revolution to Determine the Effect of Reynolds Number up to and Including the Transonic Speed Range. NACA RM L53H04, October, 1963.
16. Harris, T. A., and Lowry, J. G.: Pressure Distribution over an NACA 23012 Airfoil with a Fixed Slot and a Slotted Flap. NACA Report No. 732, 1942.
17. Wenzinger, C. J.: Pressure Distribution over an NACA 23012 Airfoil with an NACA 23012 External Airfoil Flap. NACA Report No. 614, 1938.
18. Preston, J. H., and Sweeting, N. E.: The Experimental Determination of the Boundary Layer Wake Characteristics of a Simple Joukowski Airfoil, with Particular Reference to the Trailing Edge Region. British R and M No. 1998, March, 1943.
19. Herrig, J. L., Emery, J. C., and Erwin, J. R.: Systematic Two-Dimensional Cascade Tests of NACA 65-Series Compressor Blades at Low Speeds. NACA TN 3916, 1957.
20. Parkin, B. R., Perry, B., and Wu, T. Y.: Pressure Distribution on a Hydrofoil Running Near the Water Surface. J. App. Phys. Vol. 27, No. 3, pp.232-240, March 1956.
21. Peckham, D. H.: Low-Speed Wind Tunnel Tests on a Series of Uncambered Slender Pointed Wings with Sharp Edges. British R and M 3186, 1961.
22. Denny, S. B.: Applicability of the Douglas Computer Program to Hull Pressure Problems. David Taylor Model Basin Report No. 1786, October, 1963.
23. Loving, D. L., and Estabrook, B.B.: Transonic-Wing Investigation in the Langley 8-Foot High-Speed Tunnel at High Subsonic Mach Numbers and at a Mach Number of 1.2. Analysis of Pressure Distribution of Wing-Fuselage Configuration Having a Wing of 45° Sweepback, Aspect Ratio 4, Taper Ratio 0.6, and NACA 65A006 Airfoil Section. NACA RM L51F07, September, 1951.

— PRESENT METHOD

○ ○ ○ EXPERIMENTAL

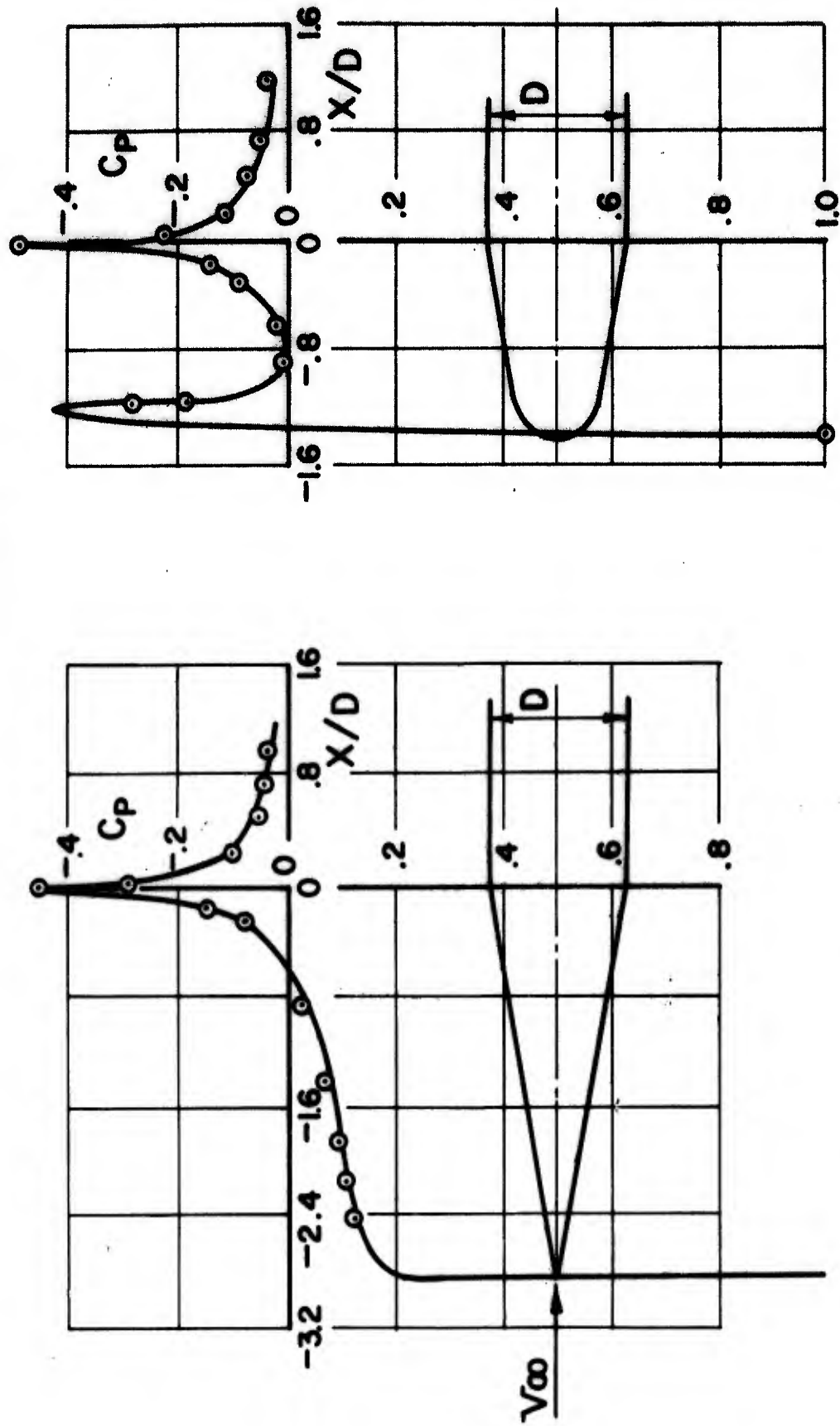


Figure 1. - Comparison of calculated and experimental pressure distributions on a sharp and a blunted cone-cylinder.

— PRESENT METHOD
 ○ ○ ○ EXPERIMENTAL

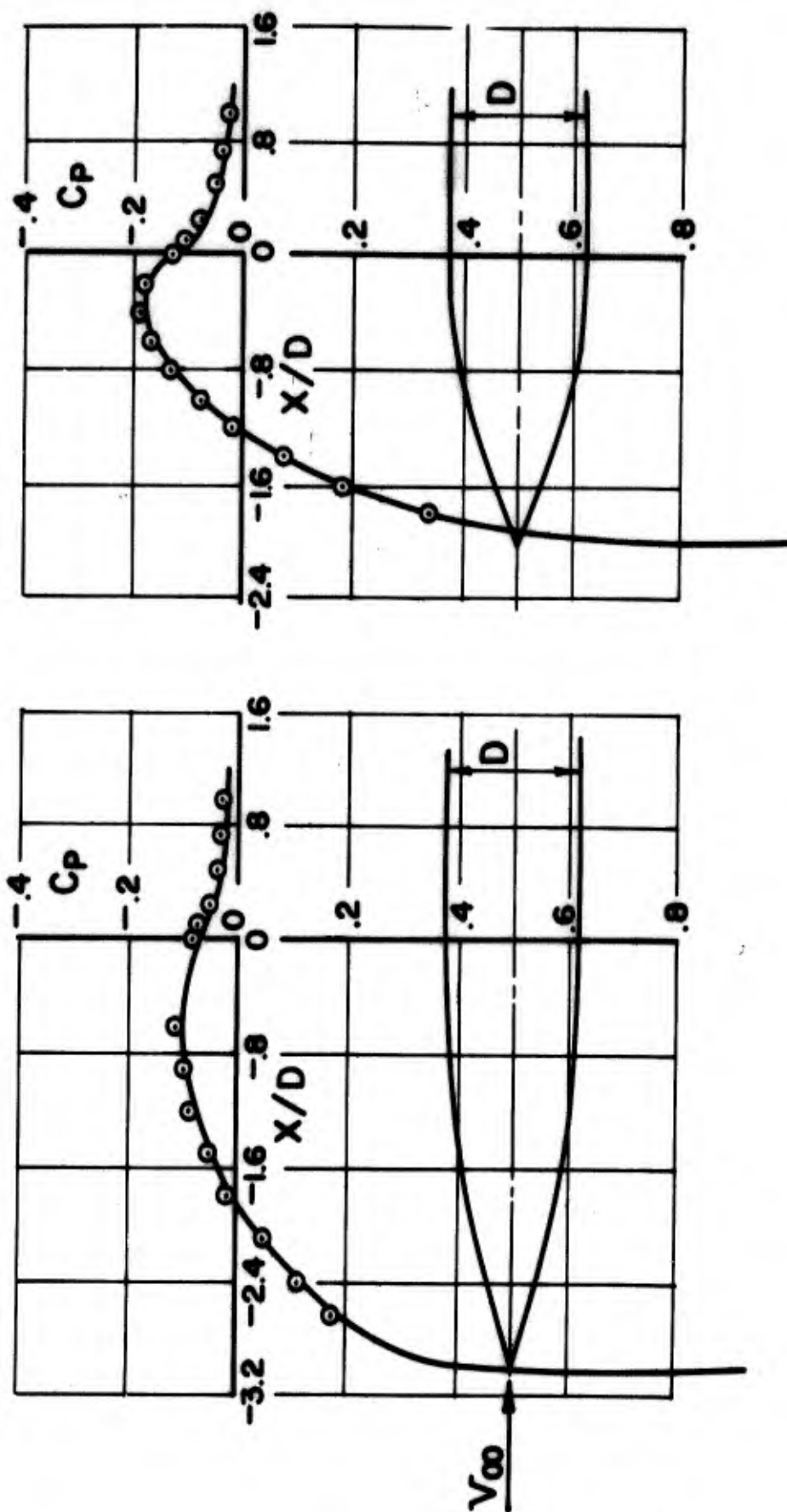


Figure 2. - Comparison of calculated and experimental pressure distributions on two ogive-cylinders.

— PRESENT METHOD
 ○ ○ ○ EXPERIMENTAL

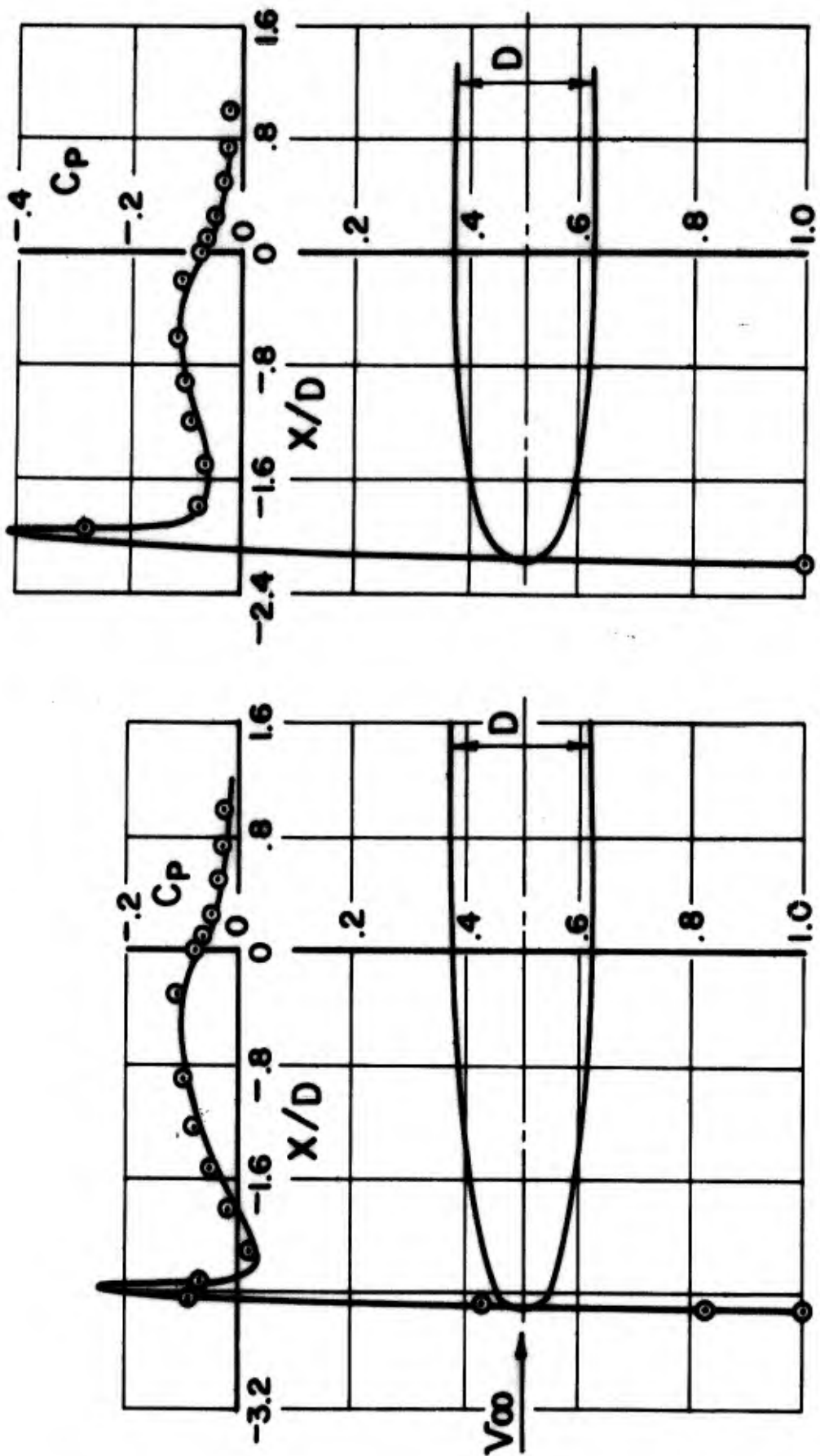


Figure 3. - Comparison of calculated and experimental pressure distributions on two blunted ogive-cylinders.

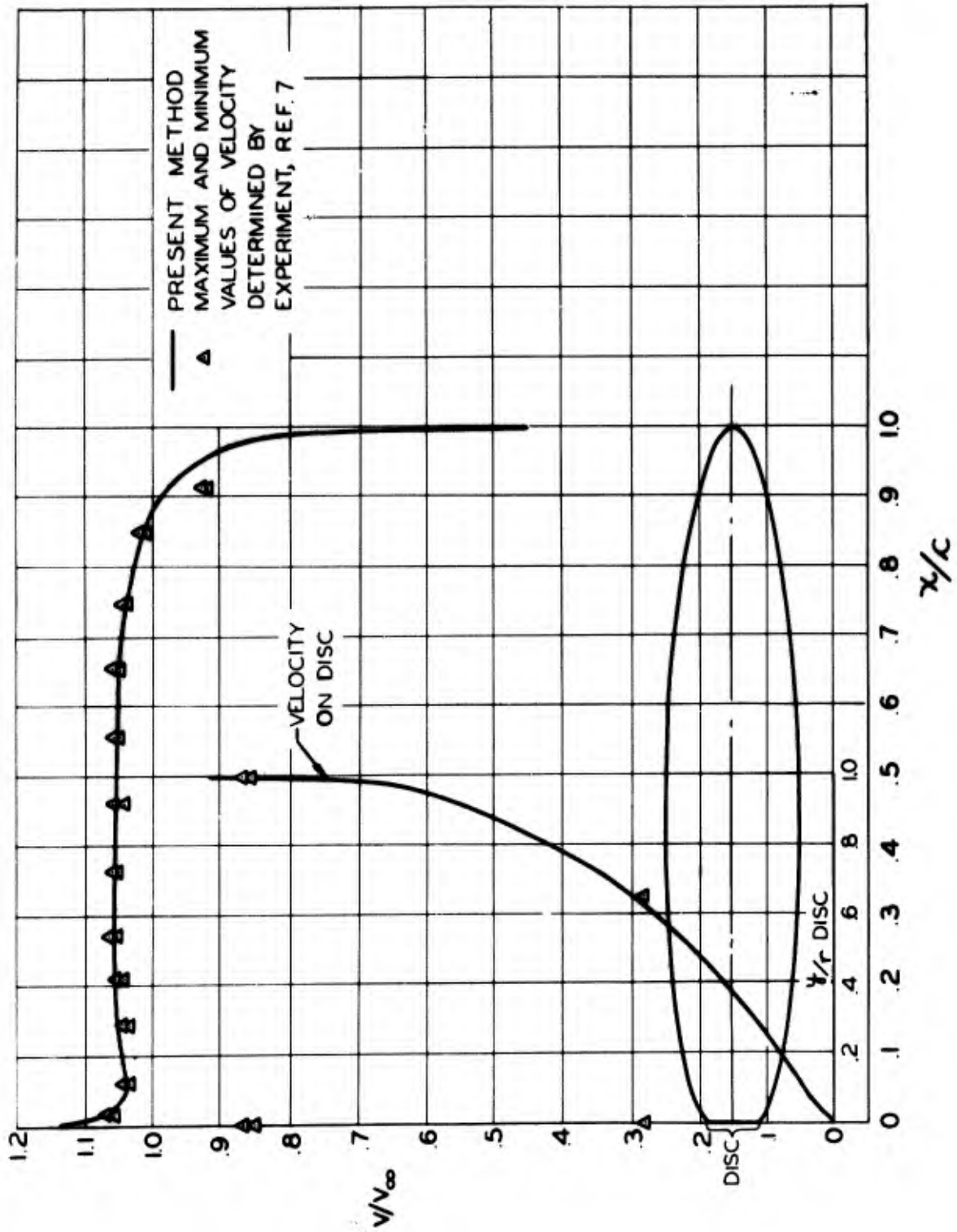


Figure 4. - Comparison of calculated and experimental velocity distributions on a flat-nosed body.

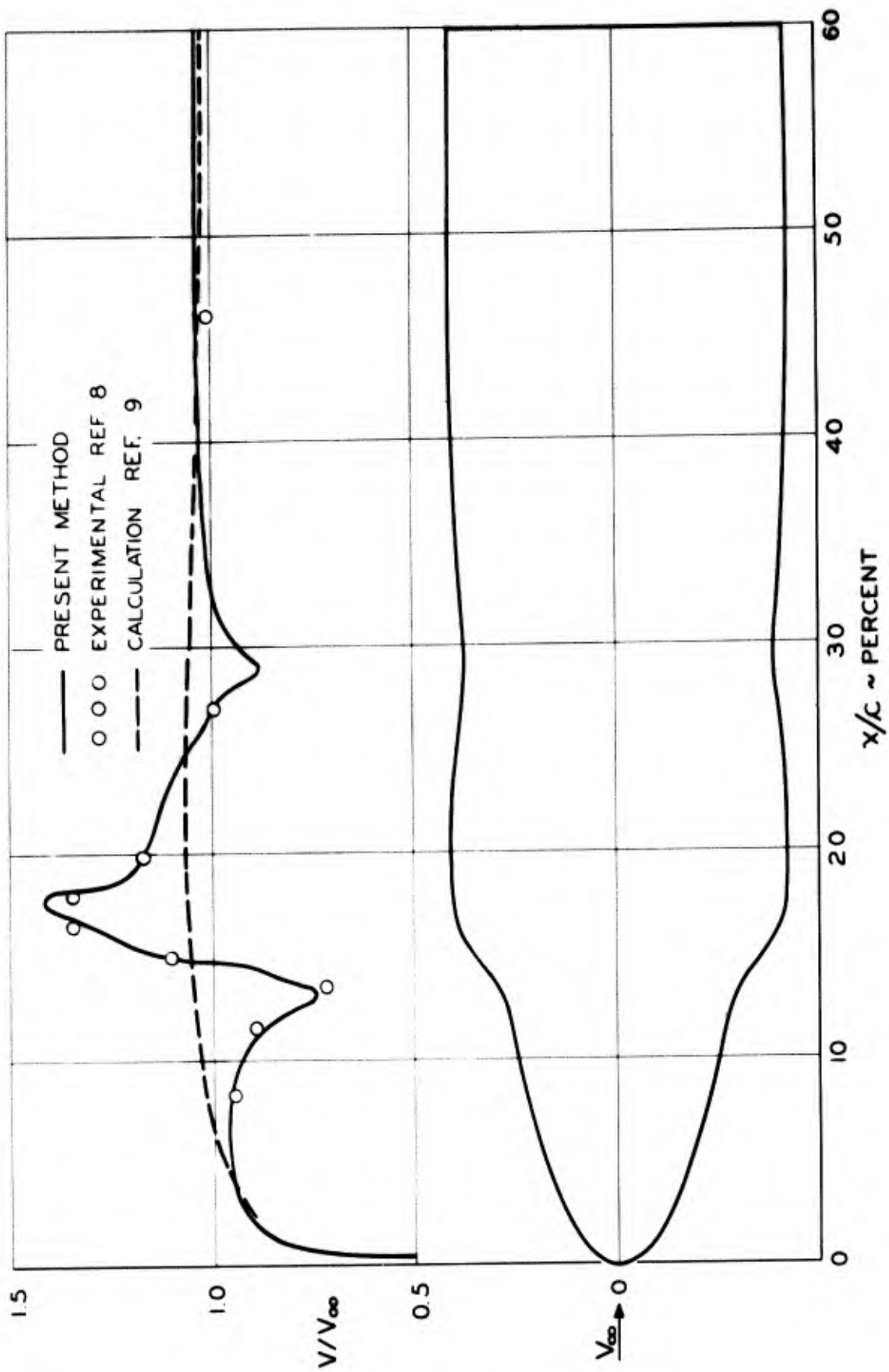


Figure 5. - Comparison of calculated and experimental velocity distributions on a prolate spheroid with an annular bump.

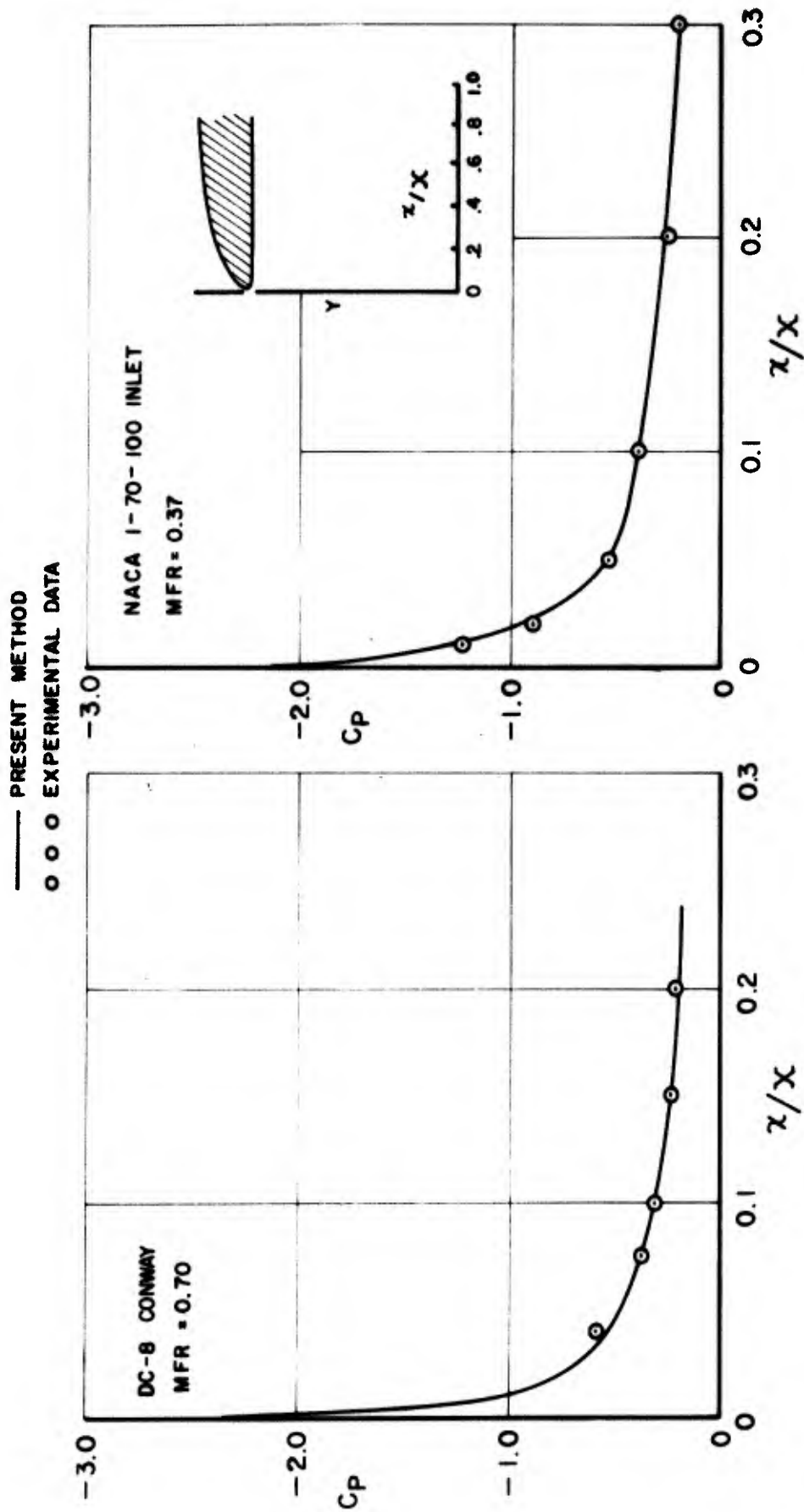


Figure 6. - Comparison of calculated and experimental pressure distributions on the exteriors of two inlet lips at finite mass-flow ratios.

— PRESENT METHOD

○ ○ ○ EXPERIMENTAL

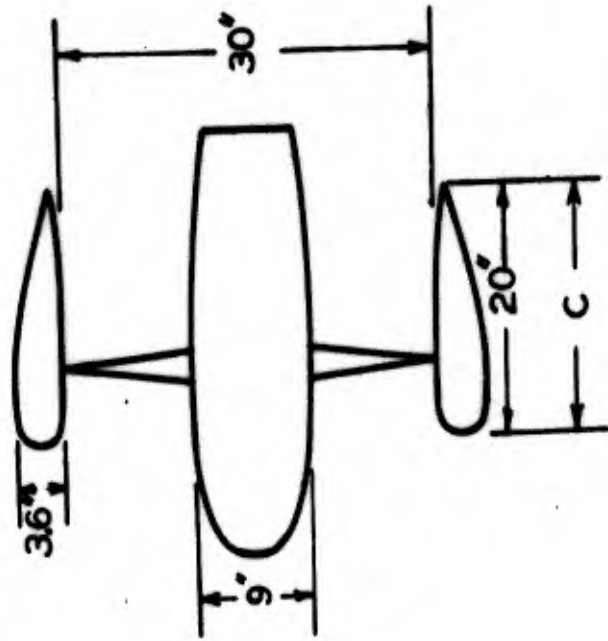
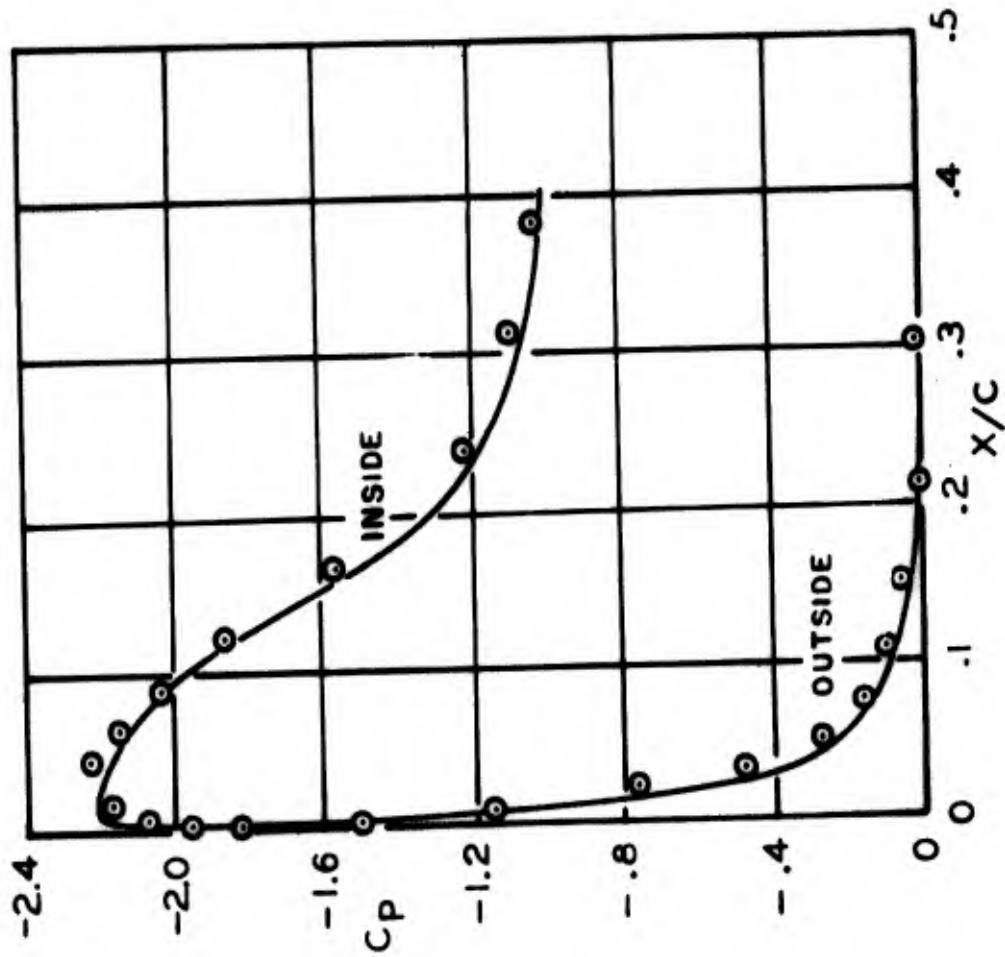


Figure 7. - Comparison of calculated and experimental pressure distributions on a propeller shroud with centerbody in static operation.

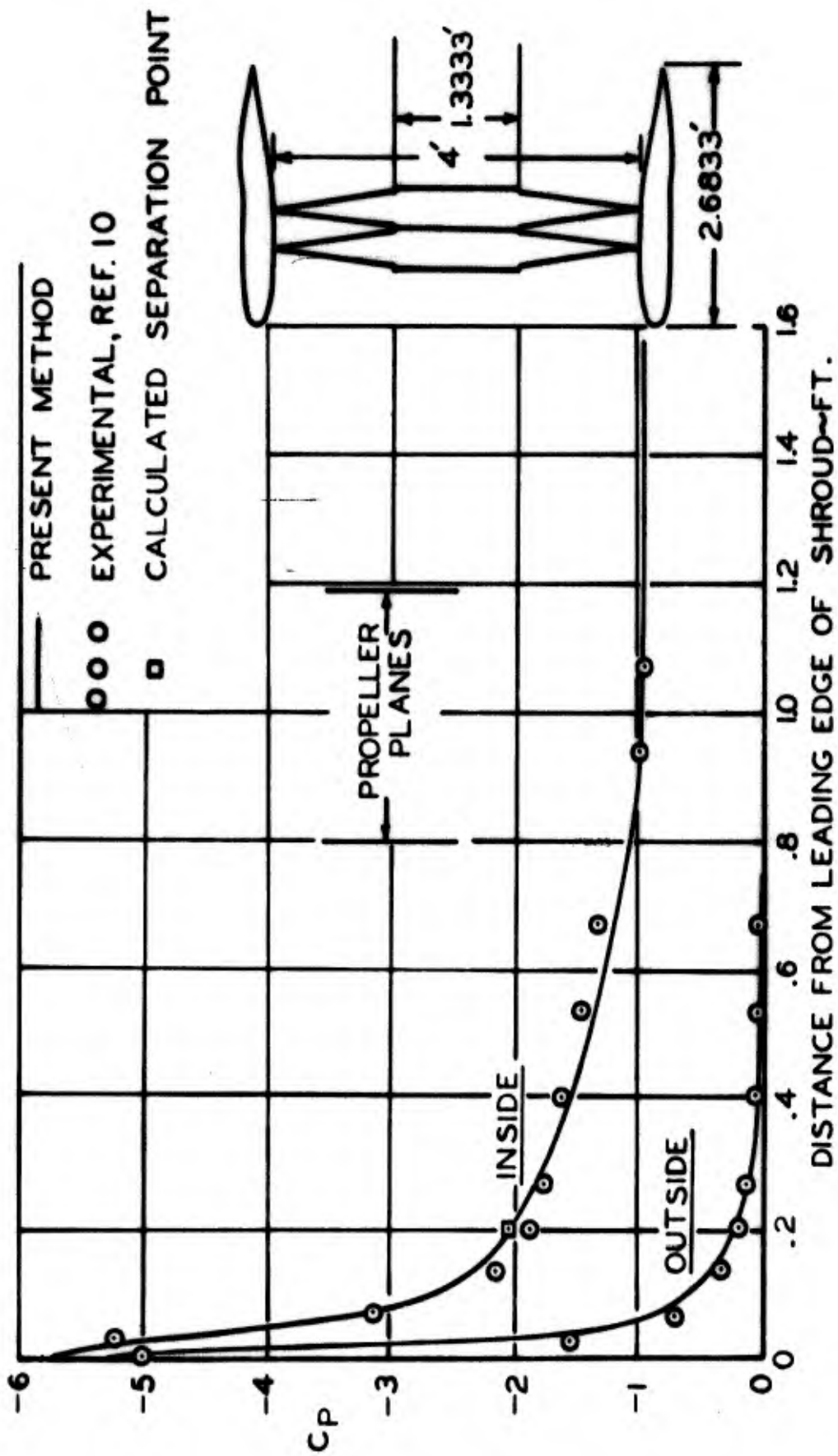


Figure 8. - Comparison of calculated and experimental pressure distributions on a propeller shroud with dual rotation propeller in static operation.

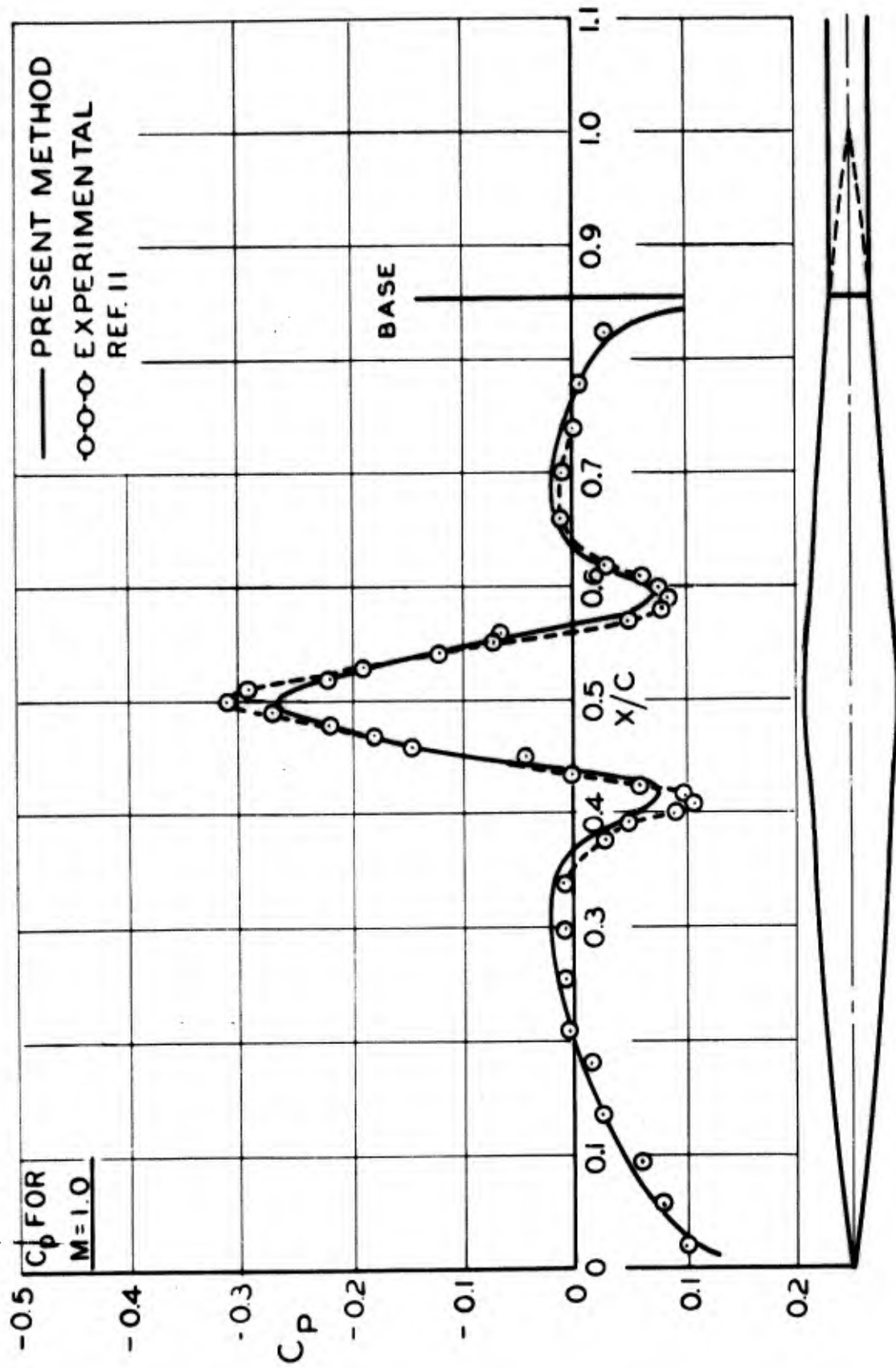


Figure 9. - Comparison of calculated and experimental pressure distributions on a parabolic-arc body with a bump for a Mach number of 0.8.

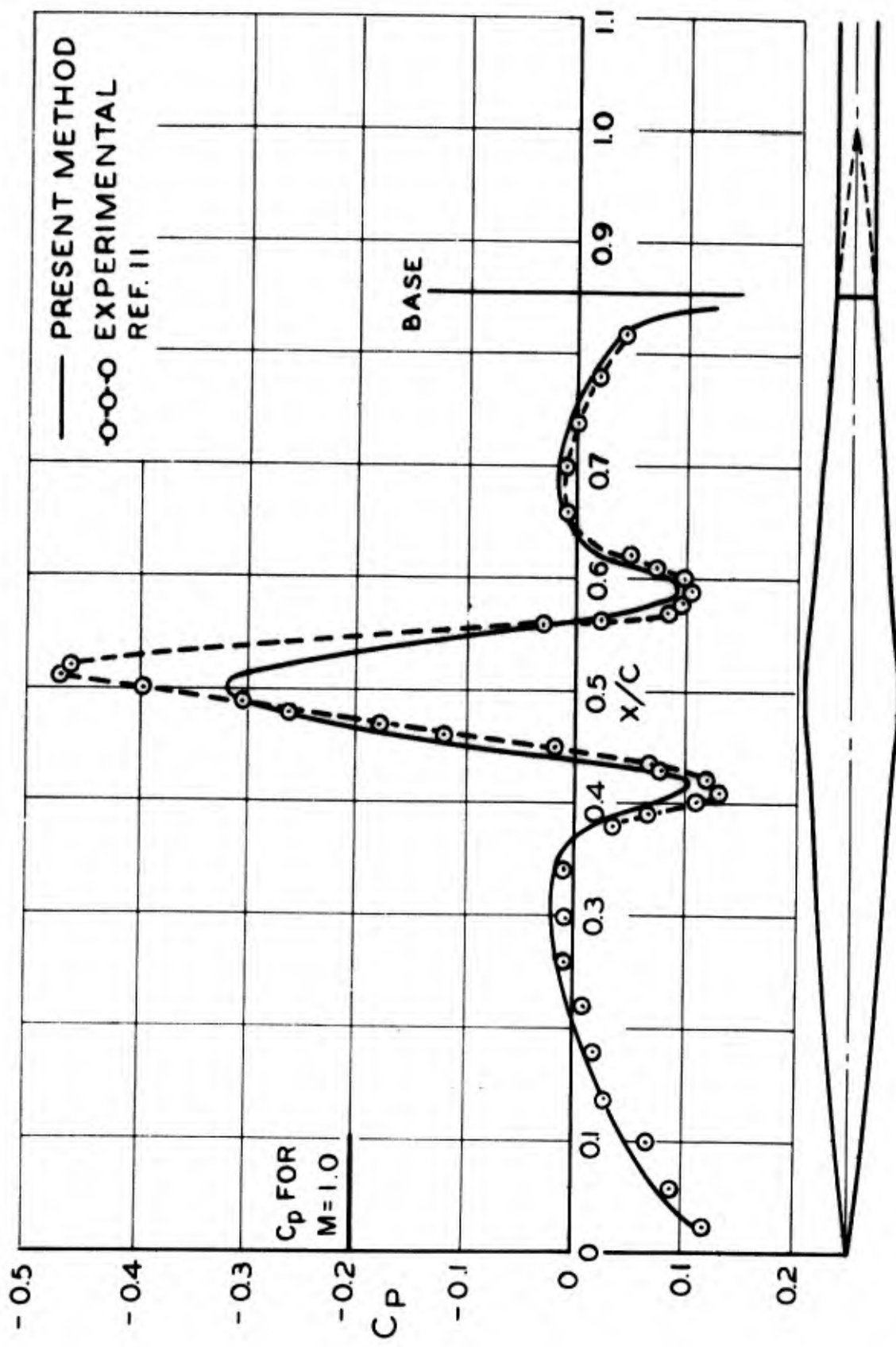


Figure 10. - Comparison of calculated and experimental pressure distributions on a parabolic-arc body with a bump for a Mach number of 0.9.

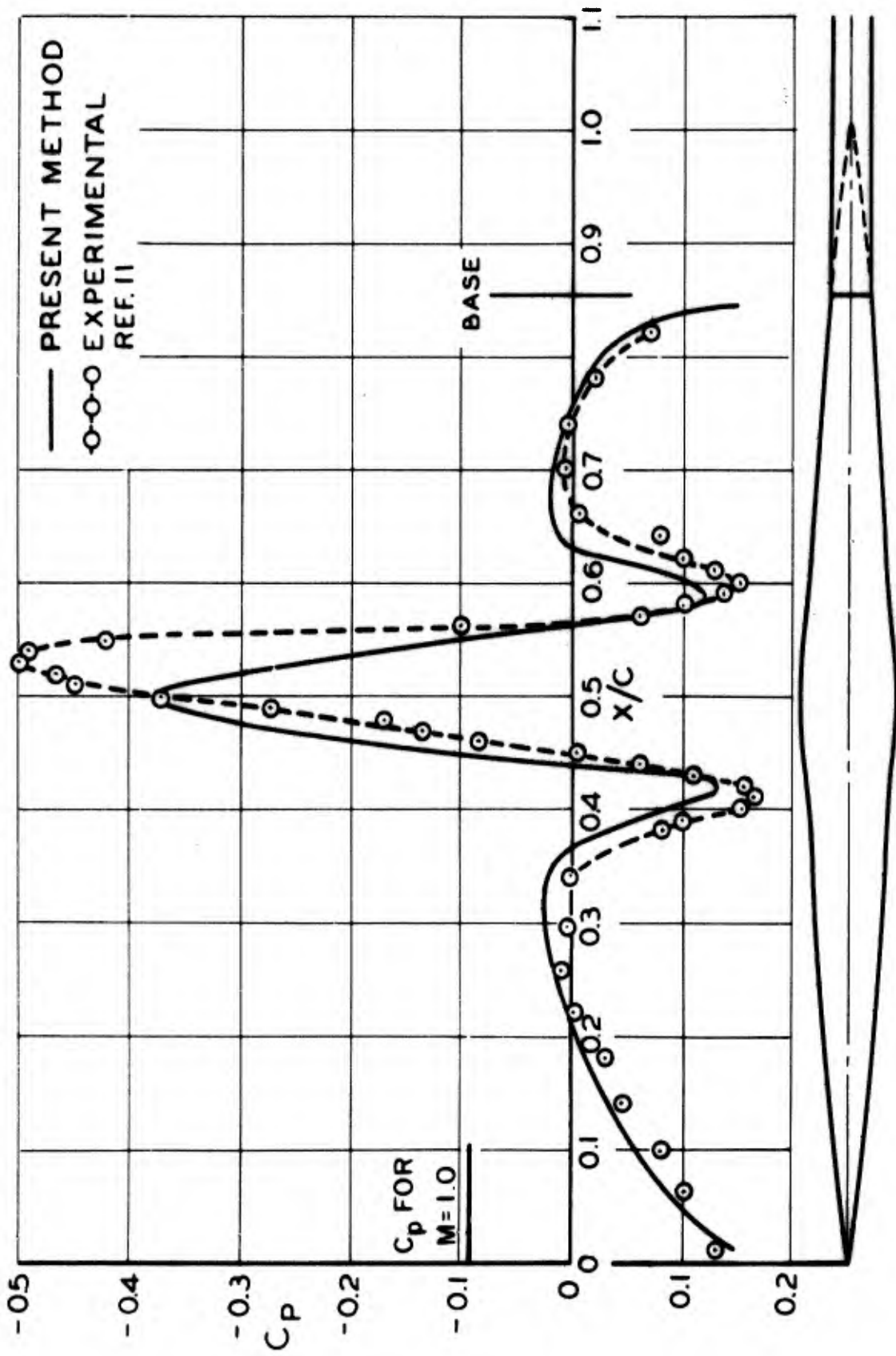


Figure 11. - Comparison of calculated and experimental pressure distributions on a parabolic-arc body with a bump for a Mach number of 0.95.

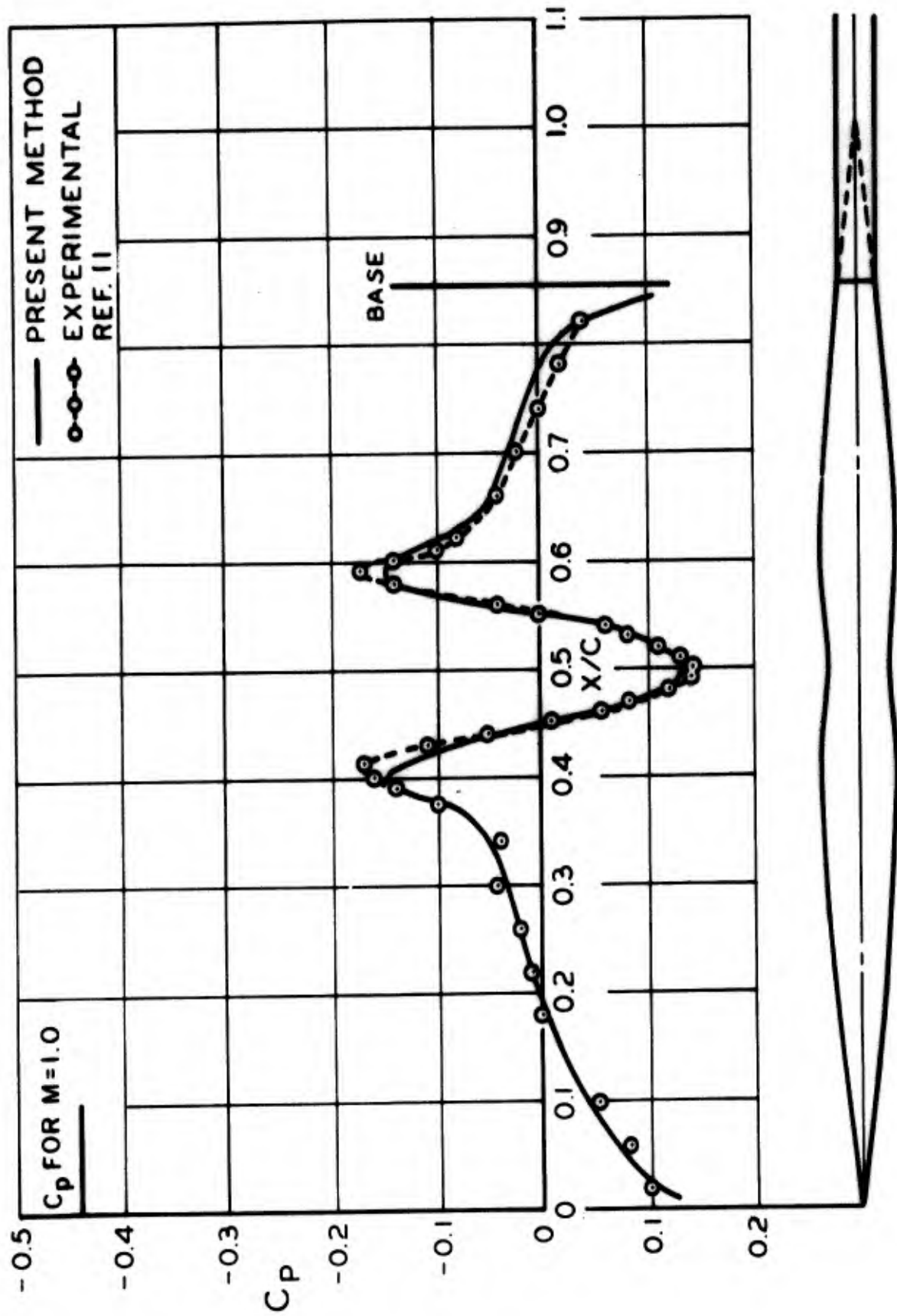


Figure 12. - Comparison of calculated and experimental pressure distributions on an indented parabolic-arc body for a Mach number of 0.8.

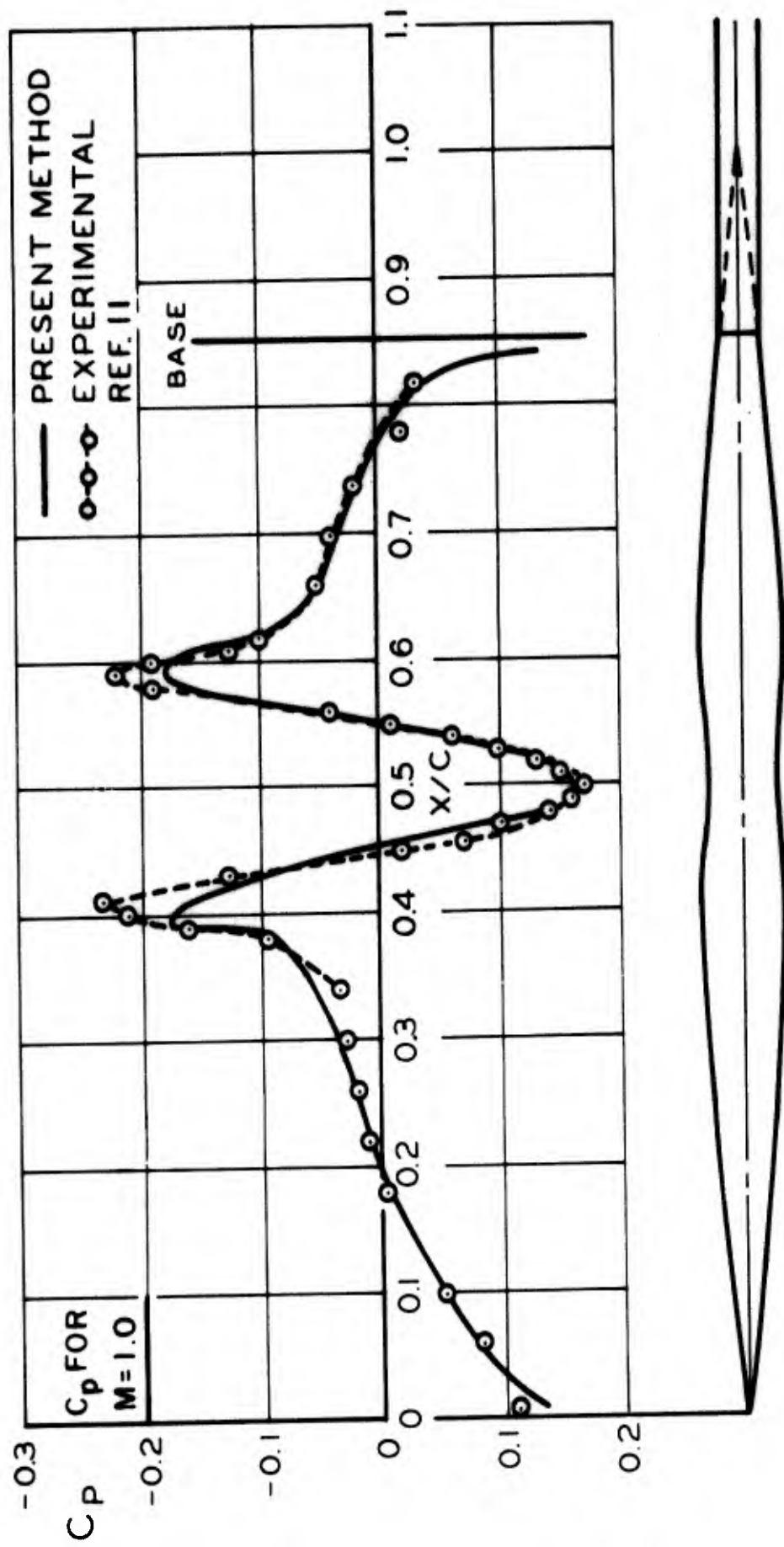


Figure 13. - Comparison of calculated and experimental pressure distributions on an indented parabolic-arc body for a Mach number of 0.9.

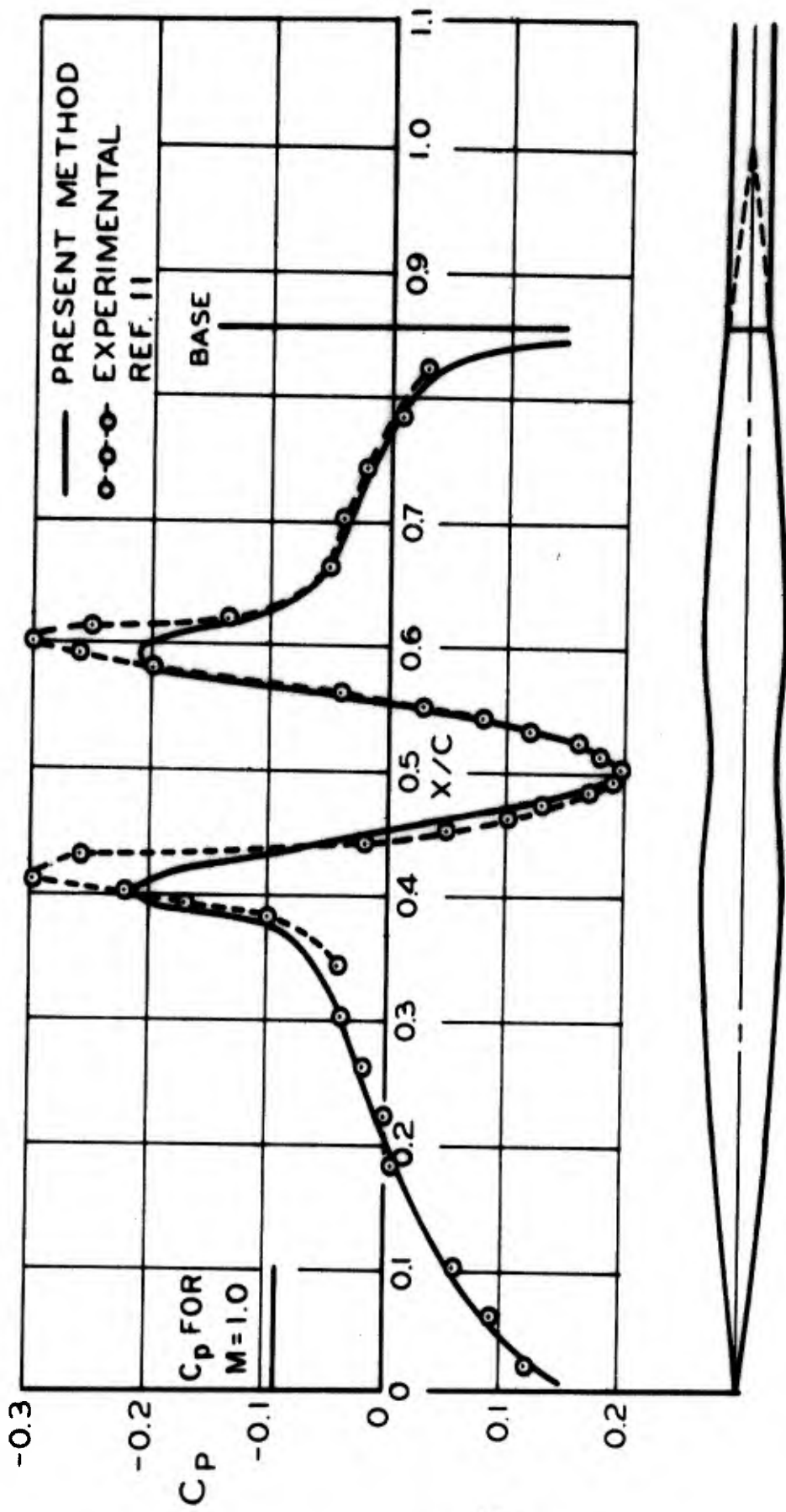


Figure 14. - Comparison of calculated and experimental pressure distributions on an indented parabolic-arc body for a Mach number of 0.95.

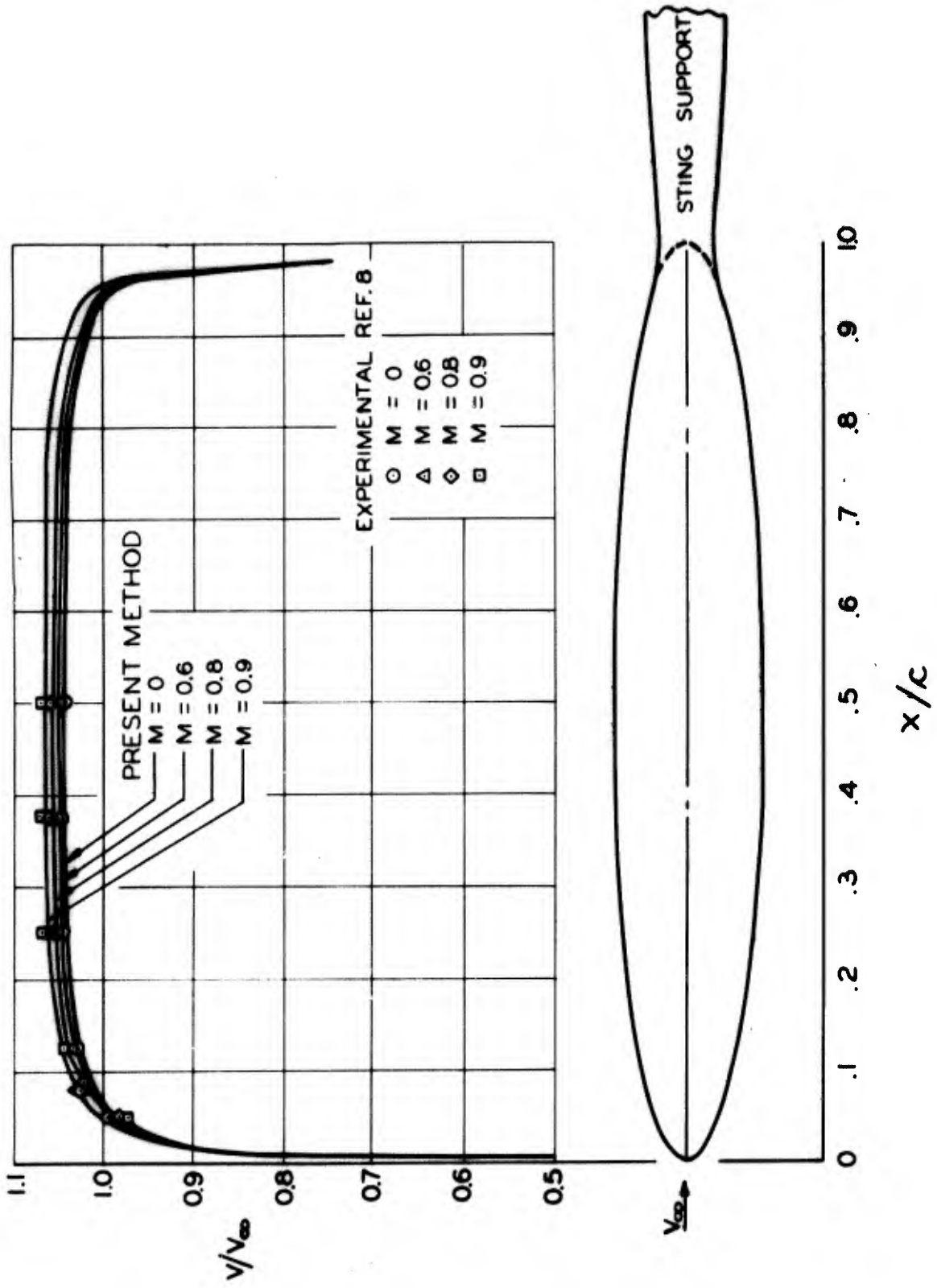


Figure 15. - Comparison of calculated and experimental velocity distributions on a prolate spheroid of fineness ratio 6 for various Mach numbers.

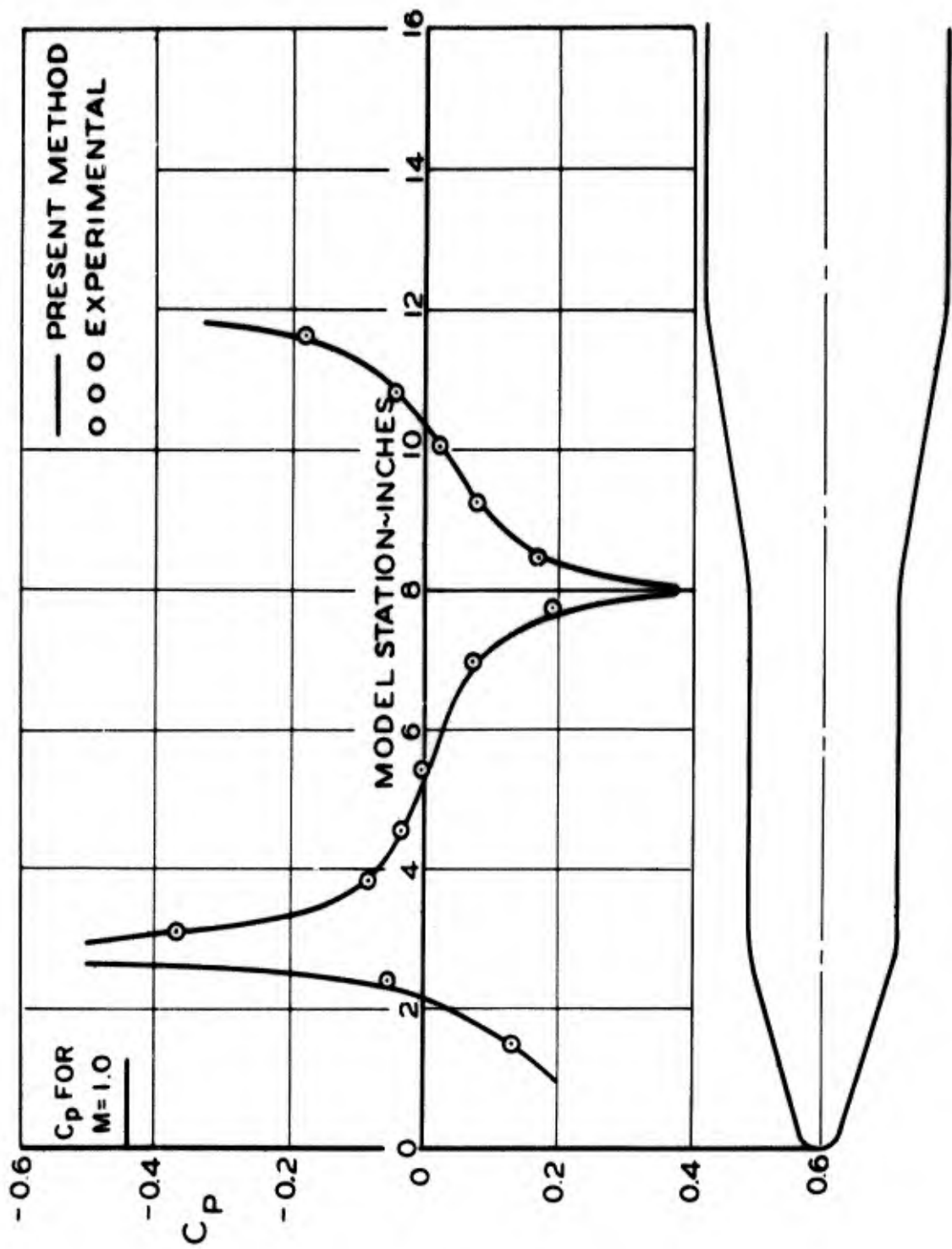


Figure 16. - Comparison of calculated and experimental pressure distributions on a Skybolt missile at a Mach number of 0.8.

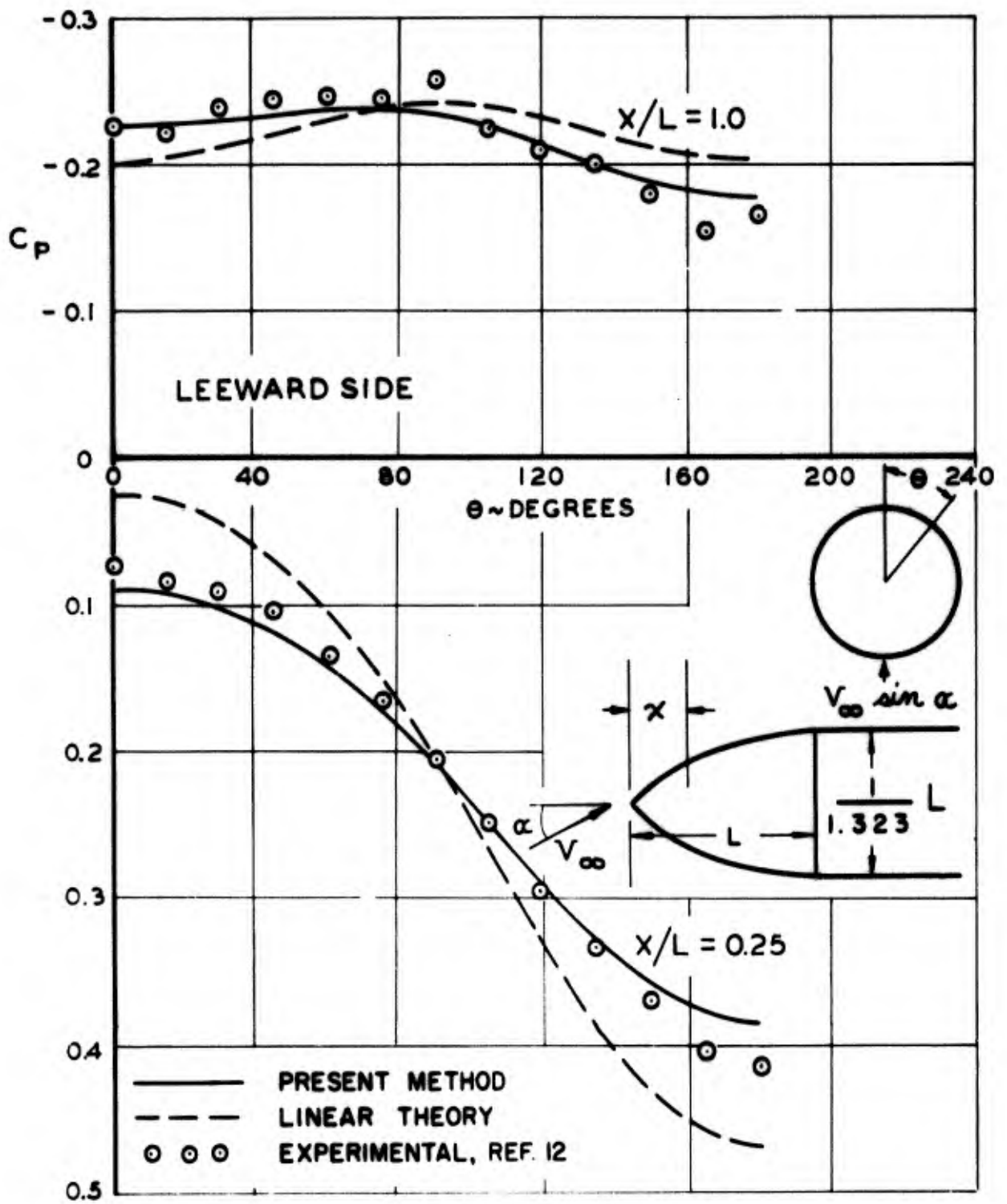


Figure 17.- Comparison of calculated and experimental circumferential pressure distributions on an ogive-cylinder at 5.73° angle of attack

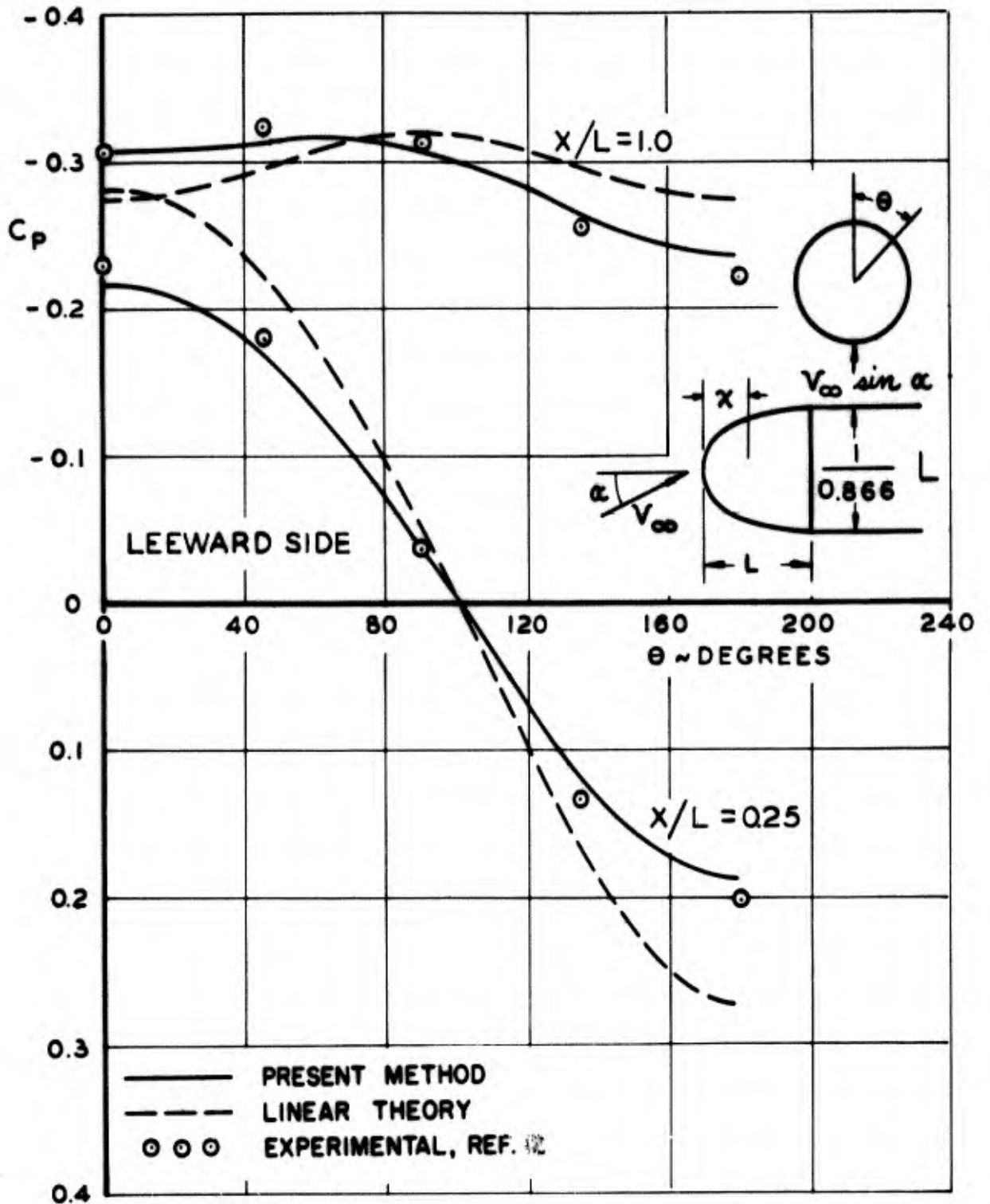


Figure 18.- Comparison of calculated and experimental circumferential pressure distributions on an ellipsoid-cylinder at 6.05° angle of attack.

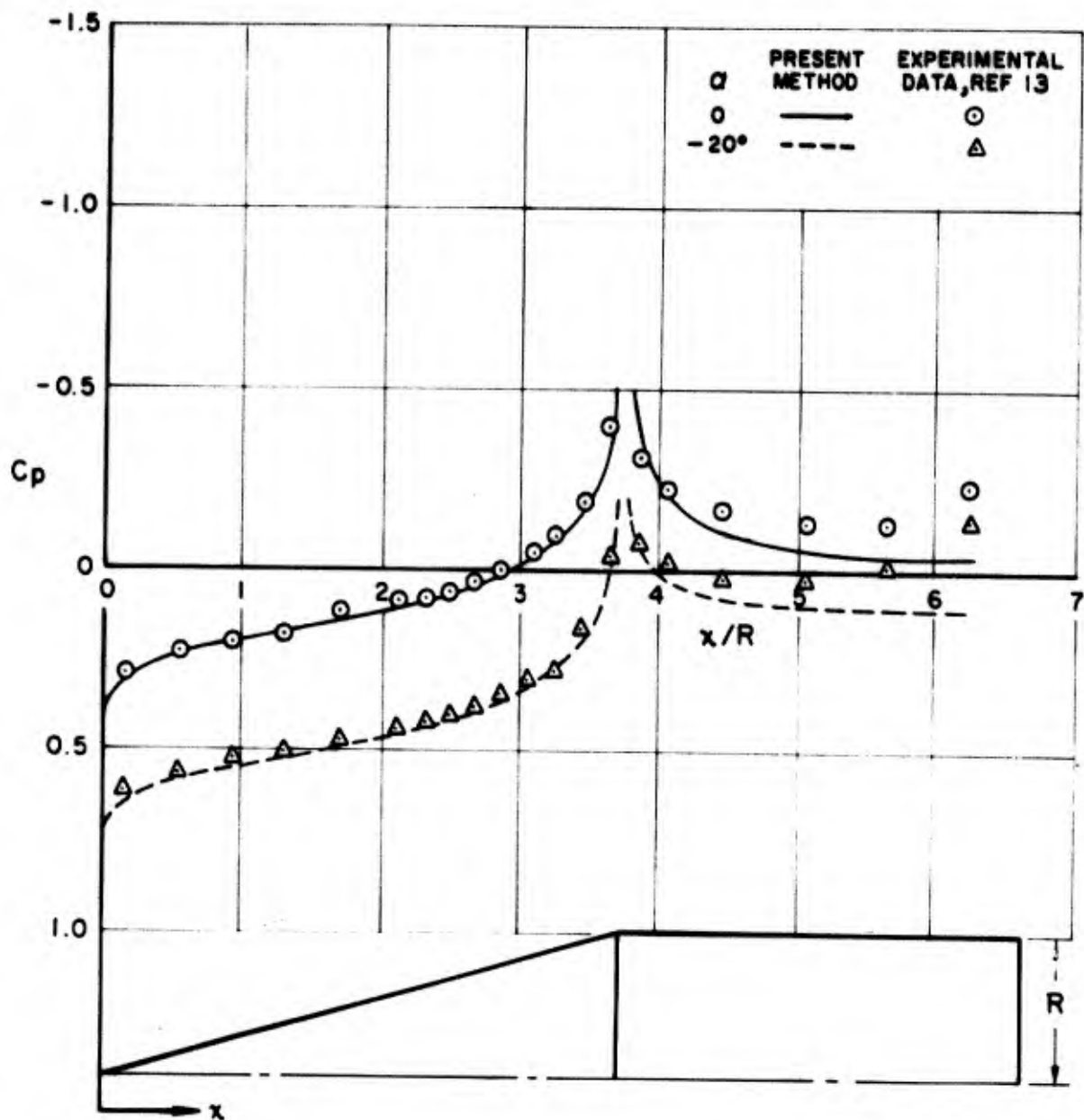


Figure 19. - Comparison of calculated and experimental pressure distributions on a 15° cone-cylinder at 0° and 20° angle of attack.

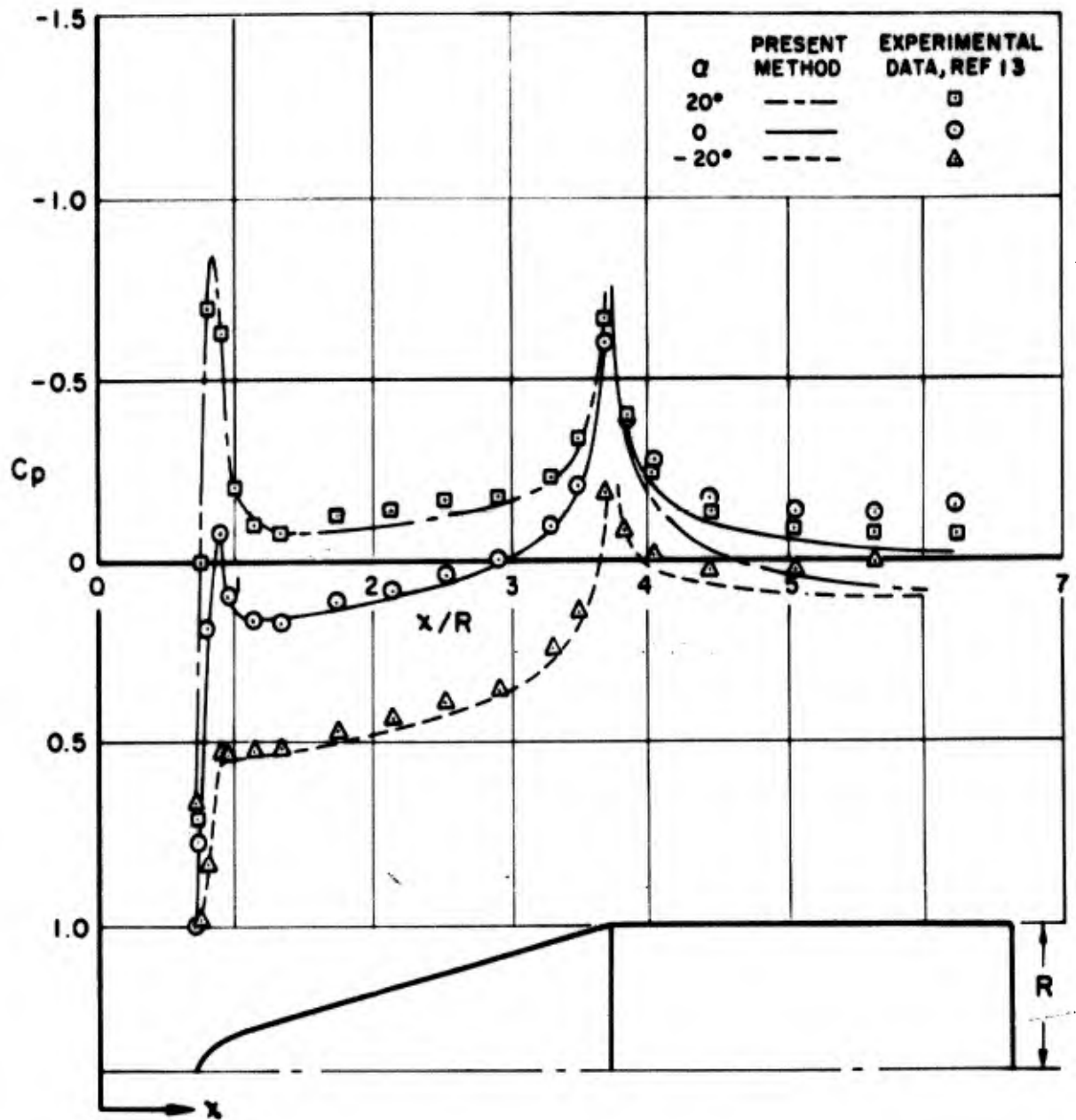


Figure 20. - Comparison of calculated and experimental pressure distributions on a blunted 15° cone-cylinder with nose radius equal to one-fourth final radius at 0° and 20° angle of attack.

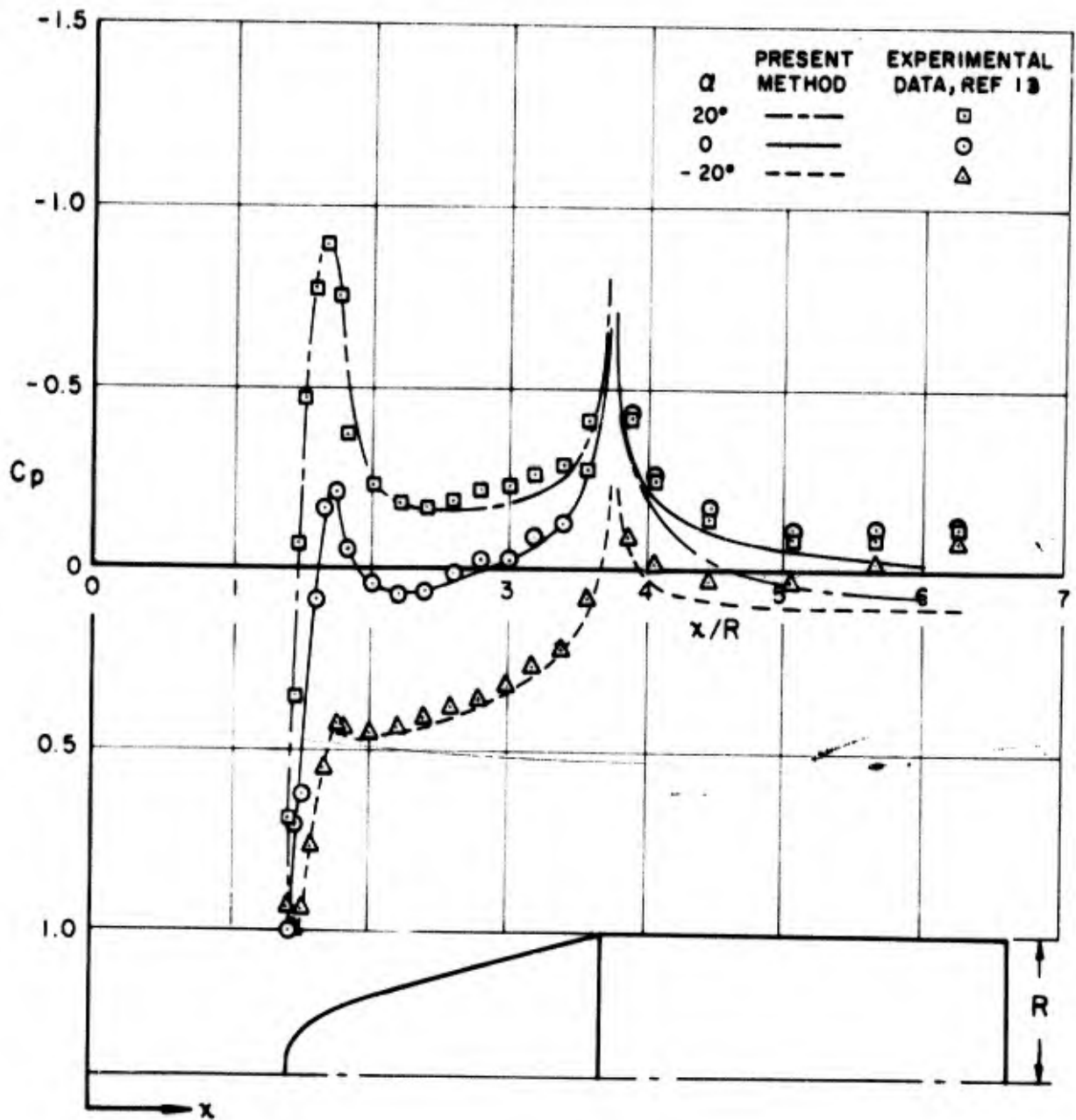


Figure 21. - Comparison of calculated and experimental pressure distributions on a blunted 15° cone-cylinder with nose radius equal to one-half final radius at 0° and 20° angle of attack.

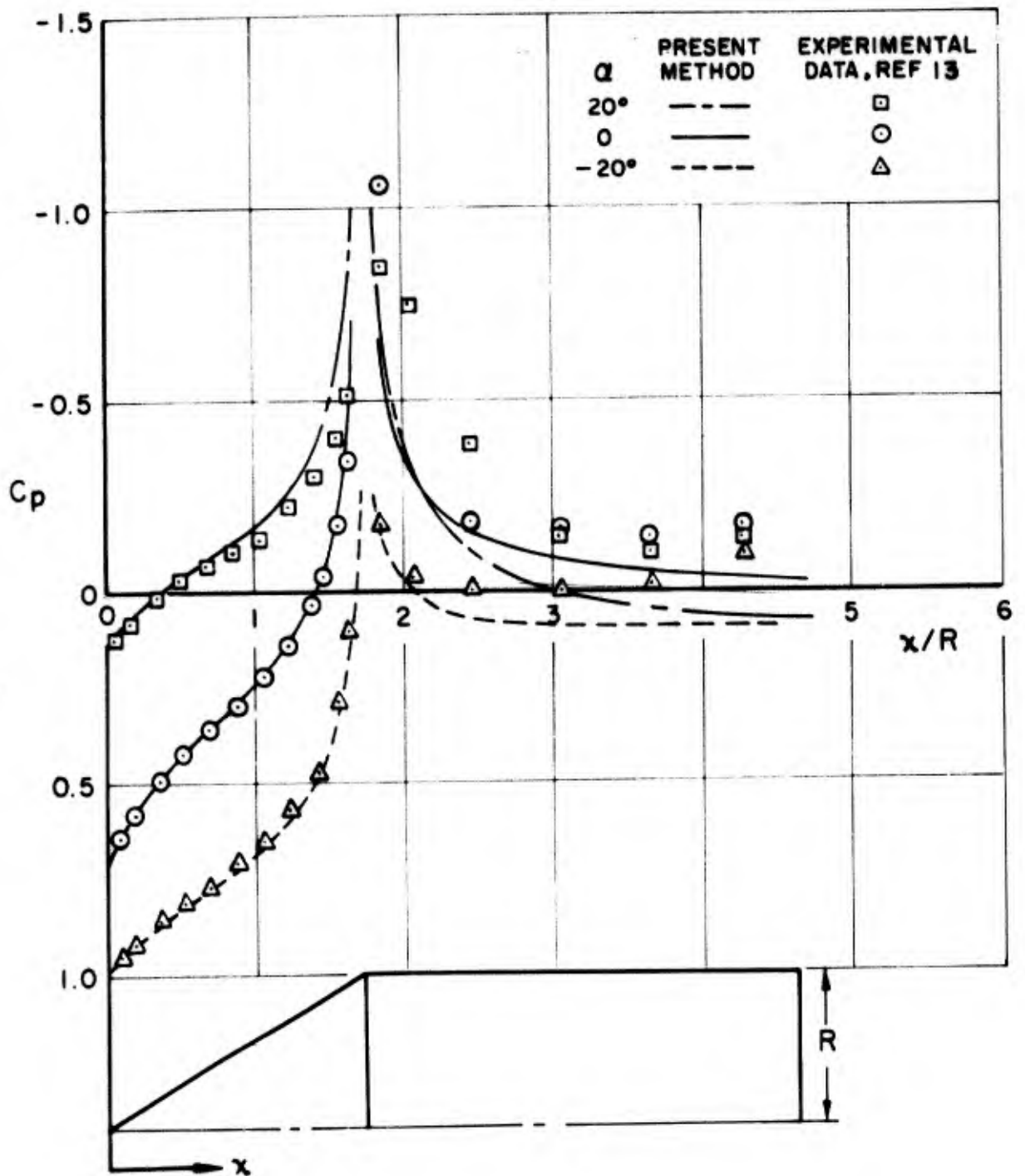


Figure 22. - Comparison of calculated and experimental pressure distributions on a 30° cone-cylinder at 0° and 20° angle of attack.

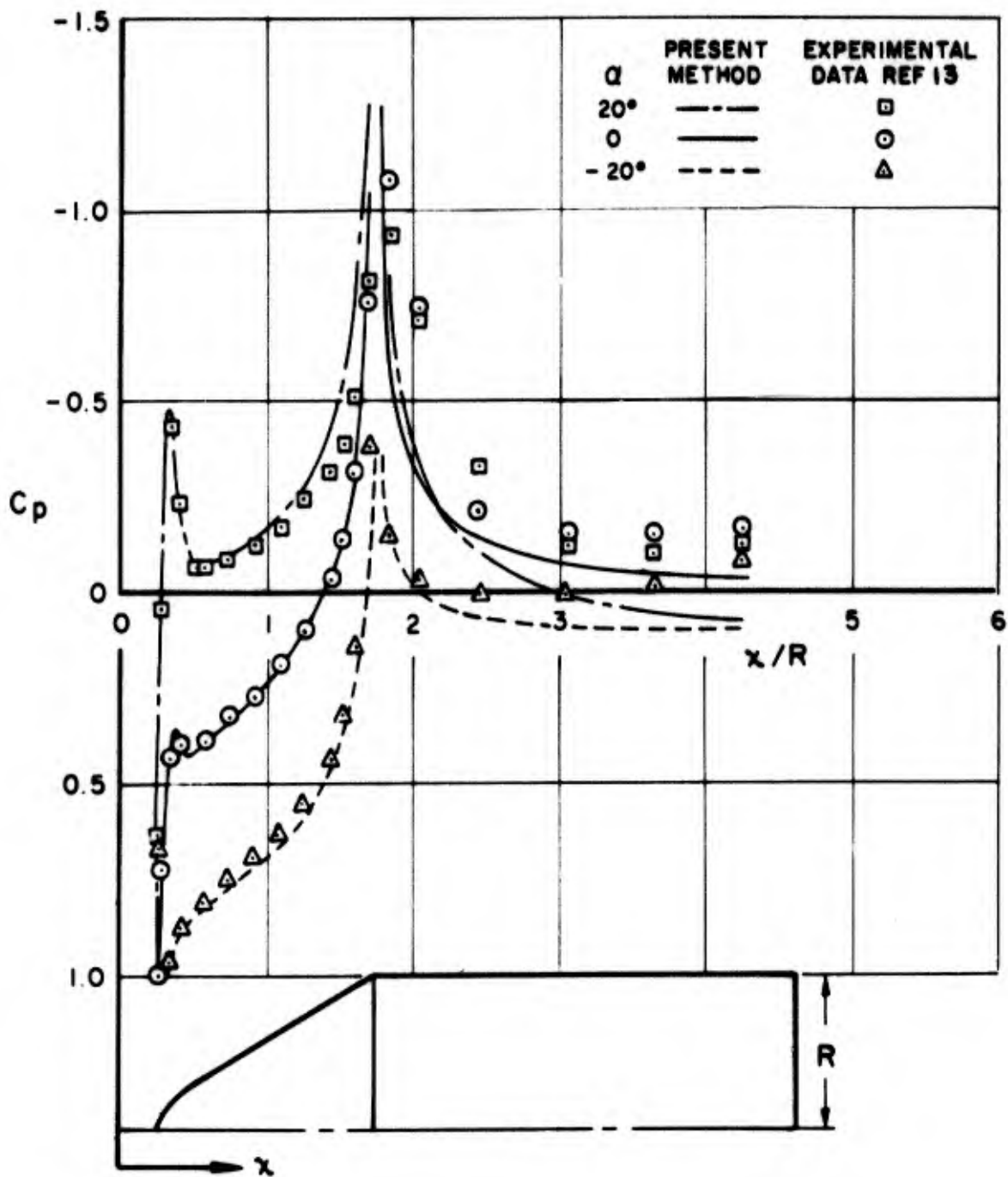


Figure 23. - Comparison of calculated and experimental pressure distributions on a blunted 30° cone-cylinder with nose radius equal to one-fourth final radius at 0° and 20° angle of attack.

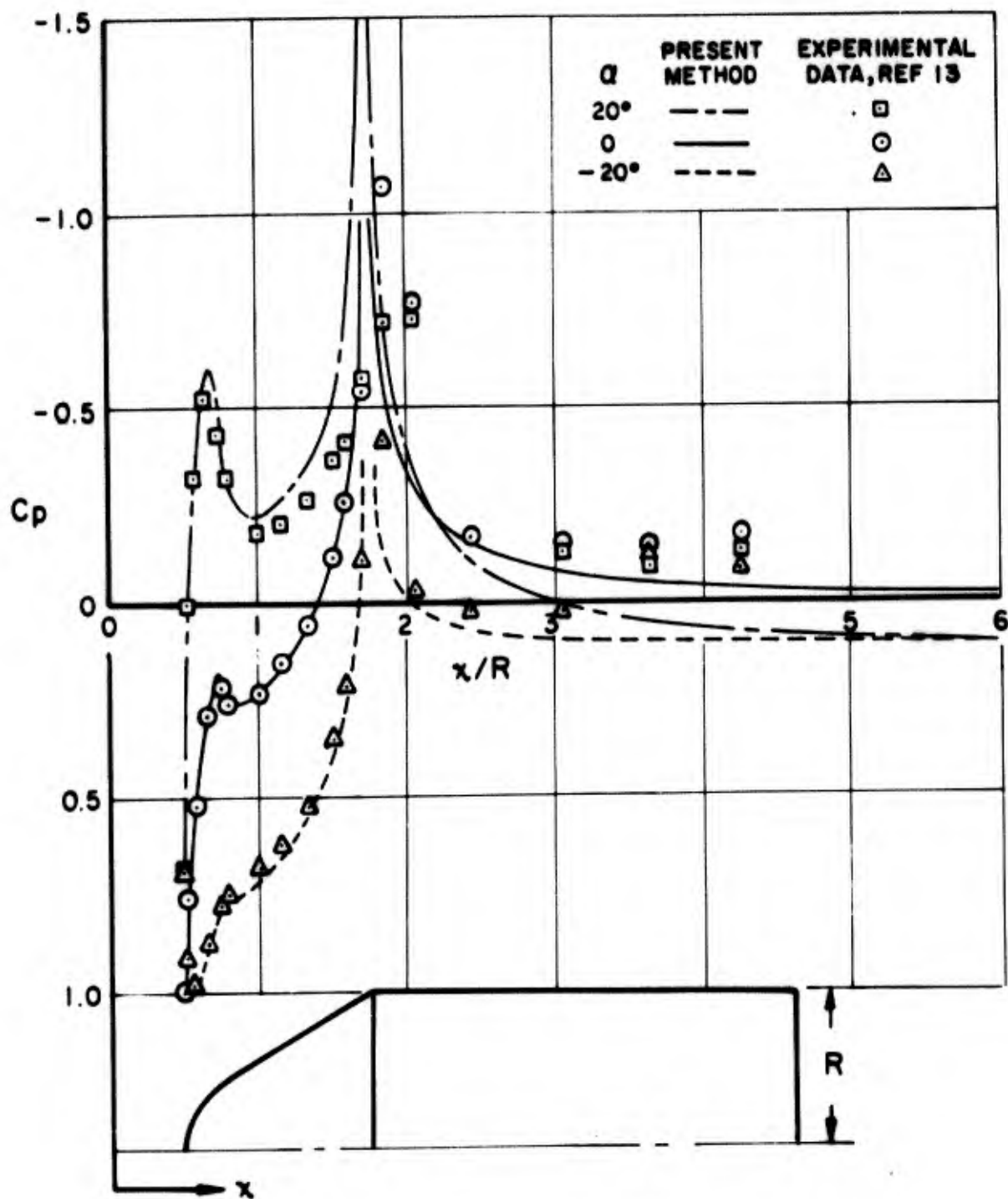


Figure 24. - Comparison of calculated and experimental pressure distributions on a blunted 30° cone-cylinder with nose radius equal to one-half final radius at 0° and 20° angle of attack.

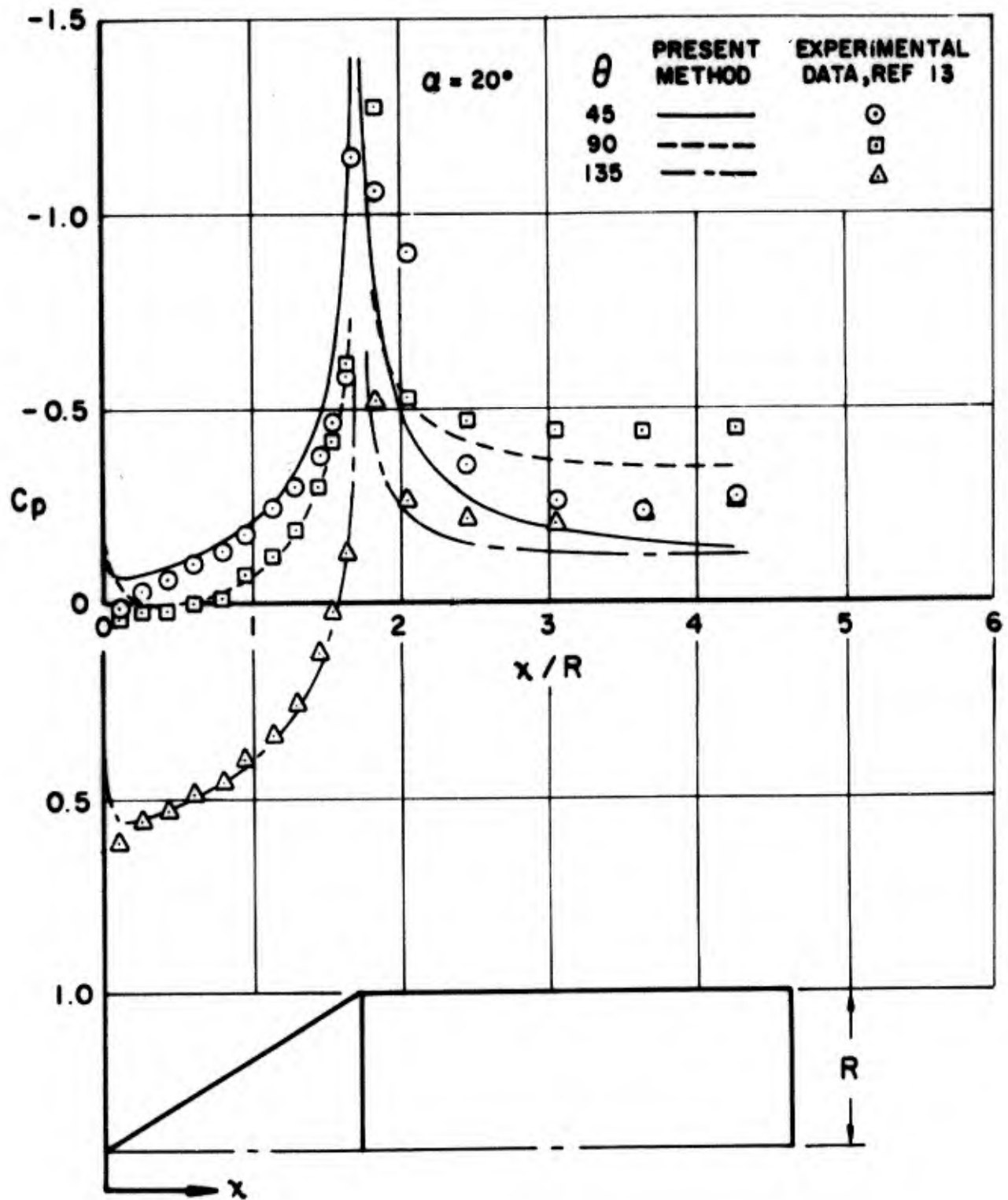


Figure 25. - Comparison of calculated and experimental pressure distributions at various circumferential locations on a 30° cone-cylinder at 20° angle of attack.

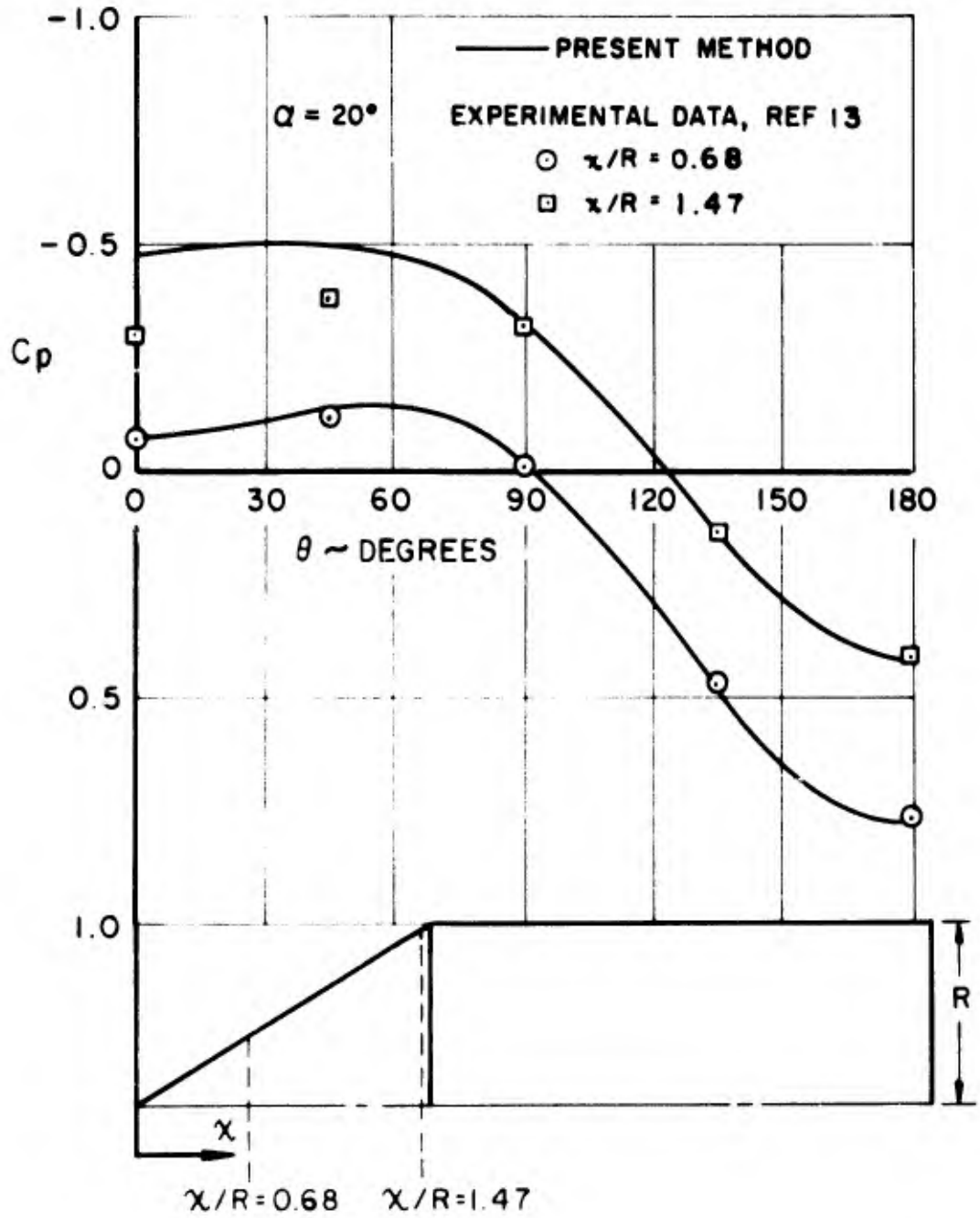


Figure 26 Comparison of calculated and experimental circumferential pressure distributions on a 30° cone cylinder at 20° angle of attack.

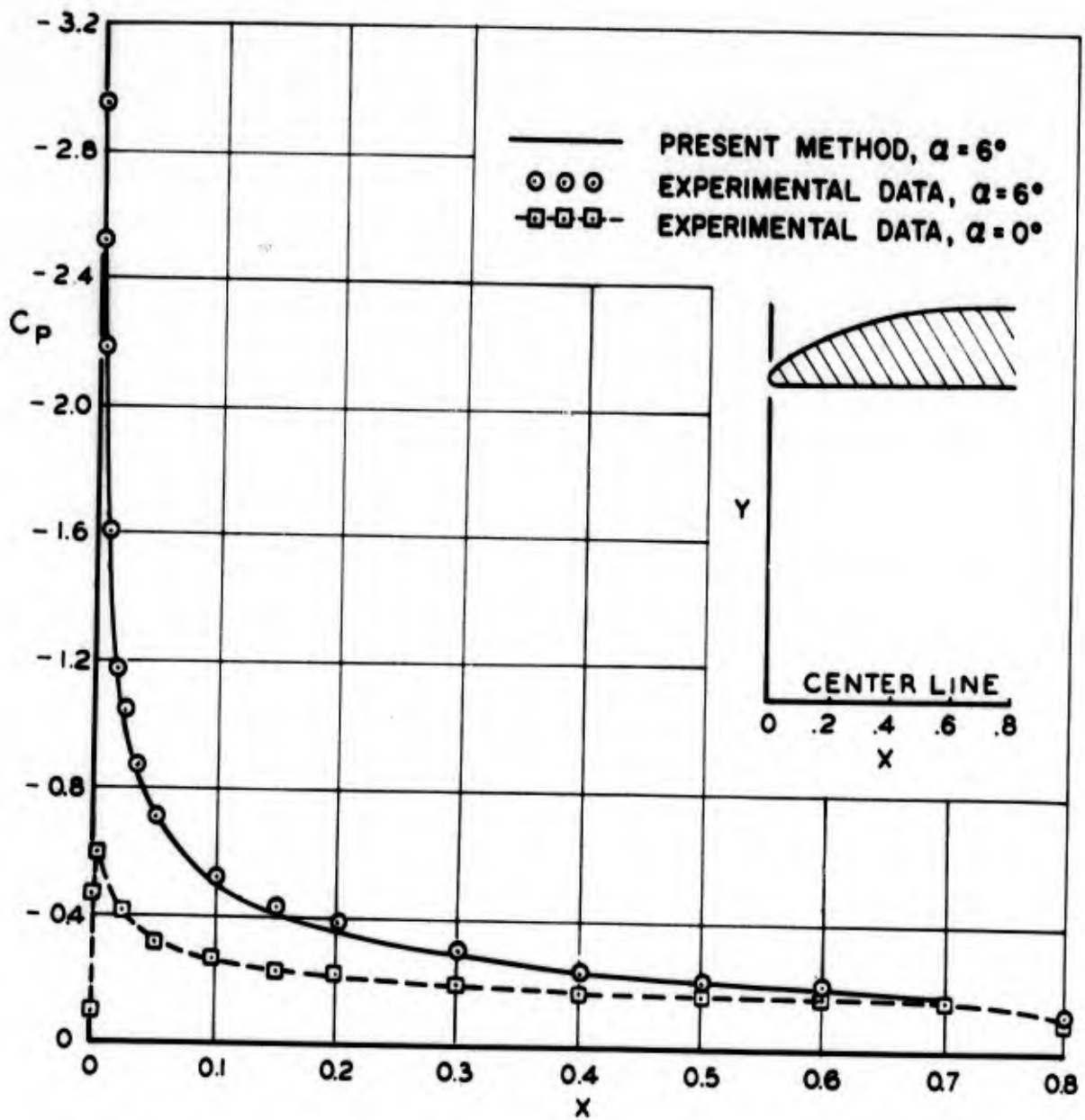


Figure 27. - Comparison of calculated and experimental pressure distributions on the exterior of an inlet lip at 6° angle of attack for a mass flow ratio of 0.44.

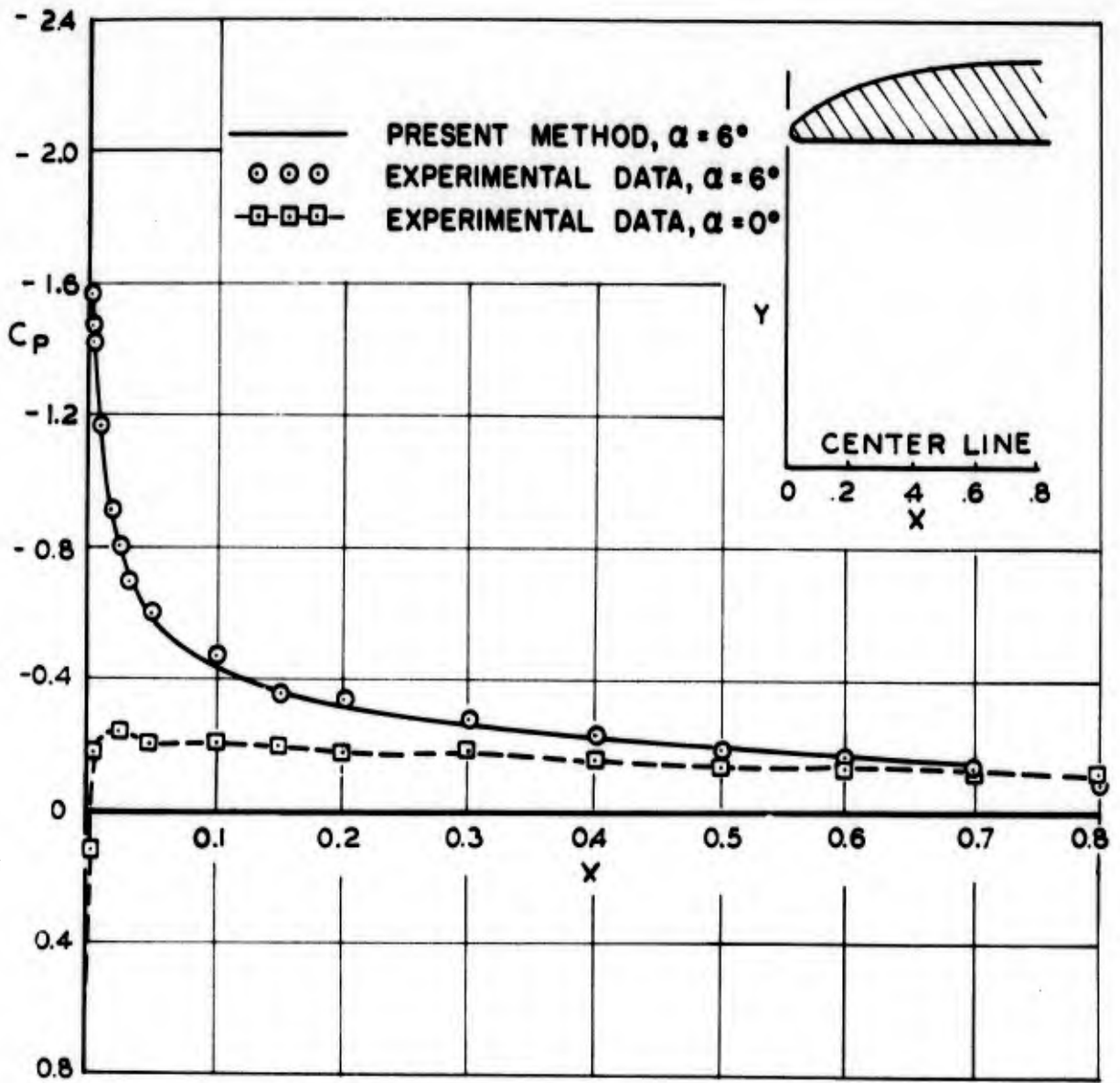


Figure 28. - Comparison of calculated and experimental pressure distributions on the exterior of an inlet lip at 6° angle of attack for a mass flow ratio of 0.52.

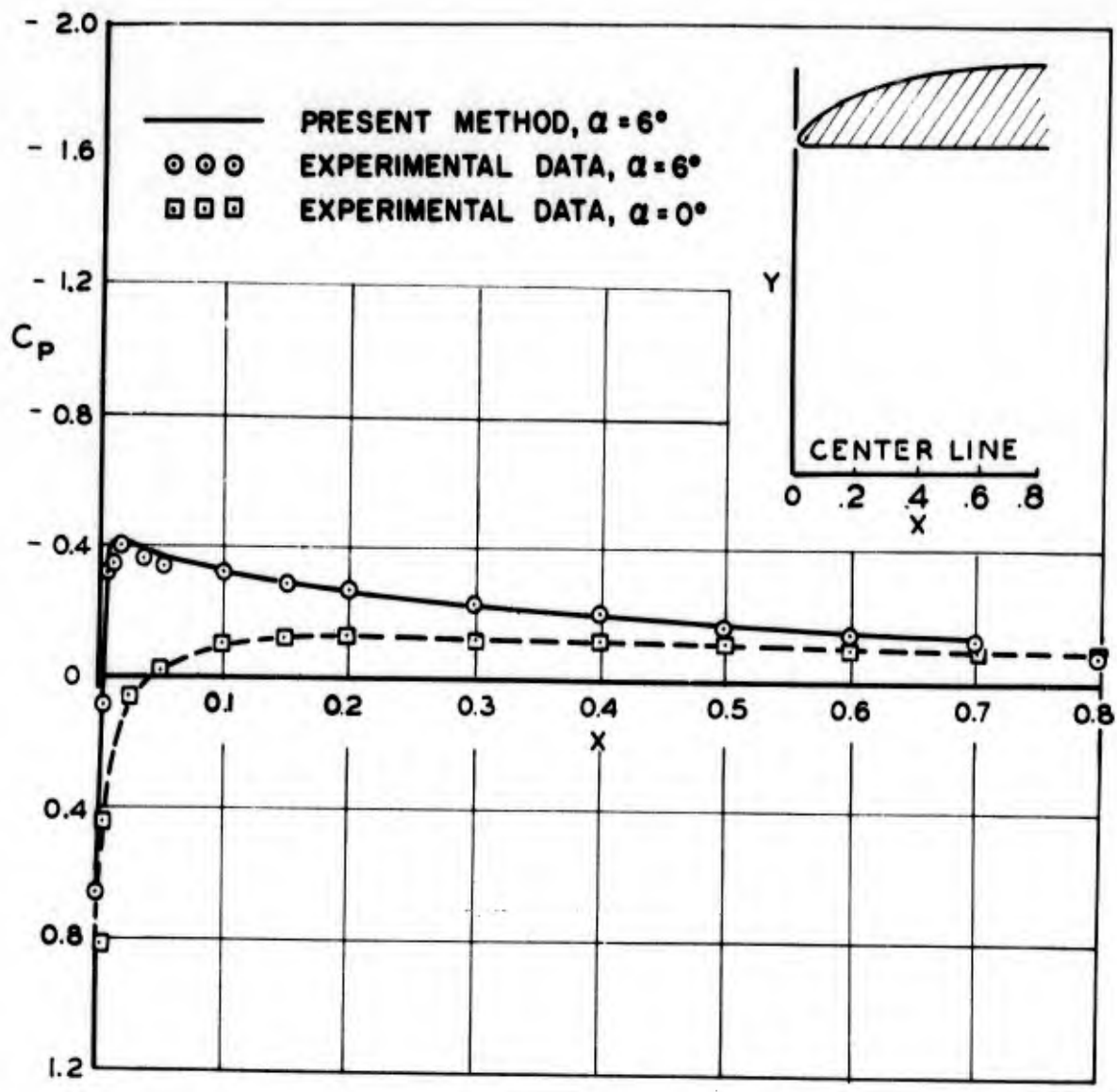


Figure 29. - Comparison of calculated and experimental pressure distributions on the exterior of an inlet lip at 6° angle of attack for a mass flow ratio of 0.73.

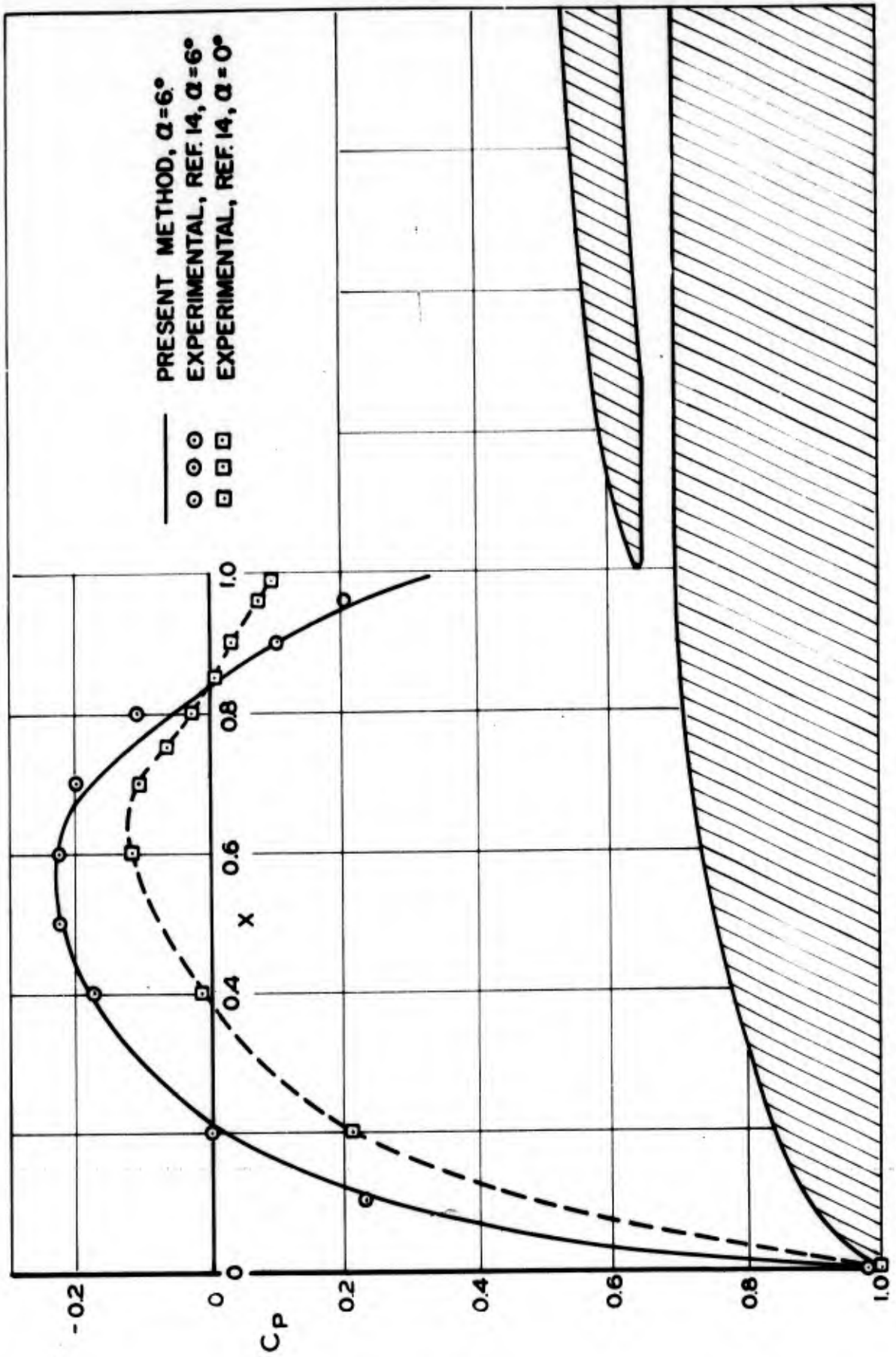


Figure 30. - Comparison of calculated and experimental pressure distributions at 6° angle of attack on an NACA 1-60-060 spinner in an NACA 1-70-100 cowling.

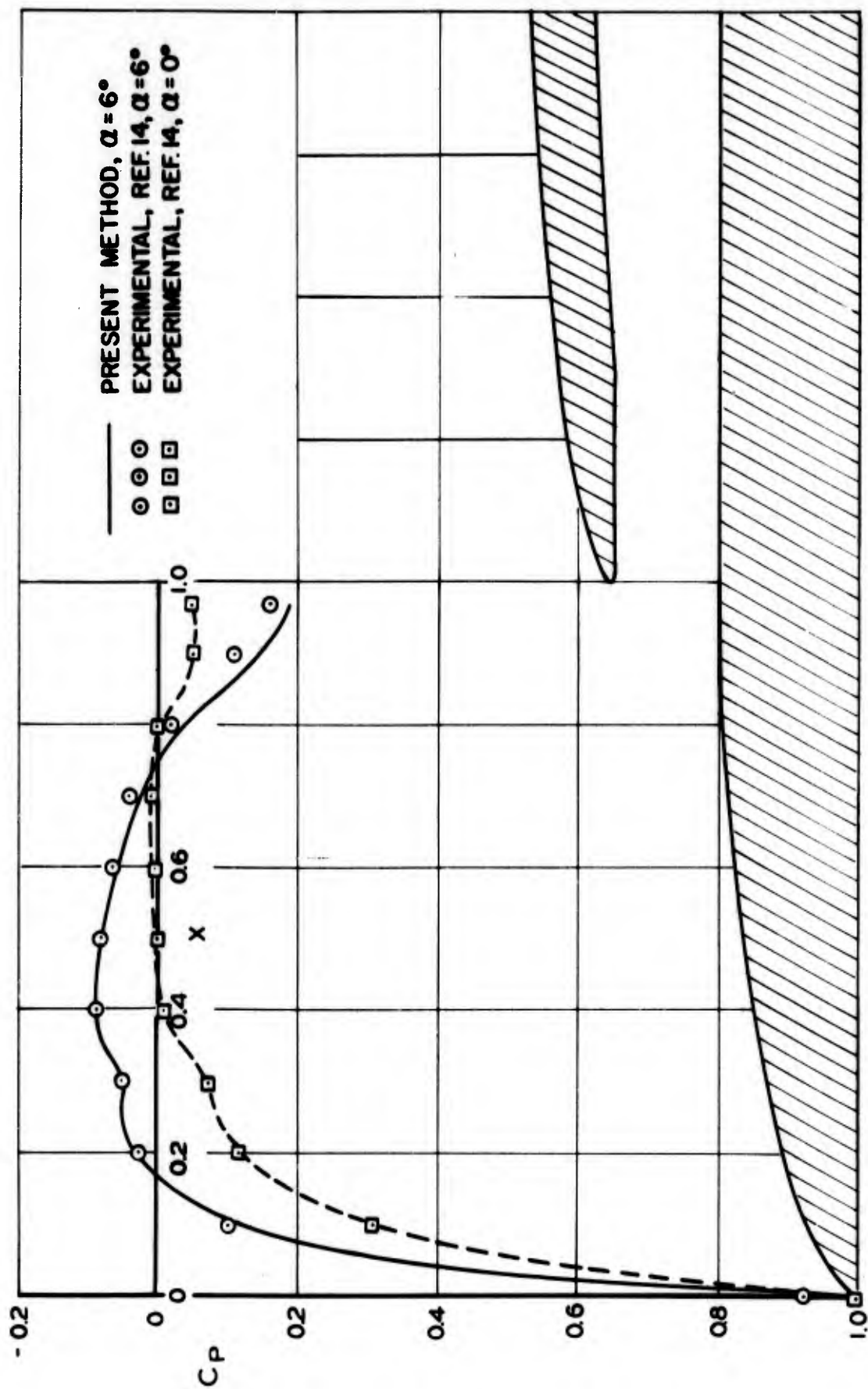


Figure 31. - Comparison of calculated and experimental pressure distributions at 6° angle of attack on an NACA 1-40-060 spinner in an NACA 1-70-100 cowling.

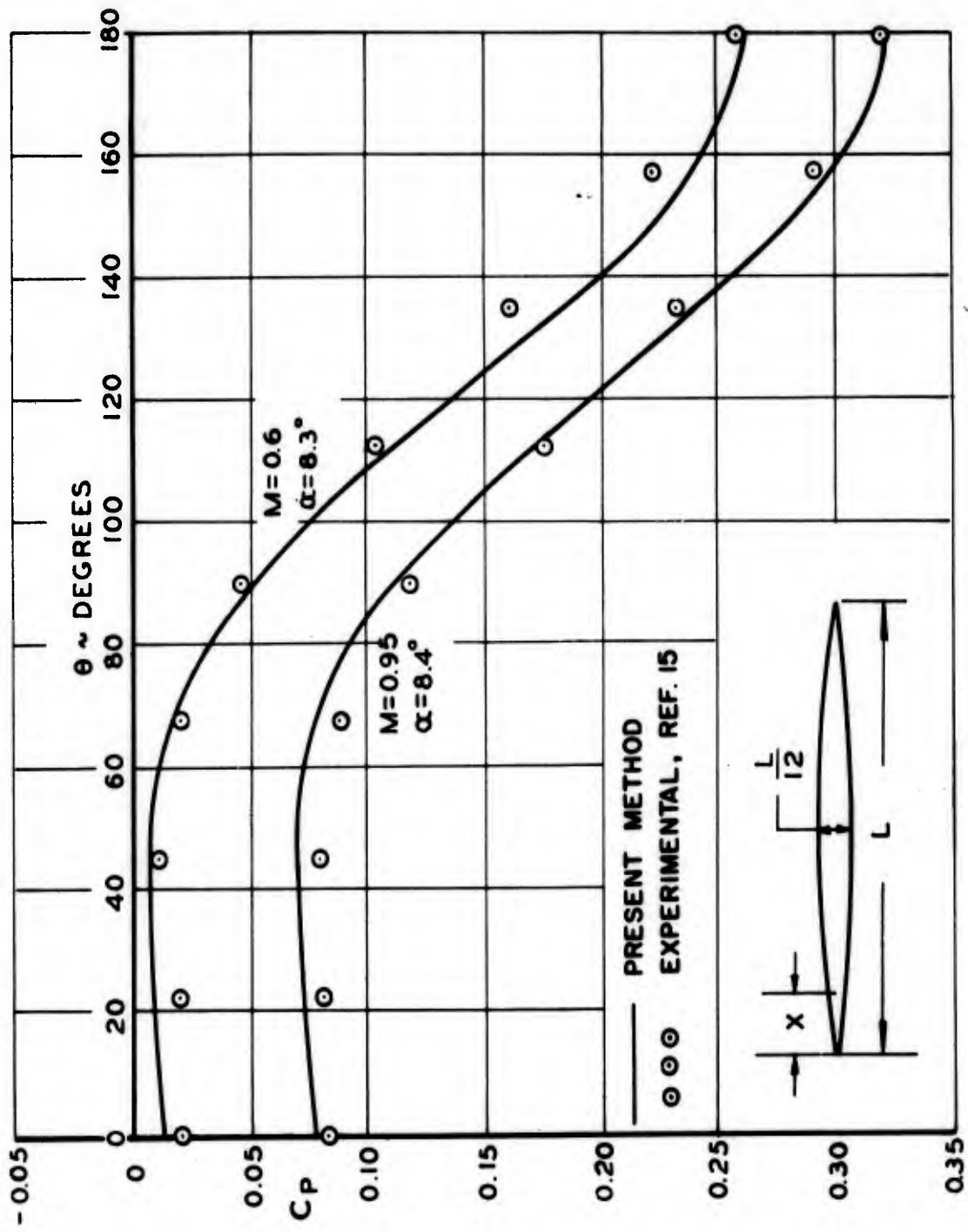


Figure 32. - Comparison of calculated and experimental circumferential pressure distributions at two Mach numbers on a slender body at angle of attack. $x/L = 0.017$.

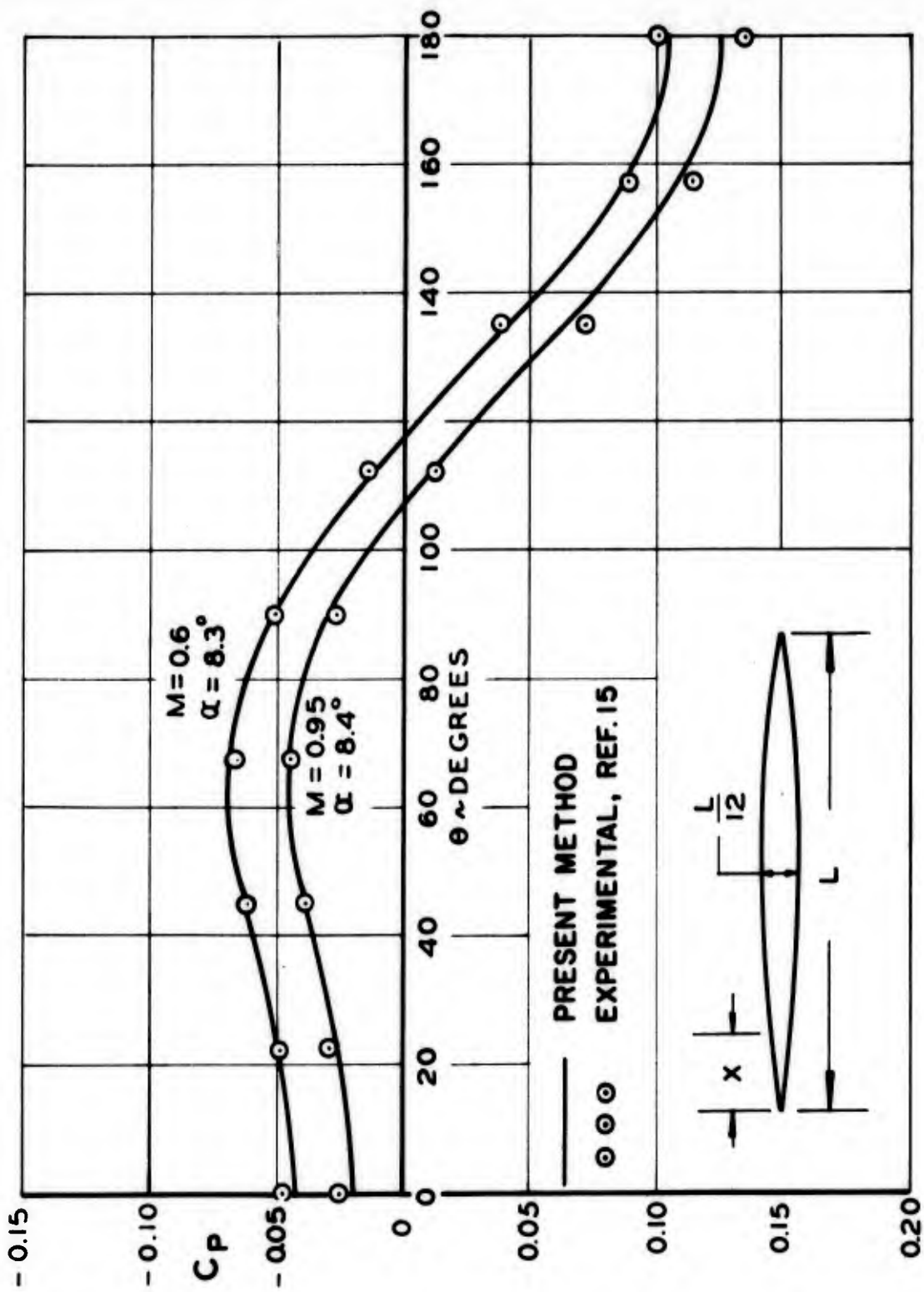


Figure 33. - Comparison of calculated and experimental circumferential pressure distributions at two Mach numbers on a slender body at angle of attack. $x/L = 0.100$.

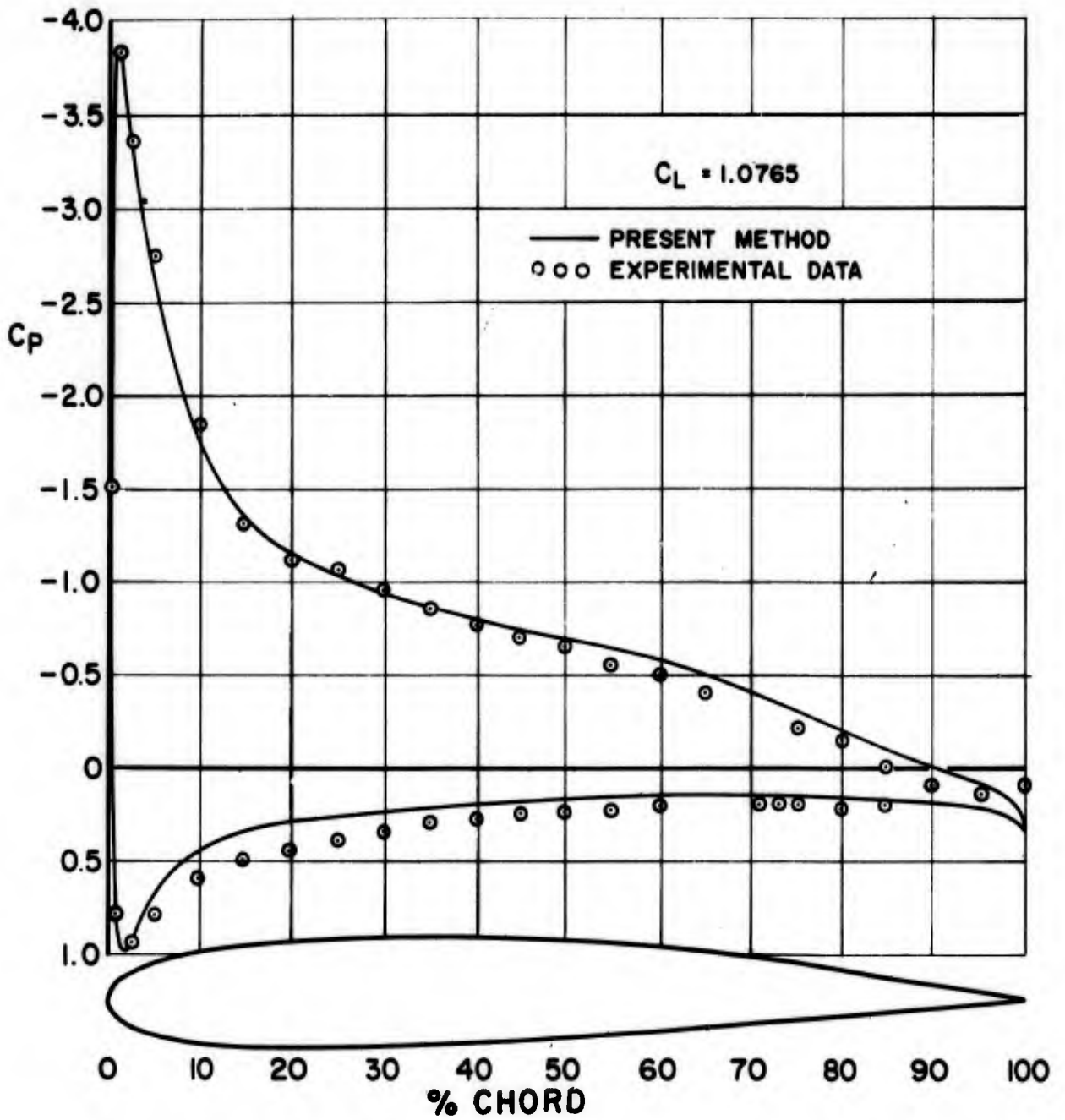


Figure 34. - Comparison of calculated and experimental pressure distributions on a DSMA 387 airfoil at $C_L = 1.0765$.



— PRESENT METHOD
 ○ ○ ○ EXPERIMENTAL DATA, REF. 16

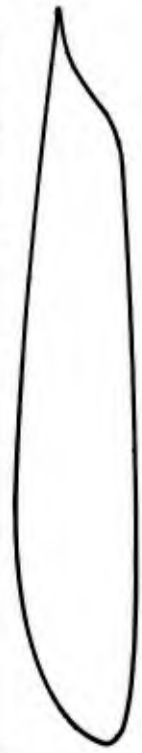
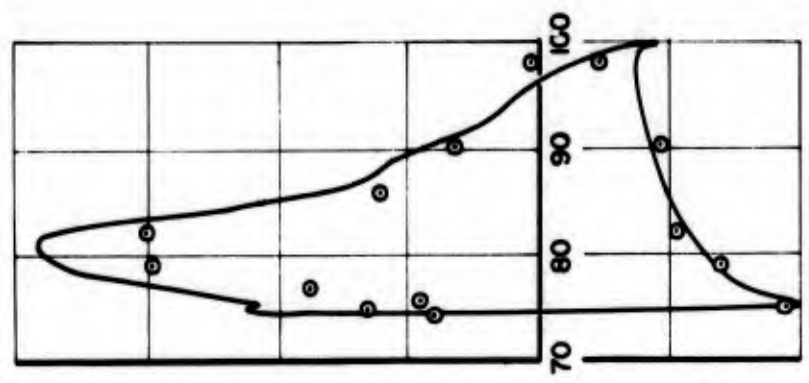
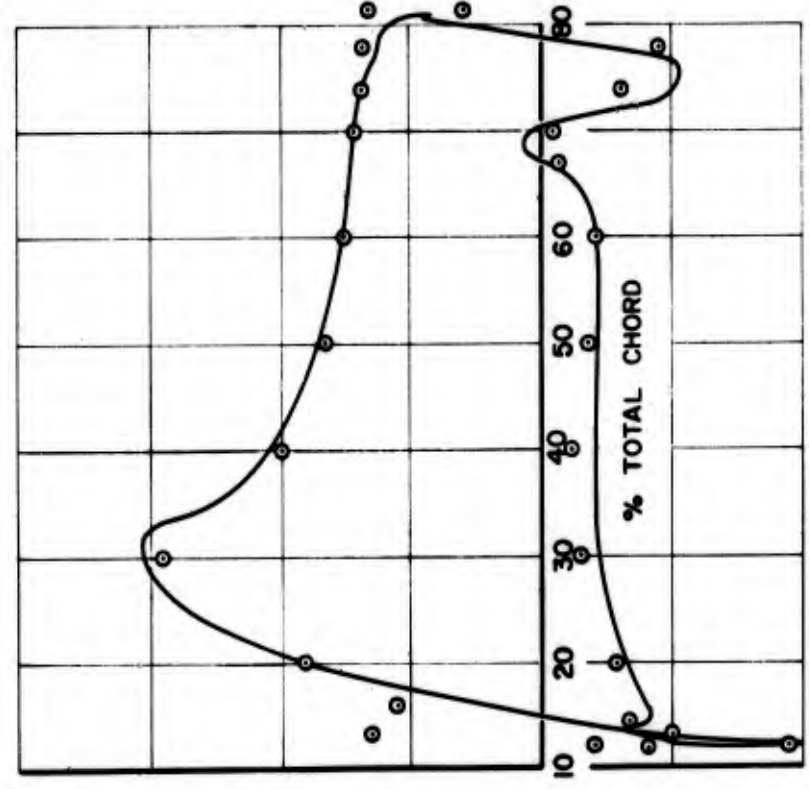
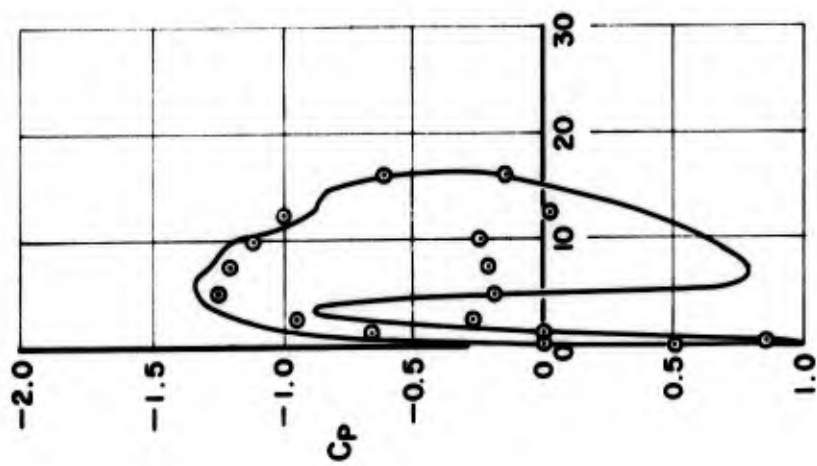


Figure 35. - Comparison of calculated and experimental pressure distributions on an NACA 23012 airfoil with fixed slot and deflected slotted flap at angle of attack. Flap deflection 20°, angle of attack 0°.

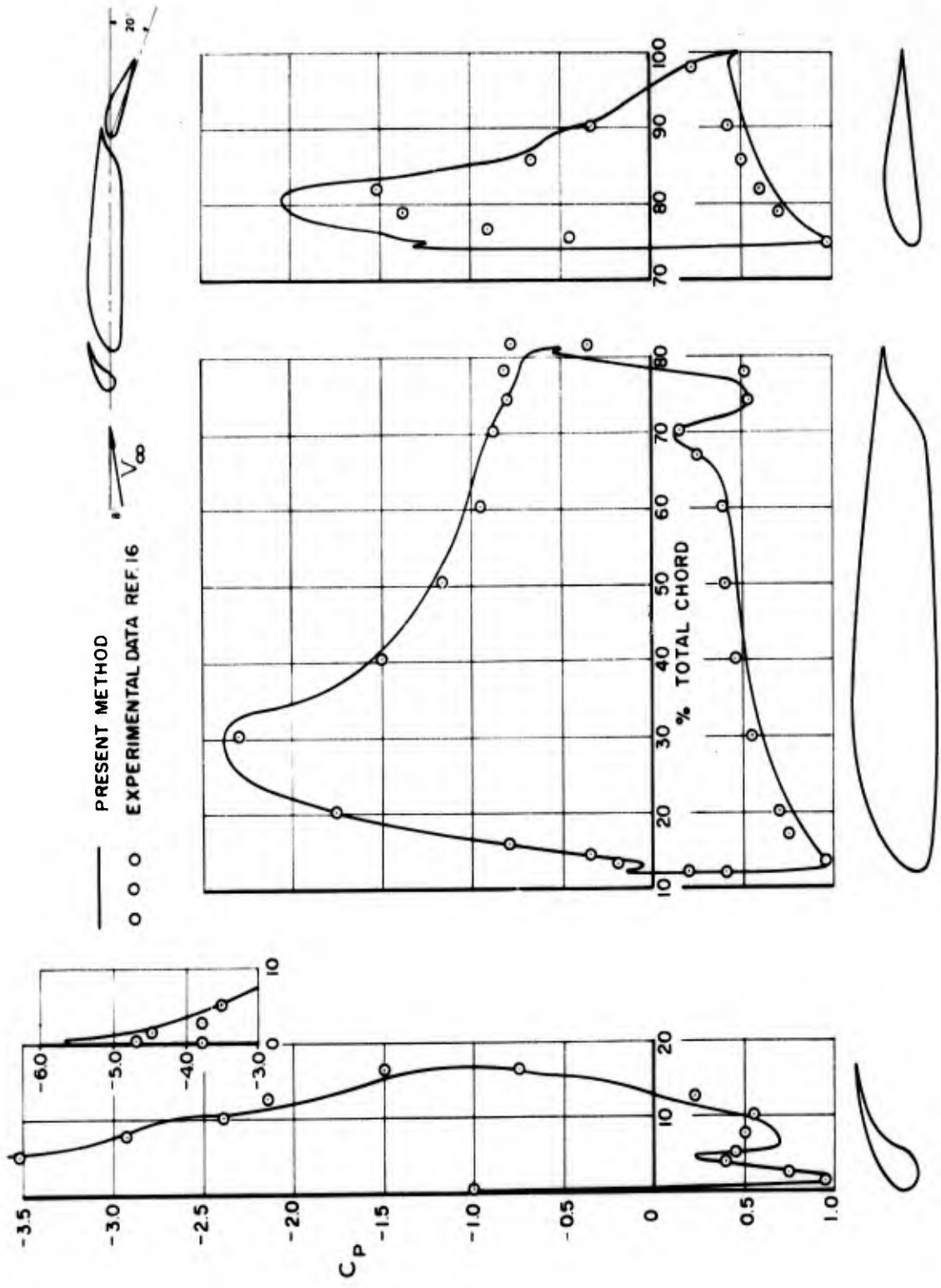


Figure 36. - Comparison of calculated and experimental pressure distributions on an NACA 23012 airfoil with fixed slot and deflected slotted flap at angle of attack. Flap deflection 20° , angle of attack 8° .

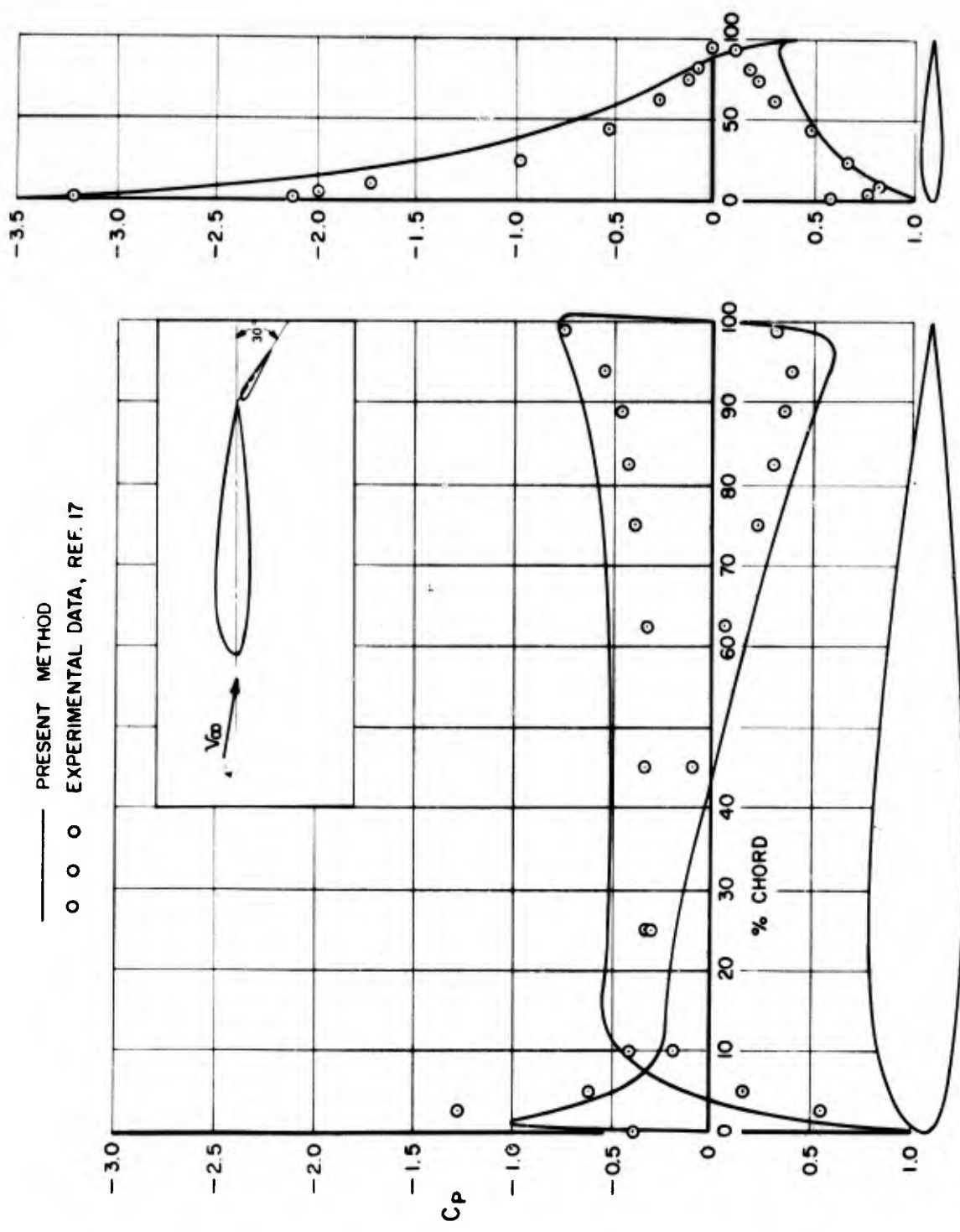


Figure 37. - Comparison of calculated and experimental pressure distributions on an NACA 23012 airfoil with a deflected external 23012 airfoil flap. Flap deflection 30° , angle of attack -4.02° .

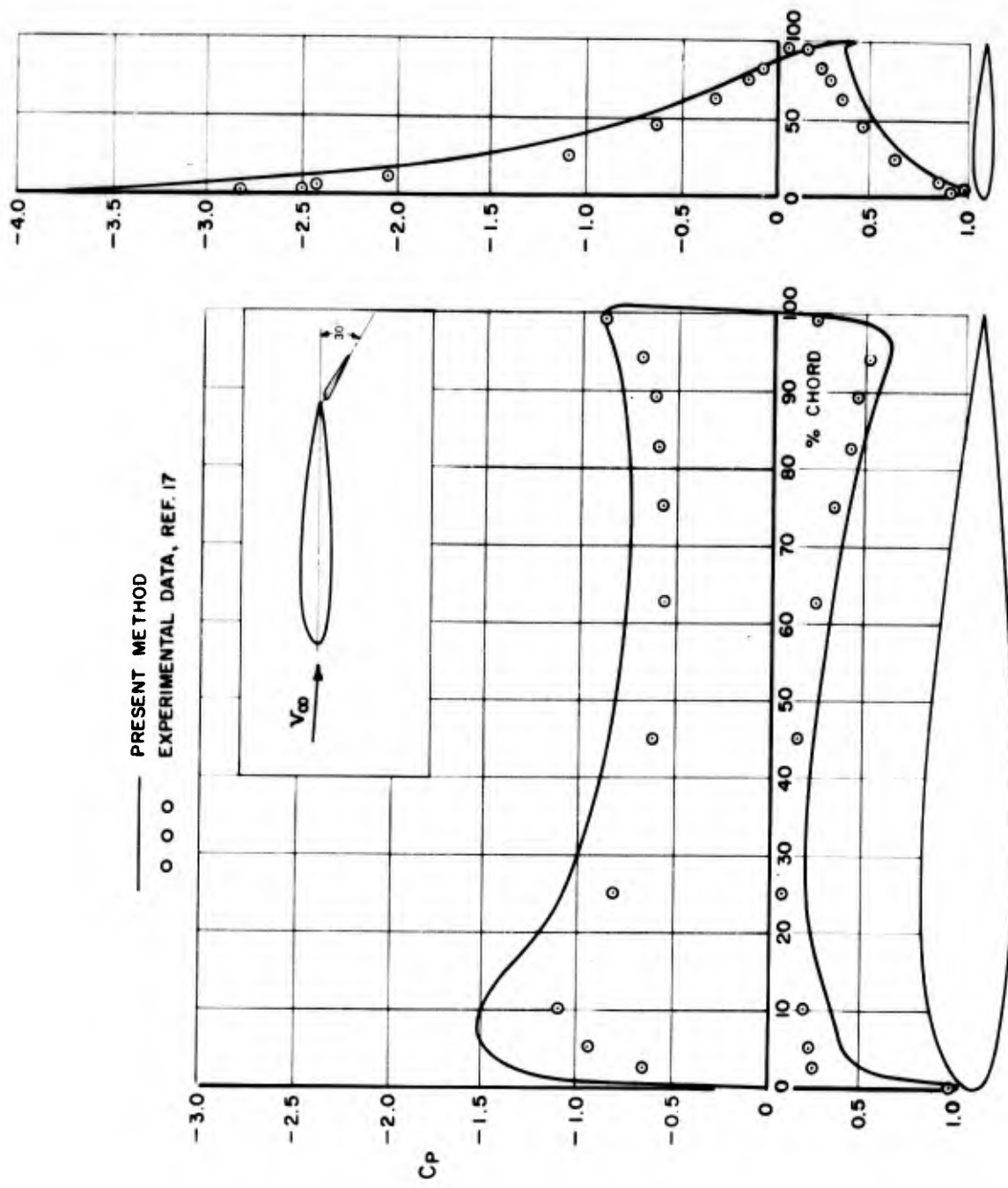


Figure 38. - Comparison of calculated and experimental pressure distributions on an NACA 23012 airfoil with a deflected external flap. Flap deflection 30° , angle of attack -9.420° .

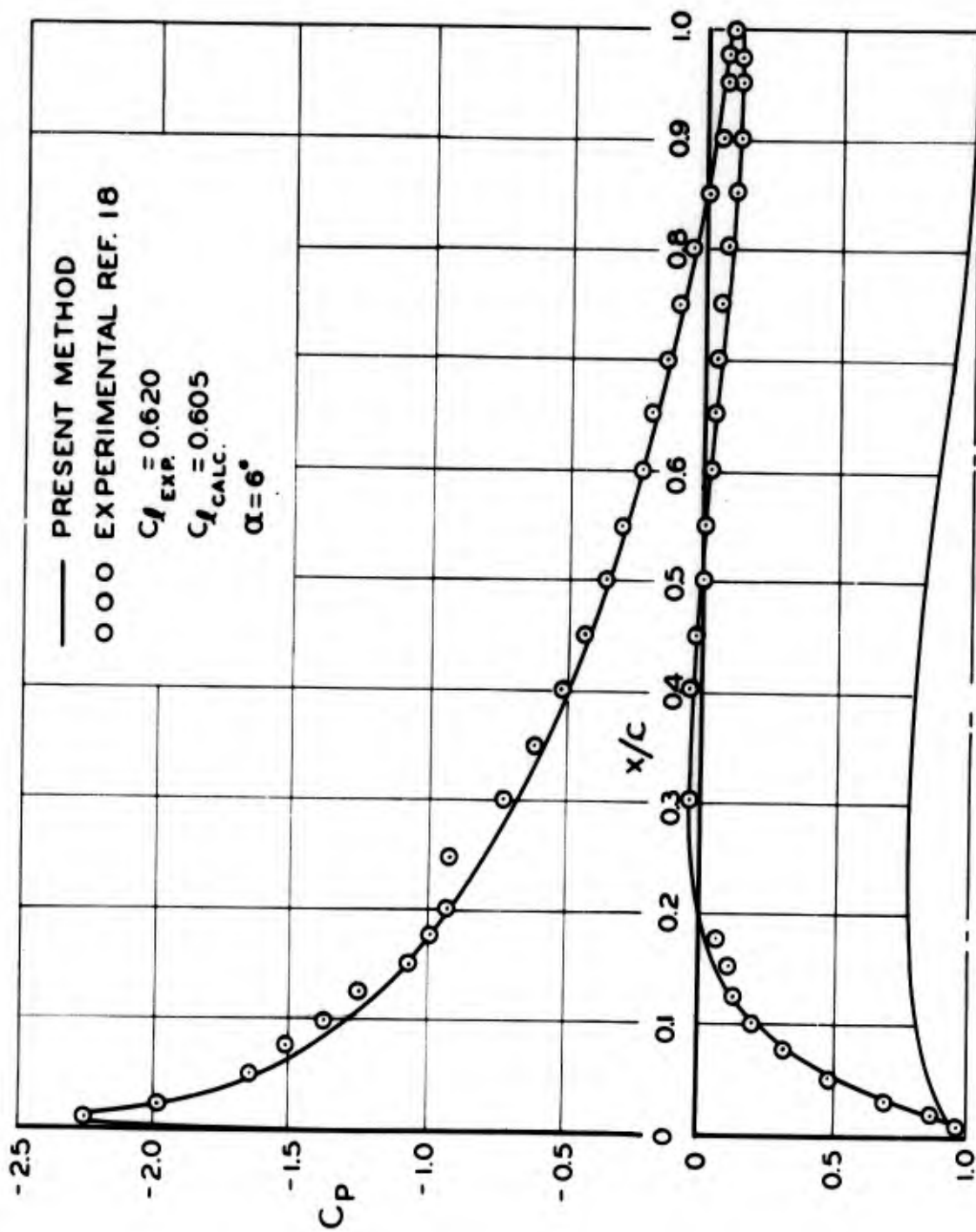


Figure 39. - Comparison of calculated and experimental pressure distributions on an 11.8 percent-thick symmetric Joukowski airfoil at 6° angle of attack.

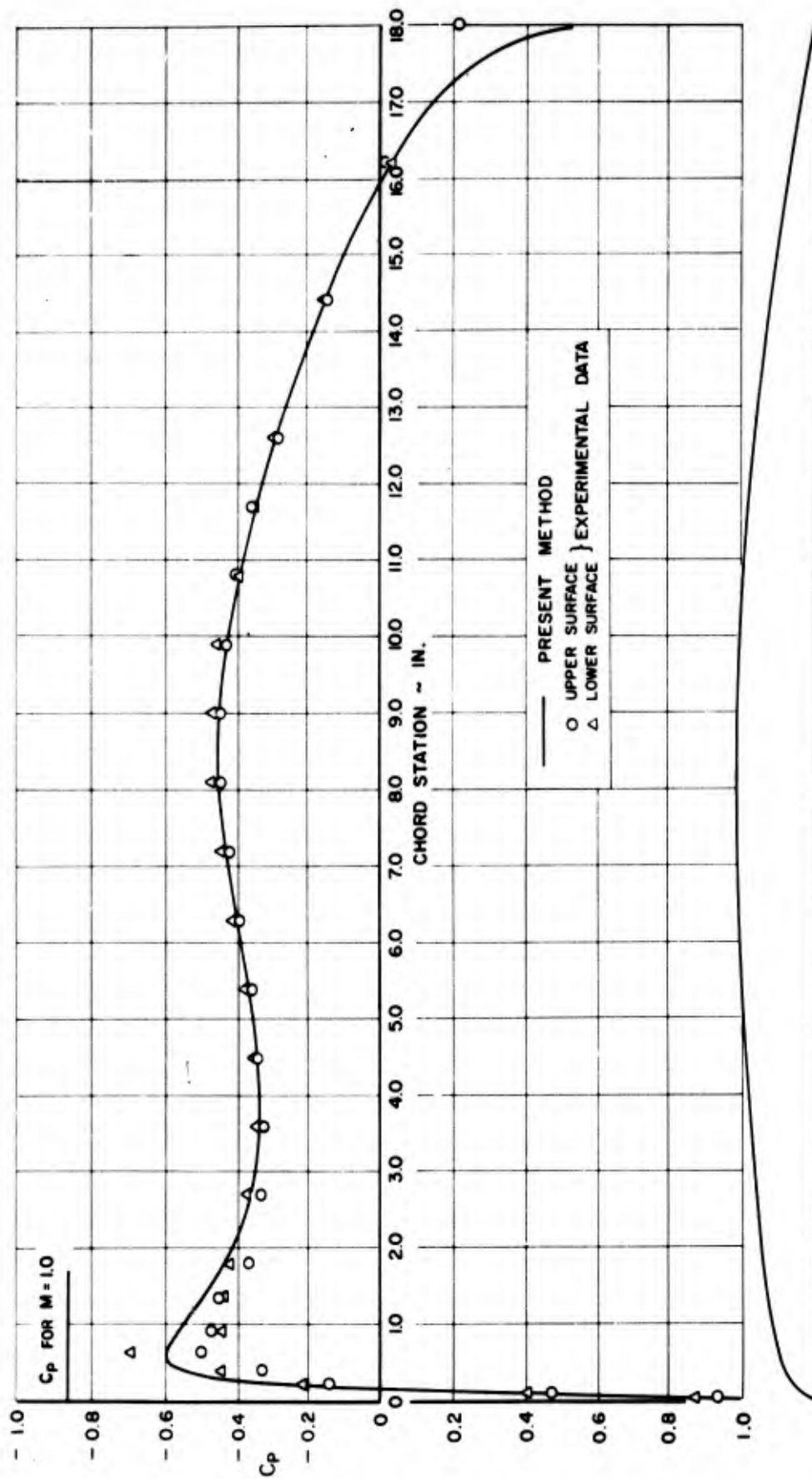


Figure 40. - Comparison of calculated and experimental pressure distributions on a DSMA 299 symmetric airfoil at 0° angle of attack and at a Mach number of 0.680.

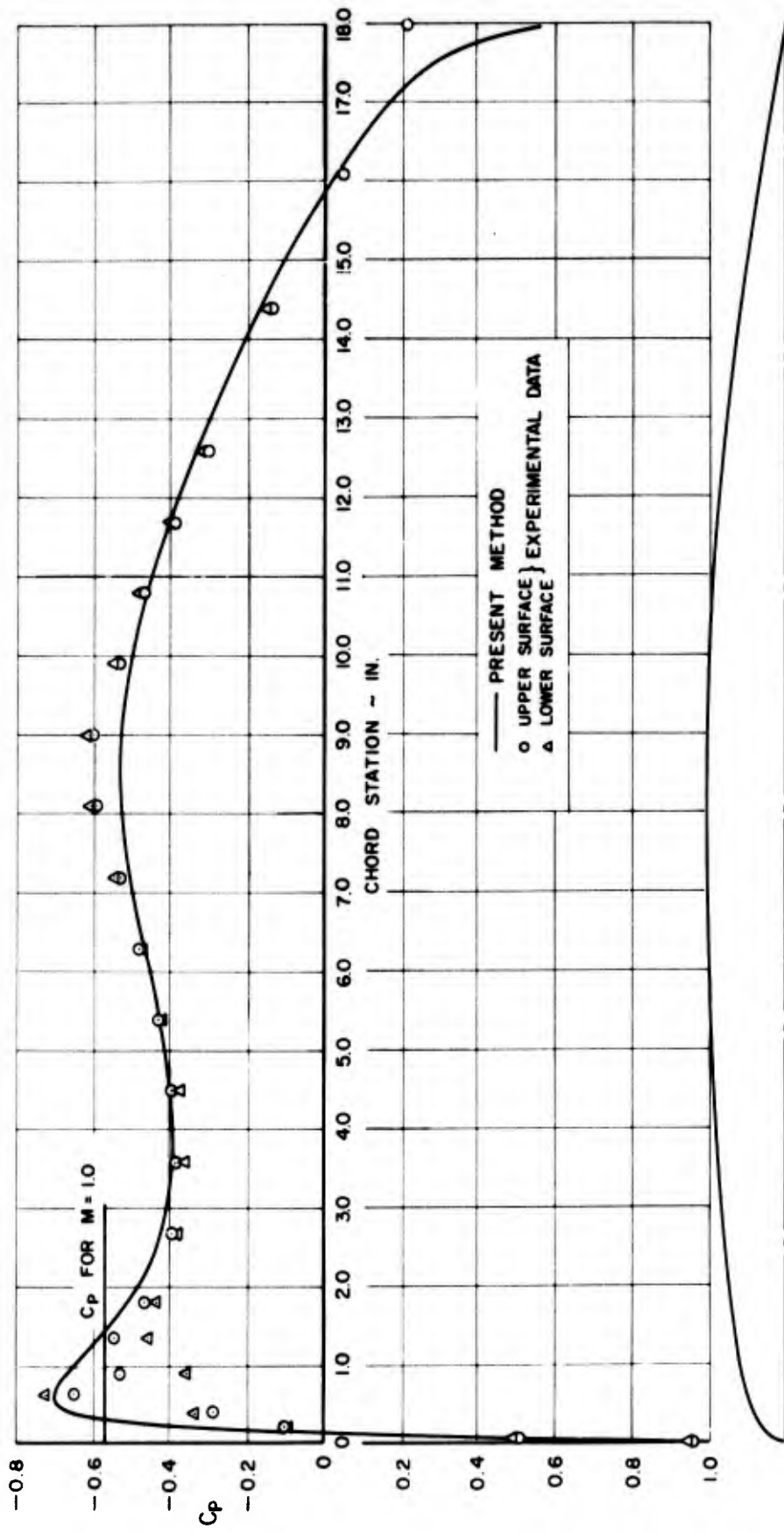


Figure 41. - Comparison of calculated and experimental pressure distributions on a DSMA 299 symmetric airfoil at 0° angle of attack and at a Mach number of 0.757.

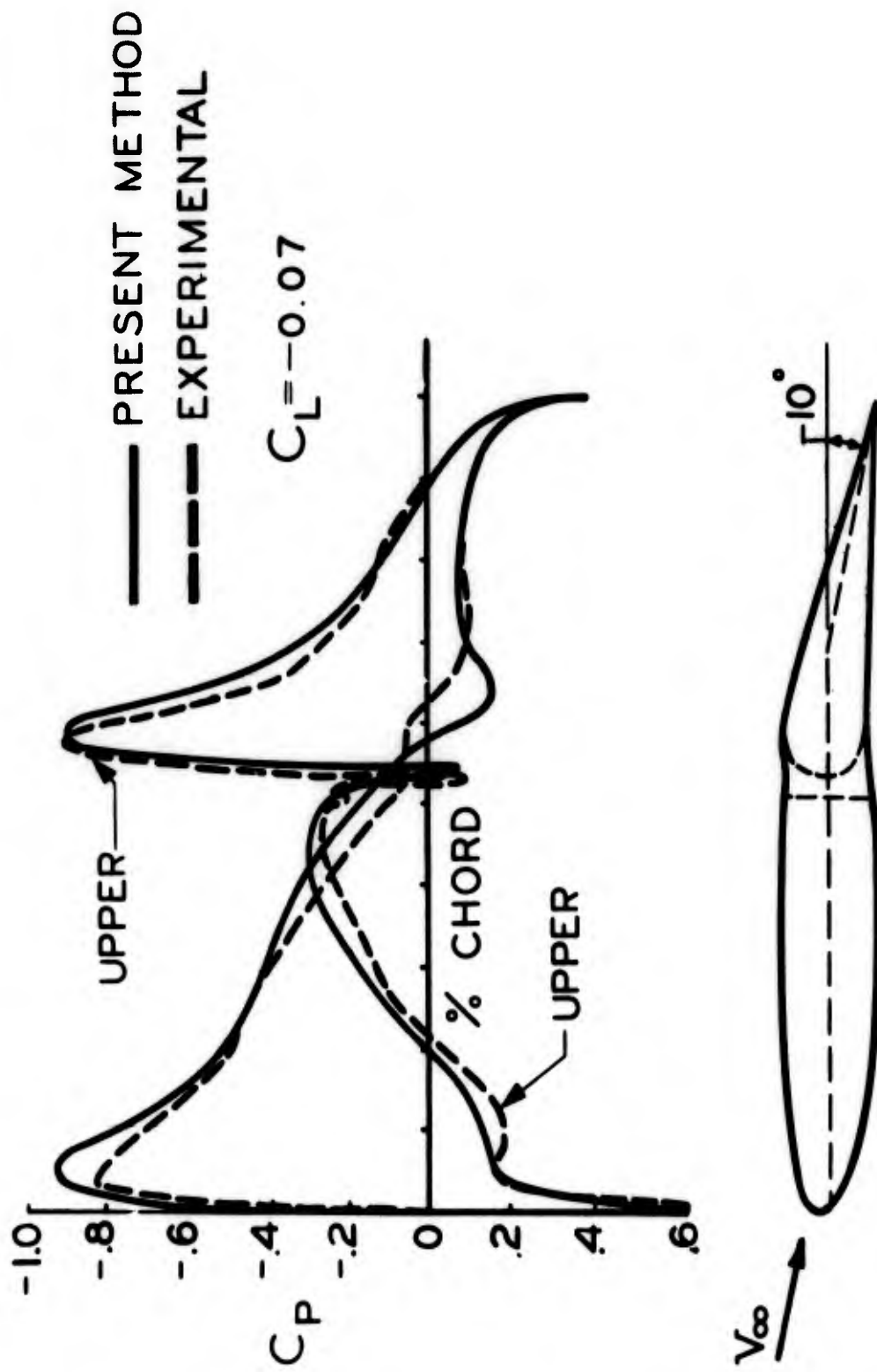


Figure 42. - Comparison of calculated and experimental pressure distributions on a horizontal tail with deflected elevator at a lift coefficient of -0.07 and Mach number of 0.5 .

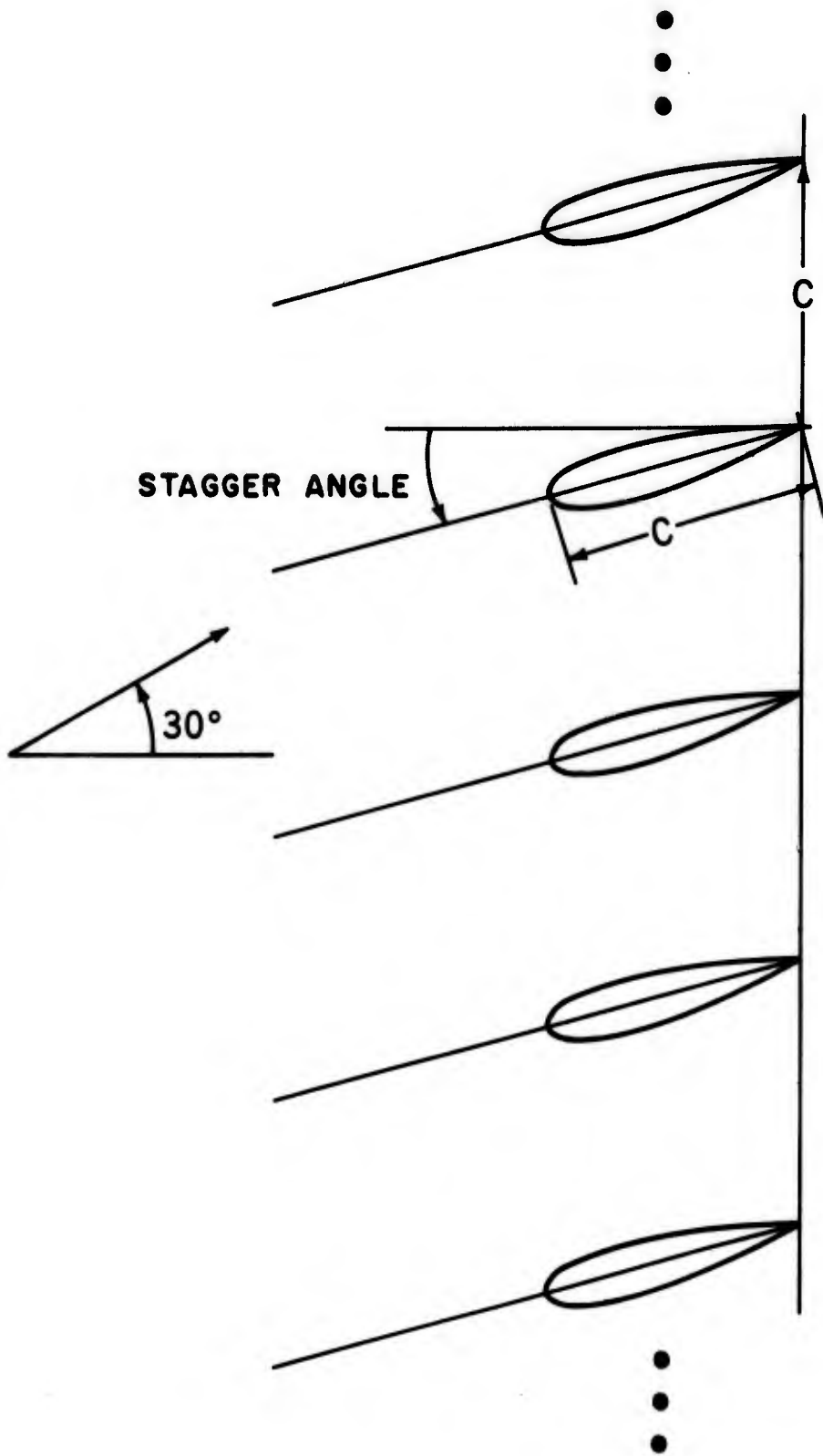


Figure 43. - Geometrical arrangement of a typical infinite cascade showing stagger angle and an inlet angle of attack of 30° .

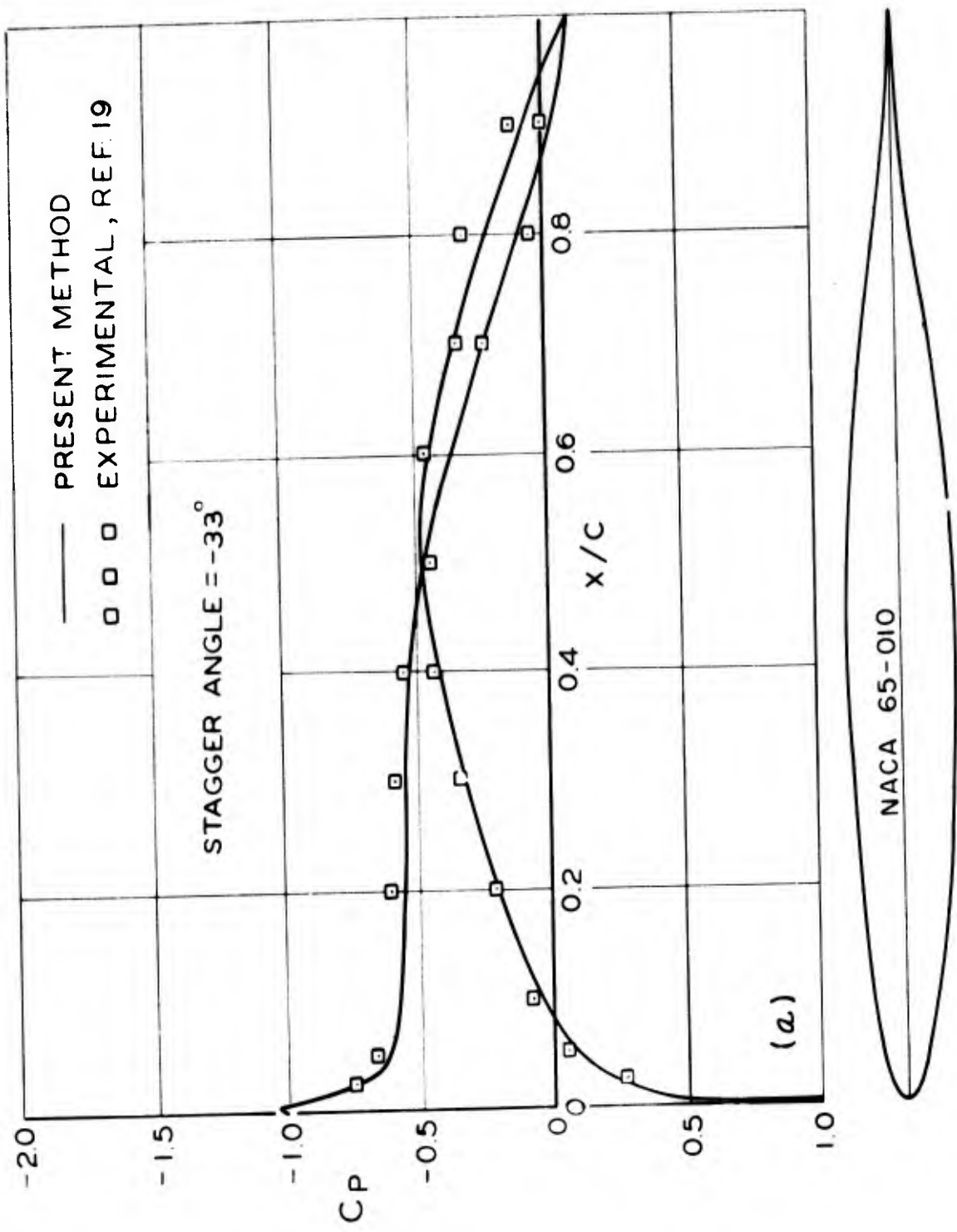


Figure 44. - Comparison of calculated and experimental pressure distributions on a symmetrical NACA 65-010 airfoil in cascade at an inlet angle of attack of 30° and stagger angle of -33° .

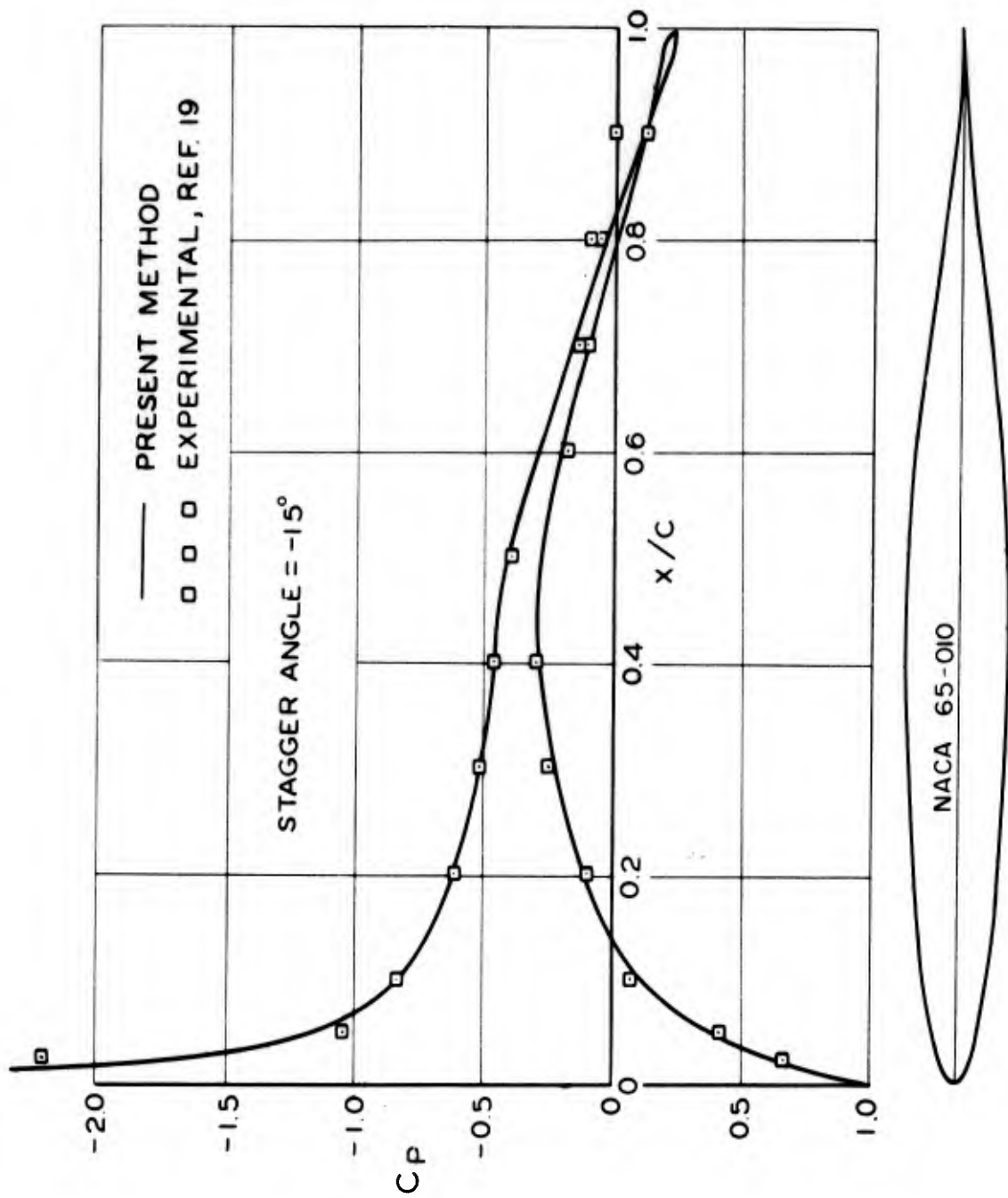


Figure 45. - Comparison of calculated and experimental pressure distributions on a symmetrical NACA 65-010 airfoil in cascade at an inlet angle of attack of 30° and stagger angle of -15° .

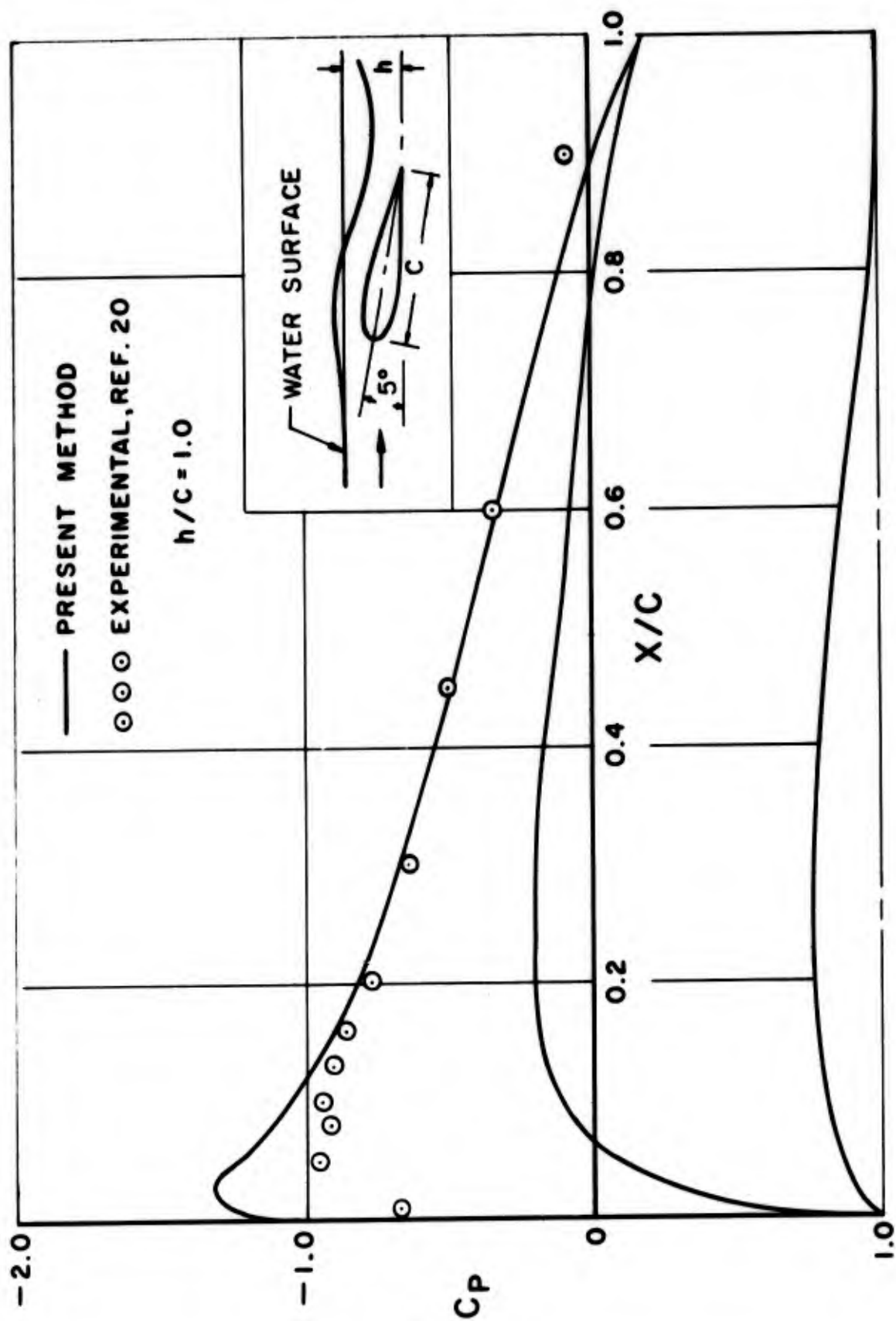


Figure 46. - Comparison of calculated and experimental pressure distributions on a 12 percent-thick symmetric Joukowski hydrofoil at 5° angle of attack, Froude number of 0.95 and a depth of 1 chord. Depth measured from trailing edge.

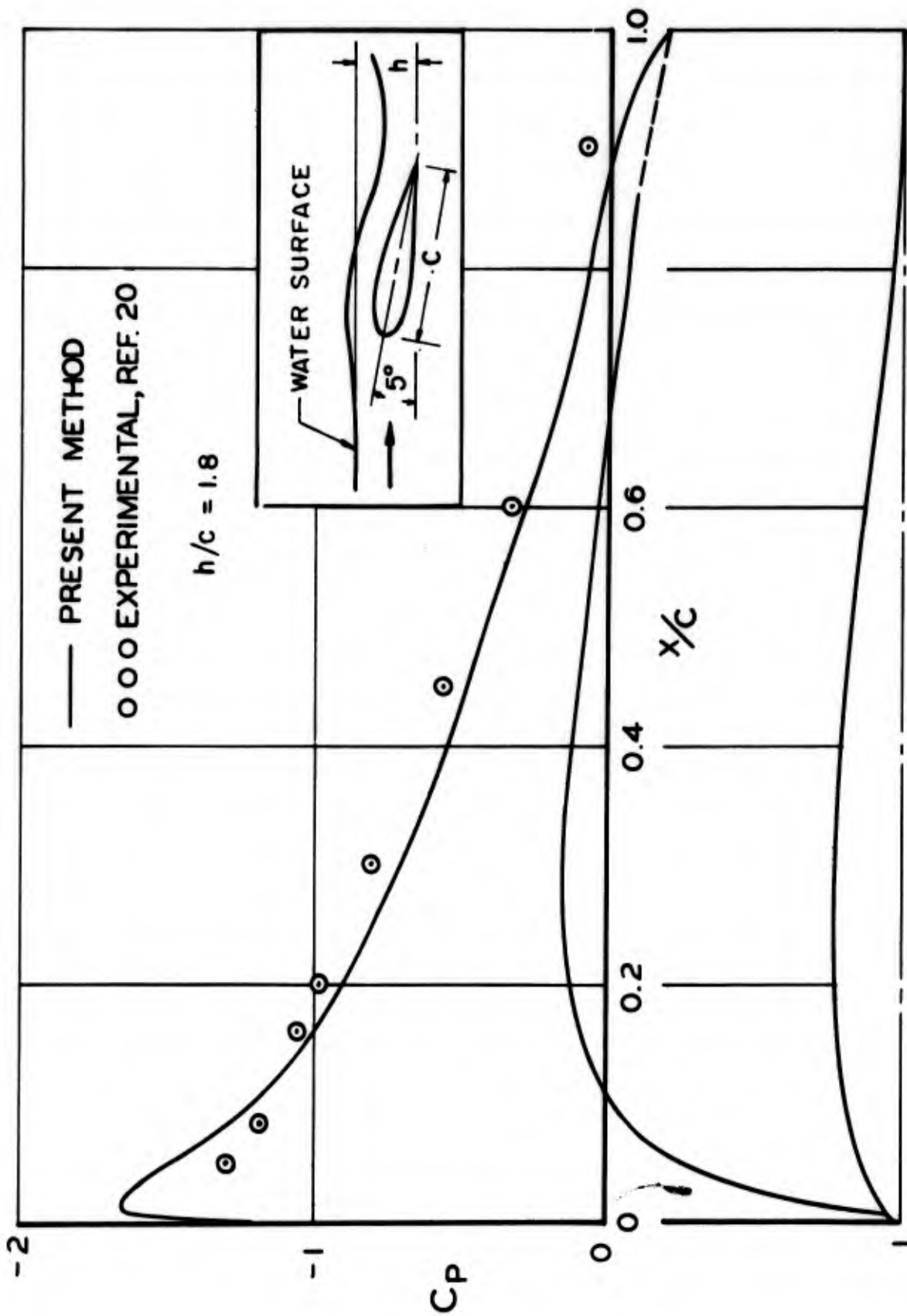


Figure 47. - Comparison of calculated and experimental pressure distributions on a 12 percent-thick symmetric Joukowski hydrofoil at 5° angle of attack, Froude number of 0.95 and a depth of 1.8 chord. Depth measured from trailing edge.

SECTION SHAPE- VARIABLE ASPECT RATIO- 1

THICKNESS RATIO- VARIABLE ACROSS SPAN

THICKNESS- 12%

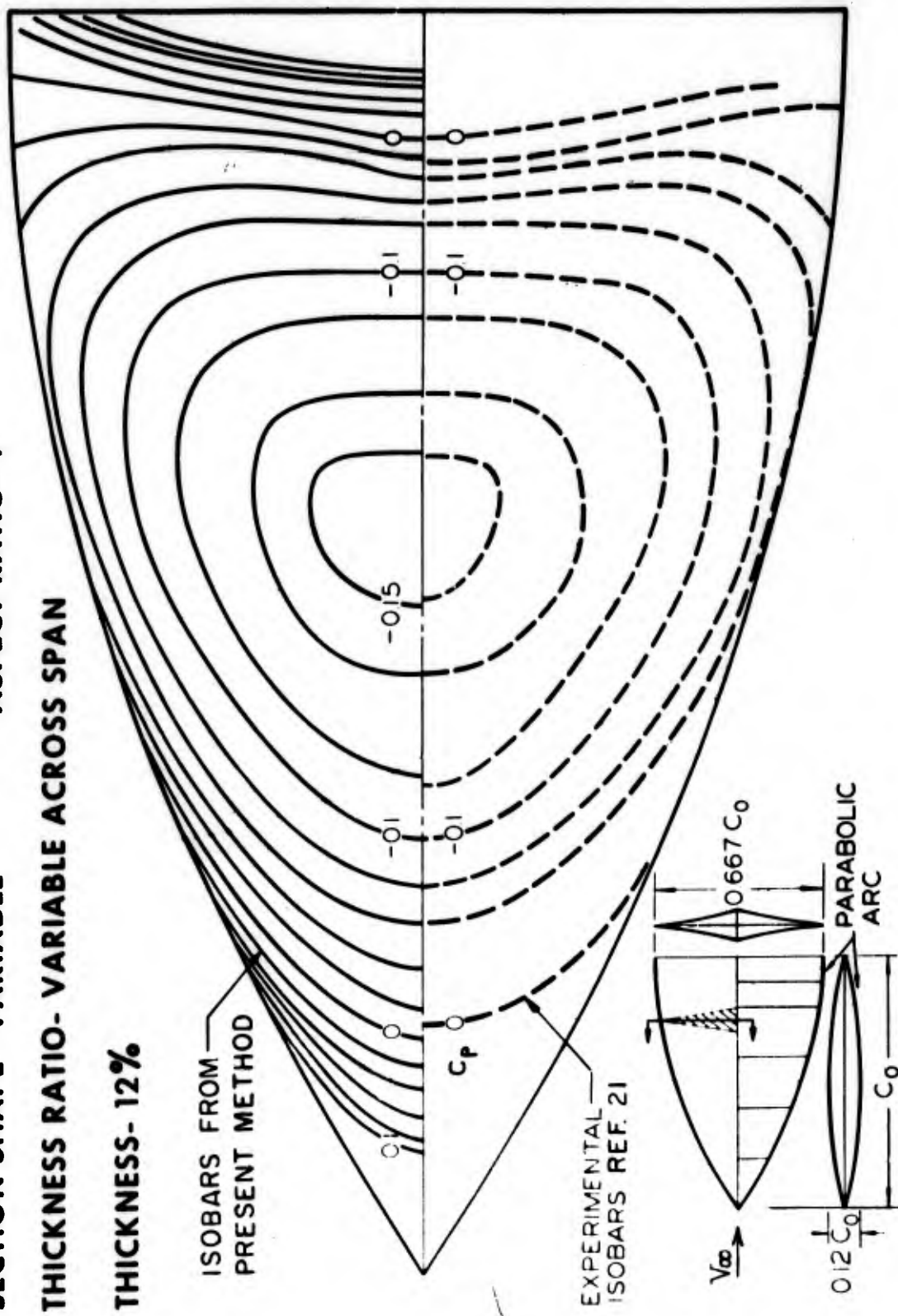


Figure 48. - Comparison of calculated and experimental isobars on Wing A at zero lift.

SECTION SHAPE- CONSTANT ACROSS SPAN ASPECT RATIO- 1
 THICKNESS RATIO- CONSTANT ACROSS SPAN THICKNESS- 12%

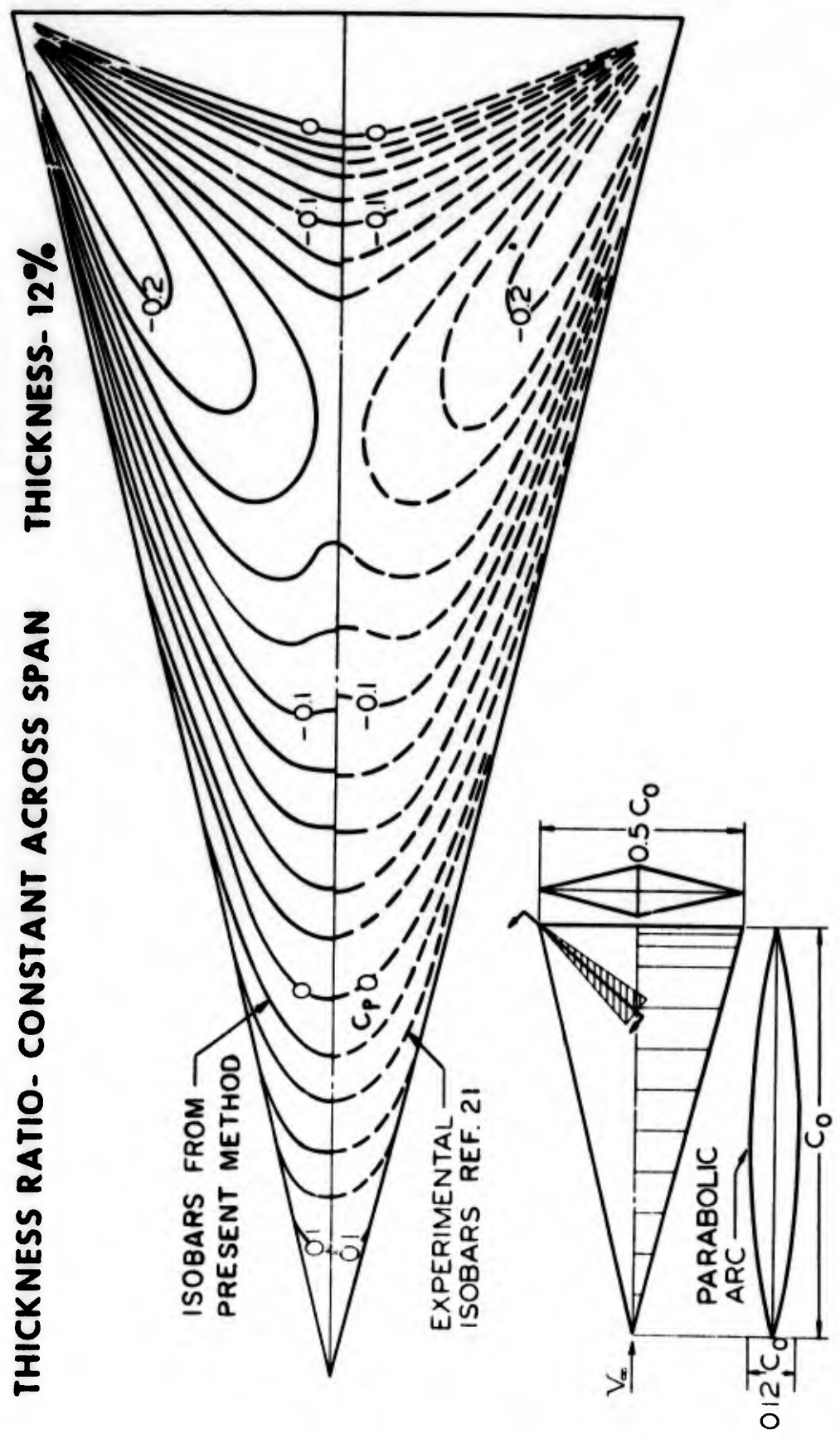


Figure 49.- Comparison of calculated and experimental isobars on Wing B at zero lift.

SECTION SHAPE- CONSTANT ACROSS SPAN ASPECT RATIO- 1
 THICKNESS RATIO- LINEARLY DECREASING THICKNESS- 12%
 ACROSS SPAN

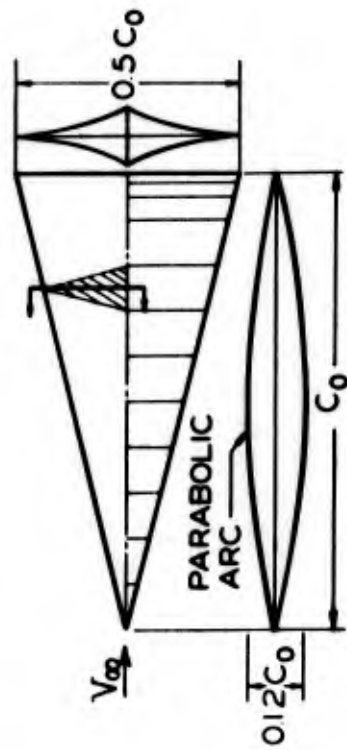
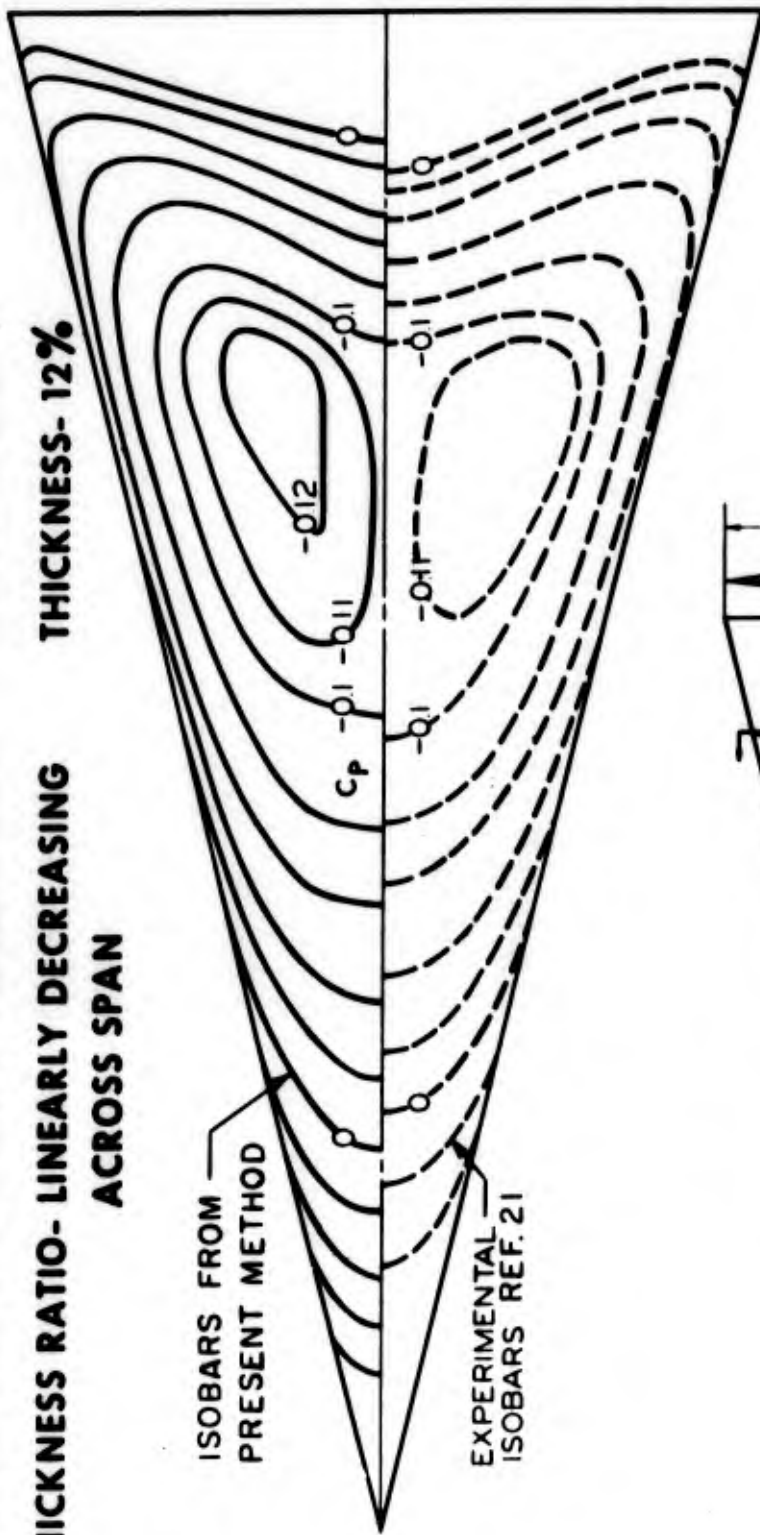


Figure 50. - Comparison of calculated and experimental isobars on Wing C at zero lift.

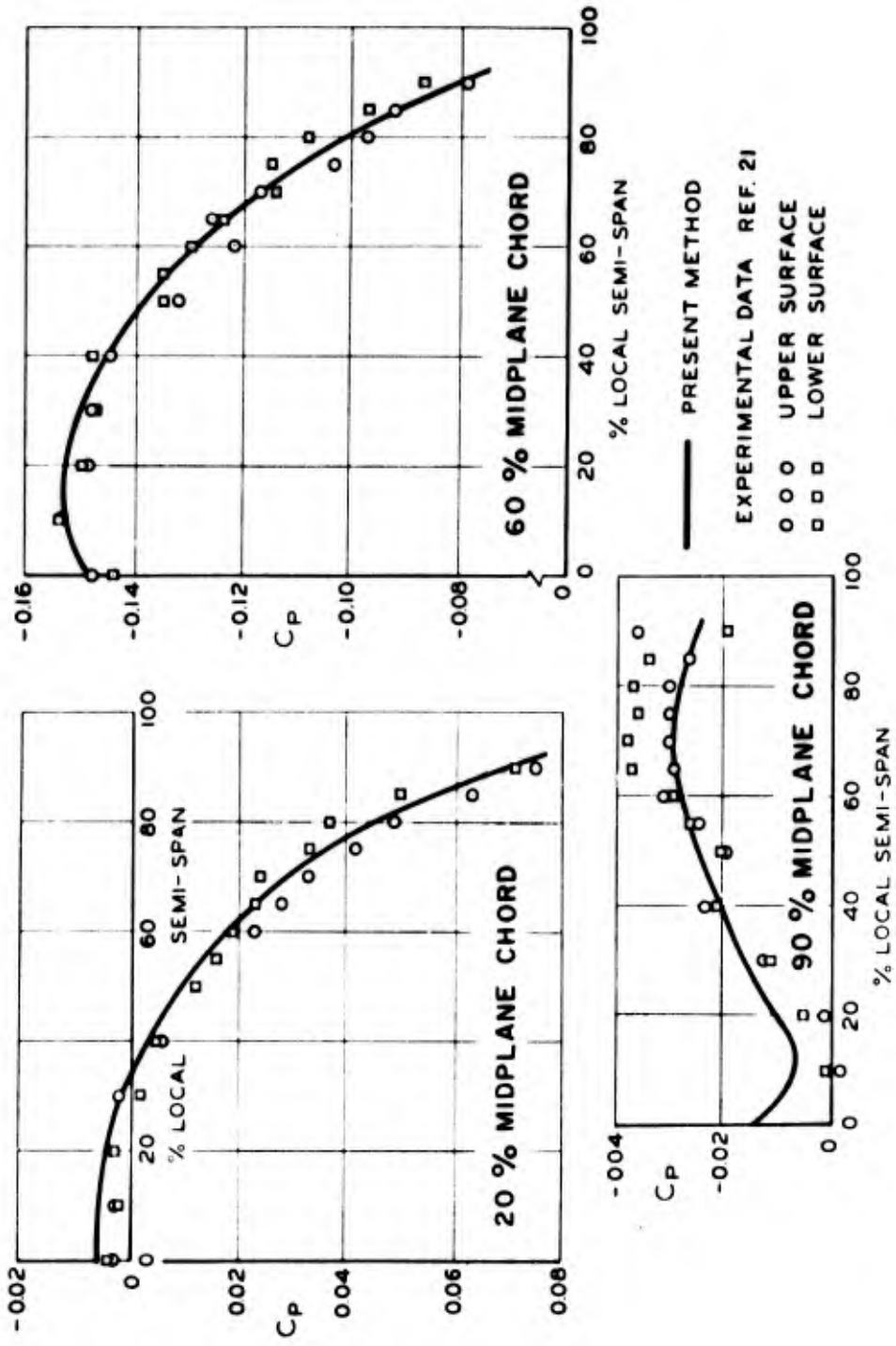


Figure 51. - Comparison of calculated and experimental spanwise pressure distributions on Wing A at zero lift.

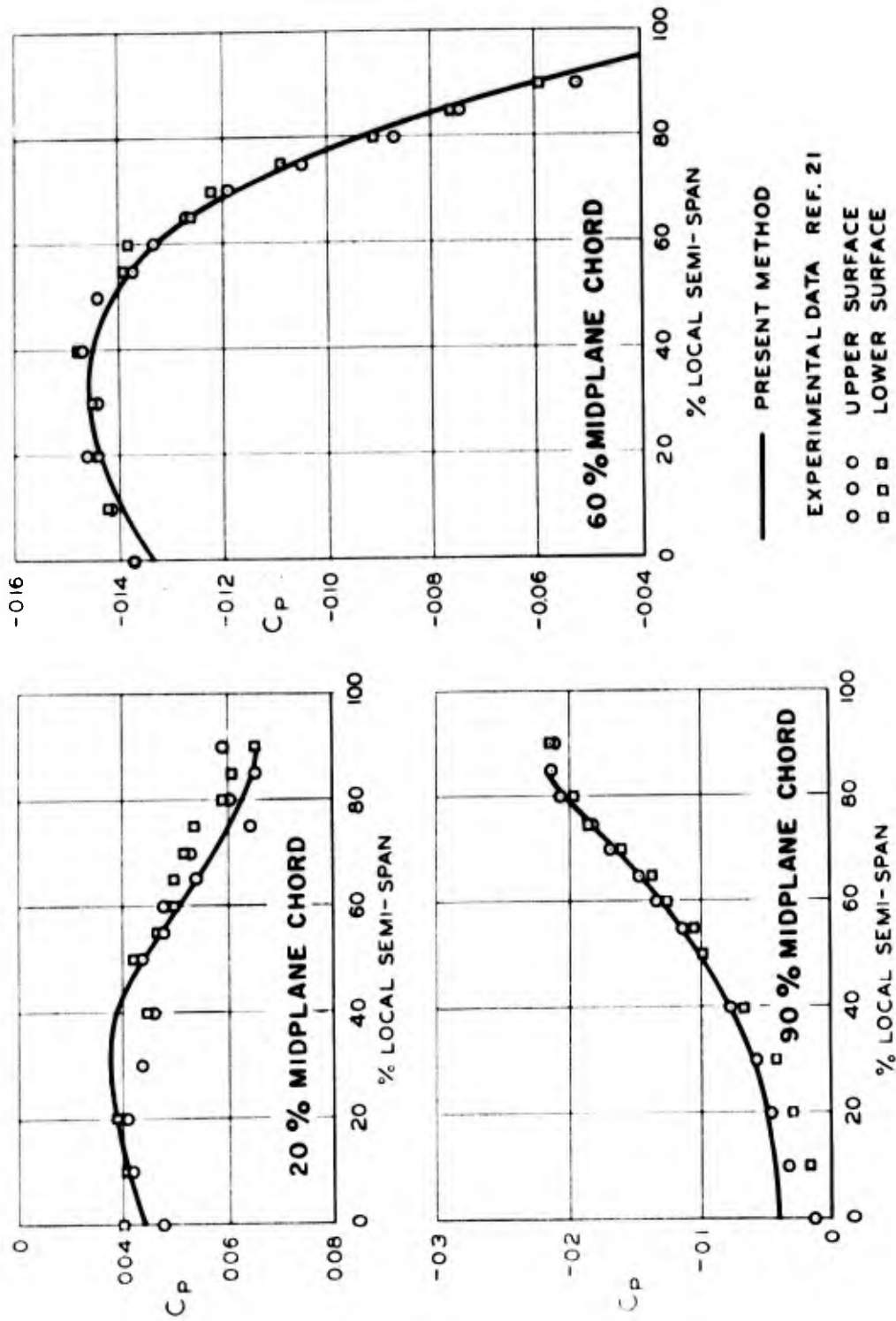


Figure 52. - Comparison of calculated and experimental spanwise pressure distributions on Wing B at zero lift.

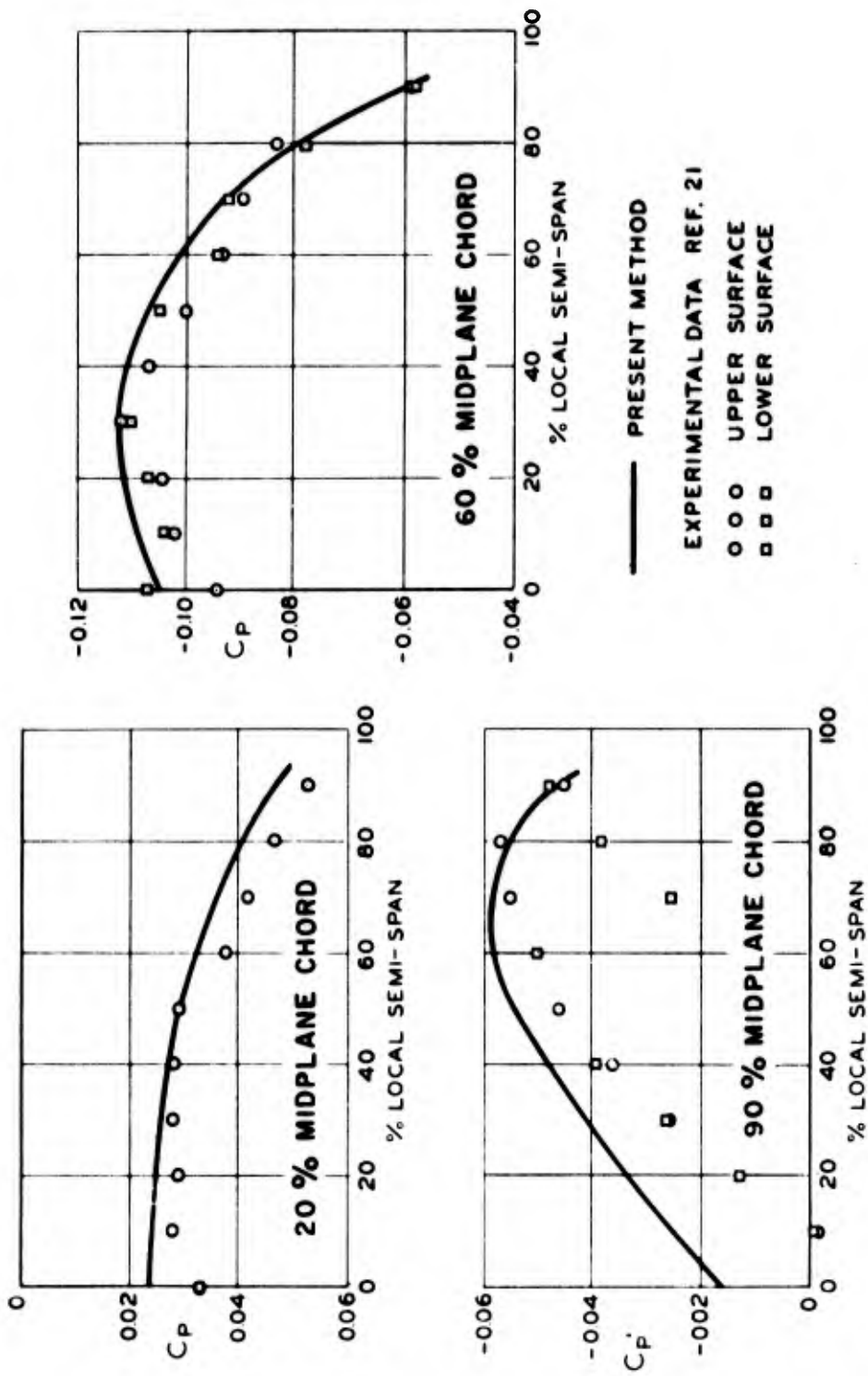


Figure 53. - Comparison of calculated and experimental spanwise pressure distributions on Wing C at zero lift.

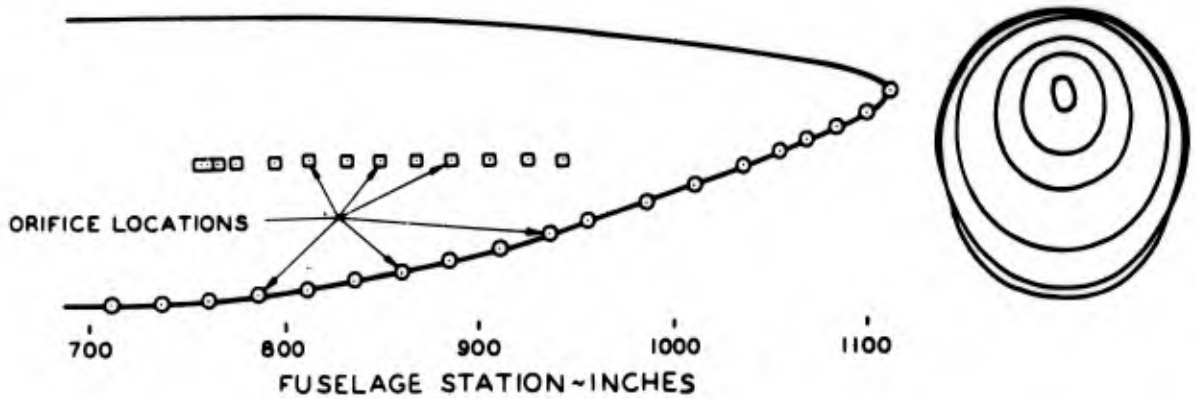
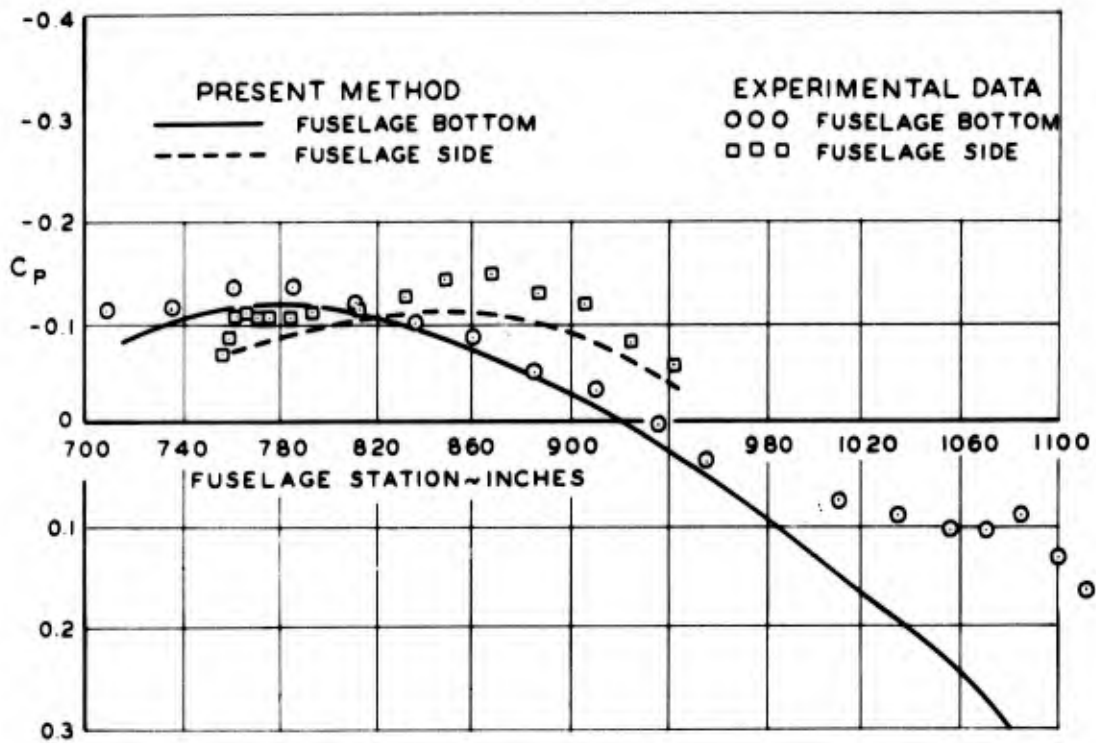


Figure 54. - Comparison of calculated and experimental pressure distributions on the aft end of a clean DC-9 fuselage.

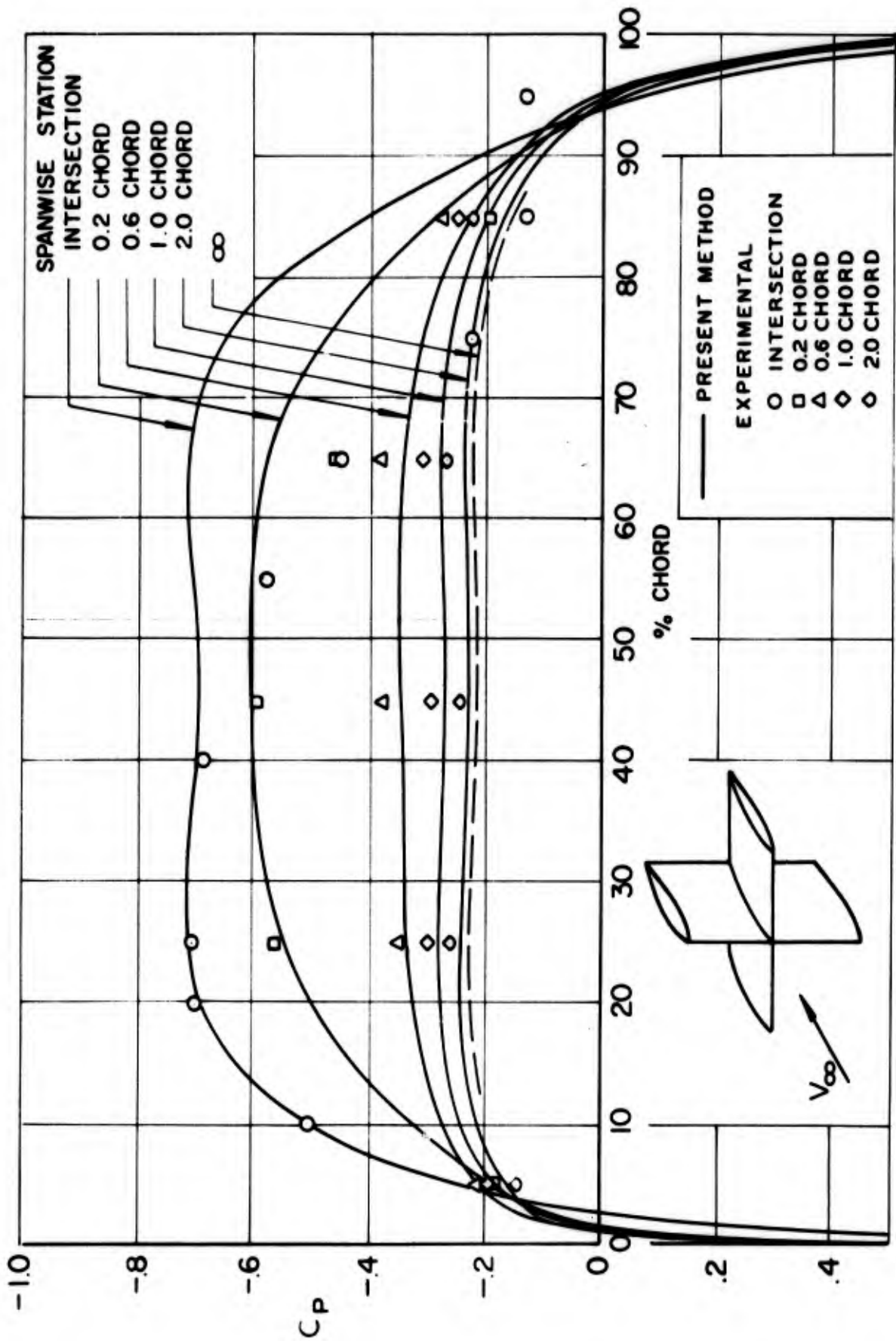


Figure 55. - Comparison of calculated and experimental pressure distributions on a nonlifting symmetric 10 percent-thick wing which intersects a nonlifting symmetric 20 percent-thick wing.

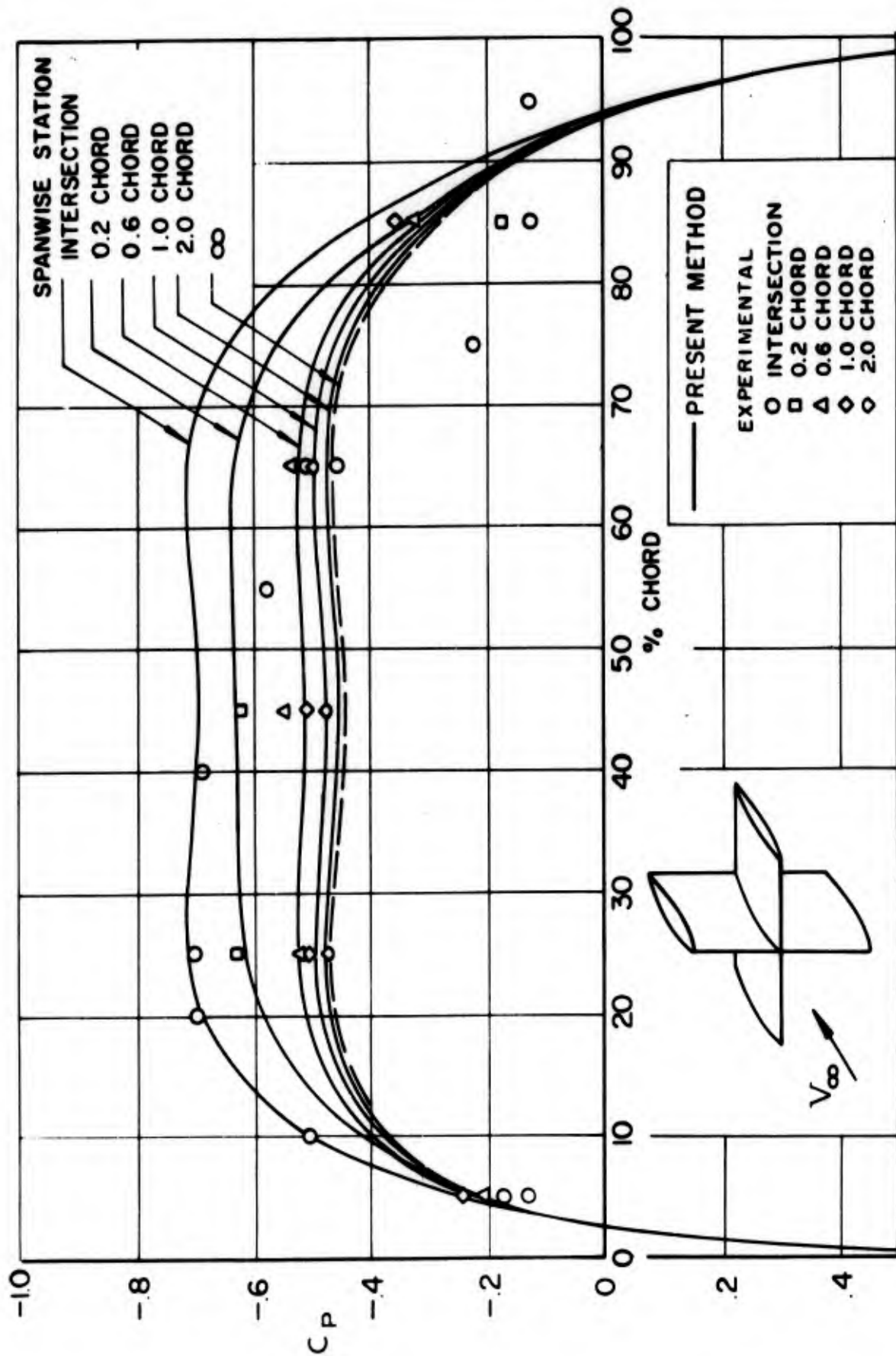


Figure 56. - Comparison of calculated and experimental pressure distributions on a nonlifting symmetric 20 percent-thick wing which intersects a nonlifting symmetric 10 percent-thick wing.

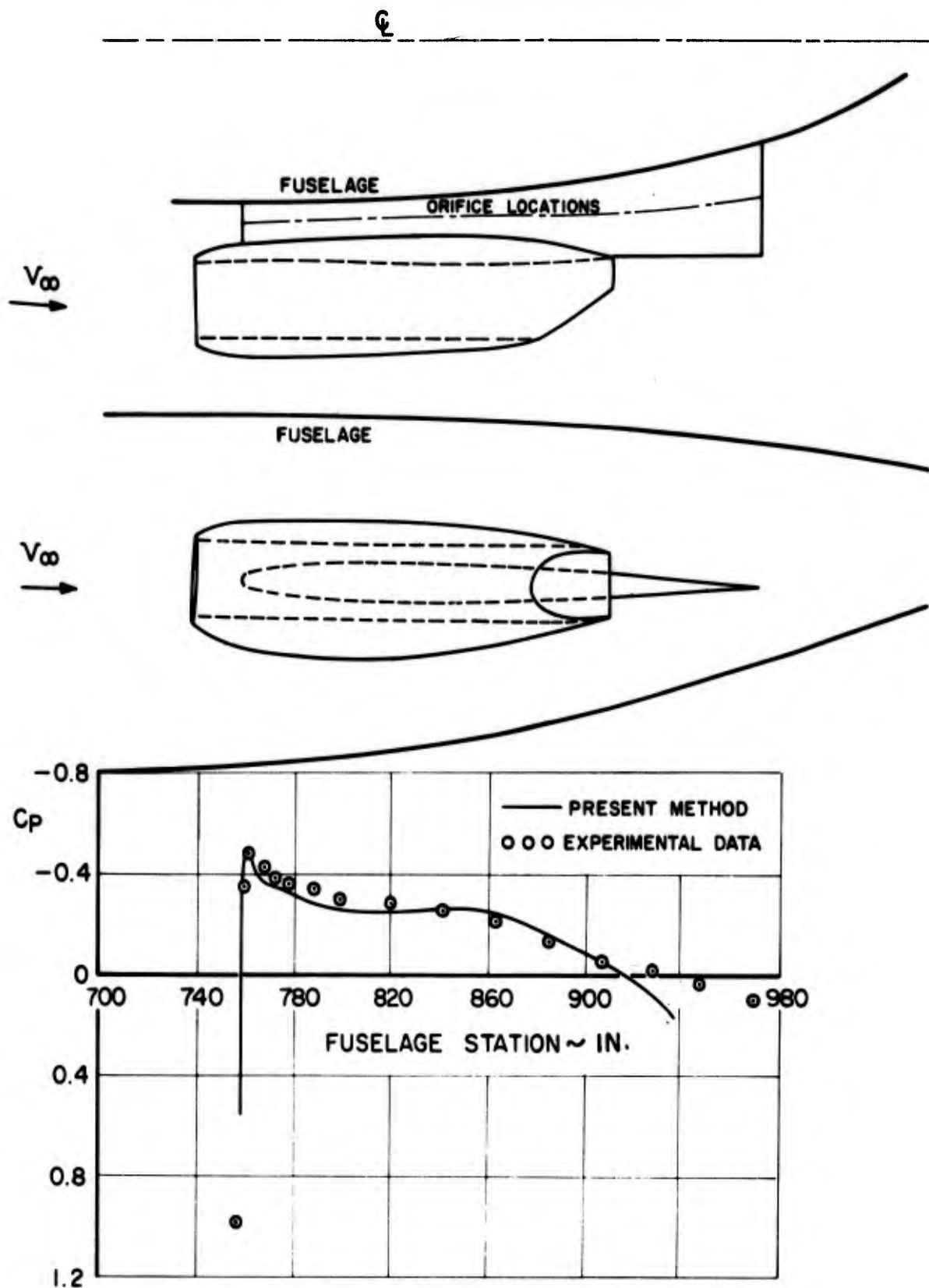


Figure 57. - Comparison of calculated and experimental pressure distributions on a DC-9 pylon in the presence of the fuselage and nacelle.

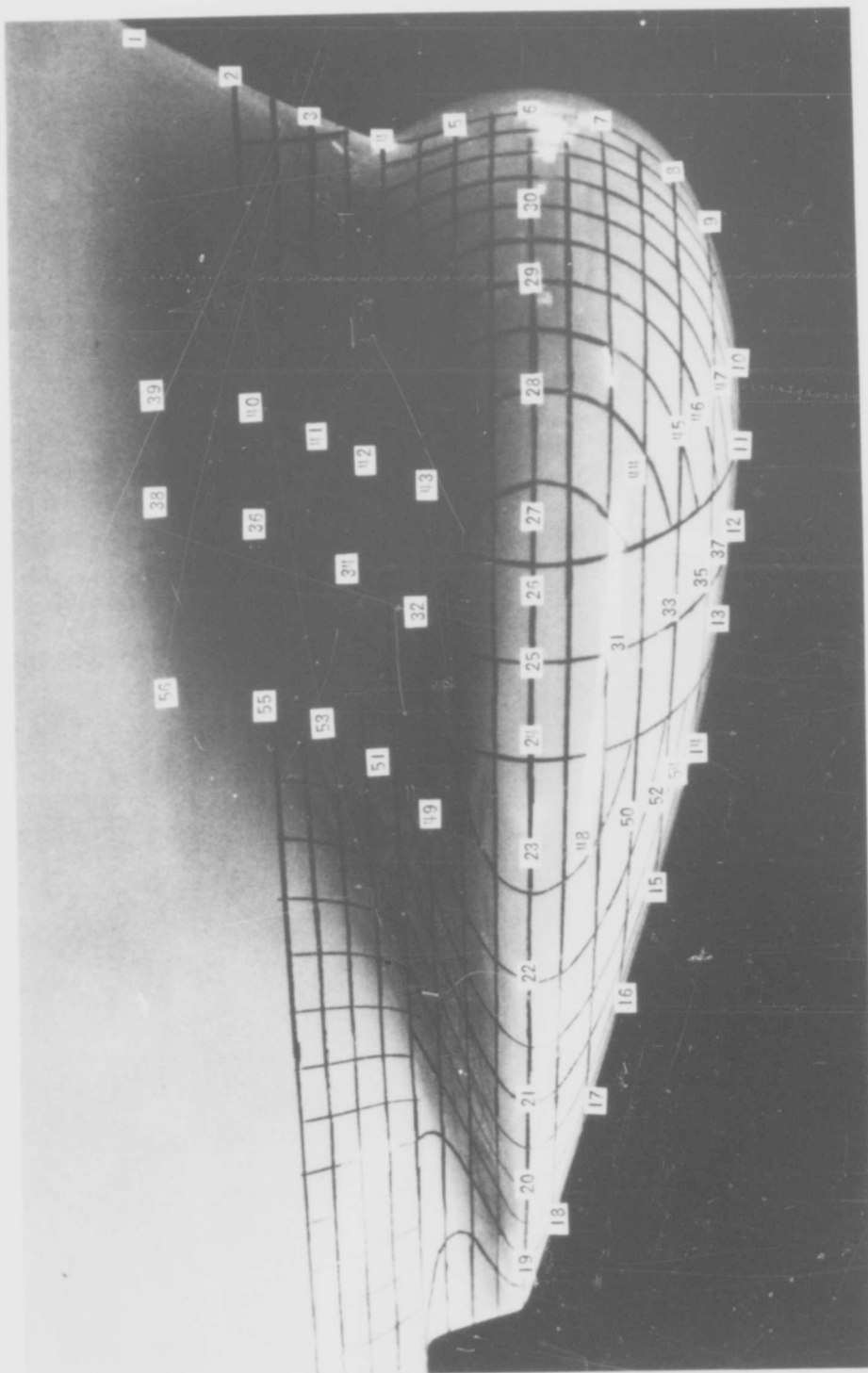


Figure 58.- Destroyer sonar dome showing orifice locations.

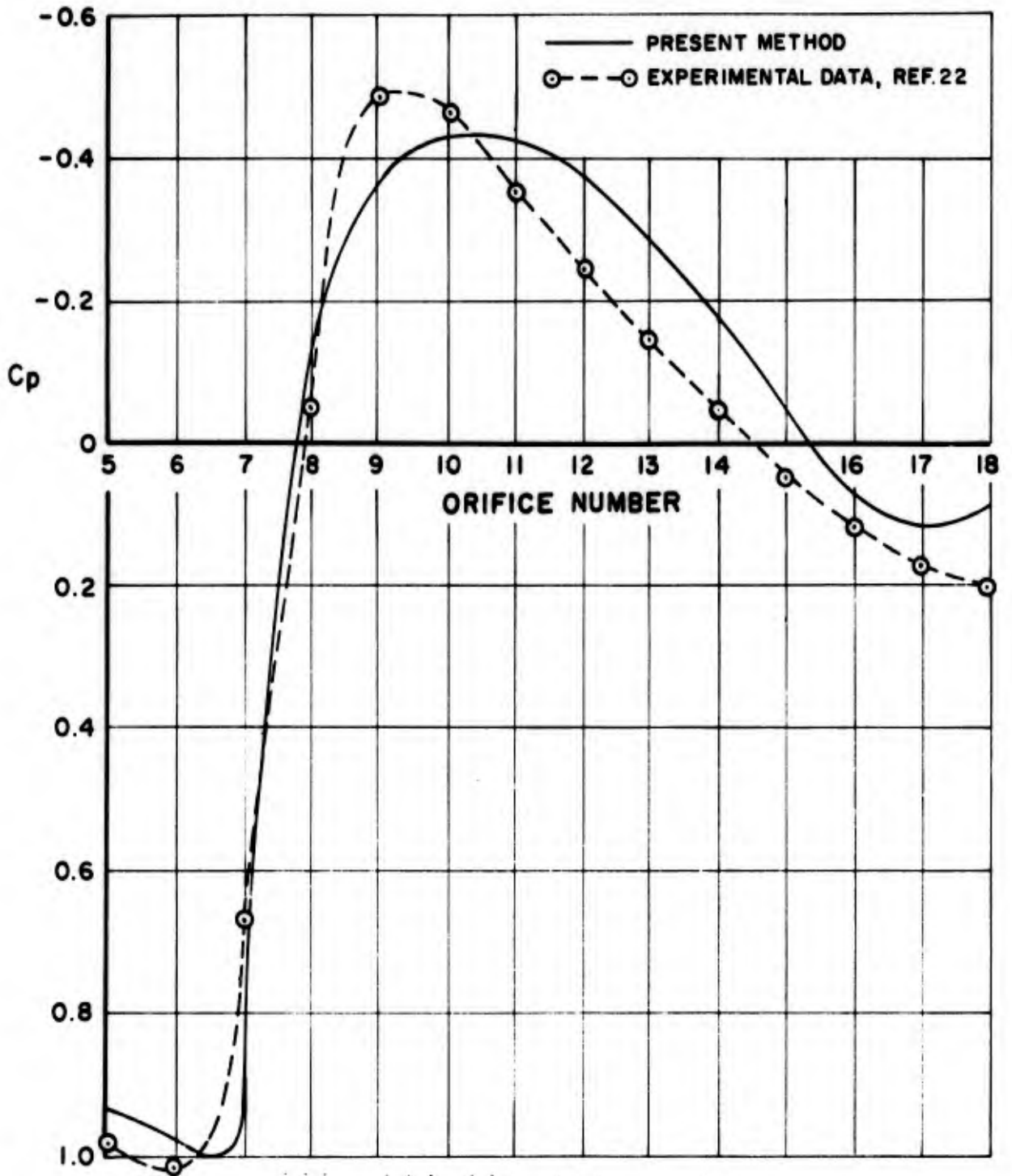


Figure 59. - Comparison of calculated and experimental pressure distributions in the symmetry plane of a destroyer sonar dome.

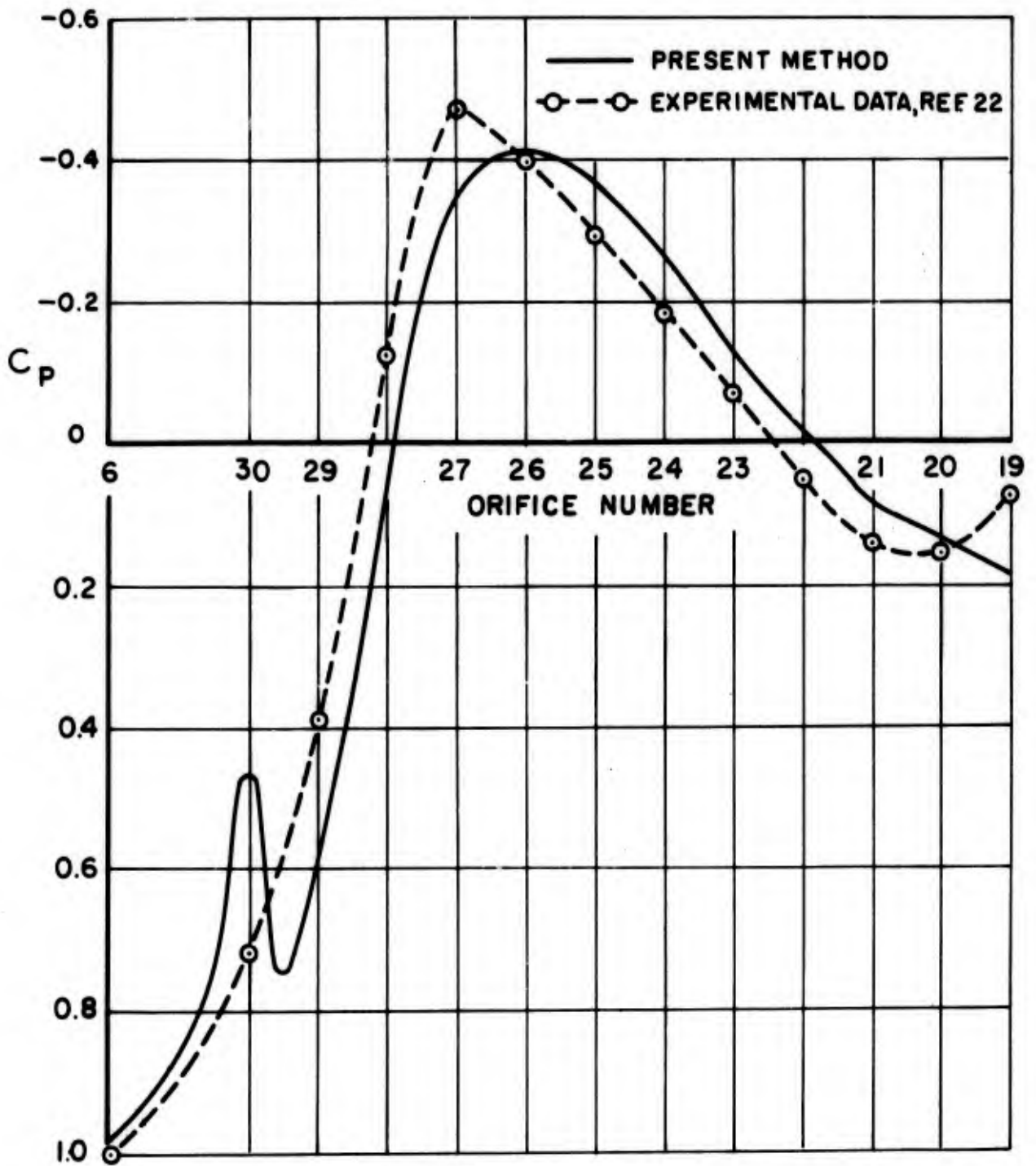


Figure 60. - Comparison of calculated and experimental pressure distributions along the maximum horizontal section of a destroyer sonar dome.

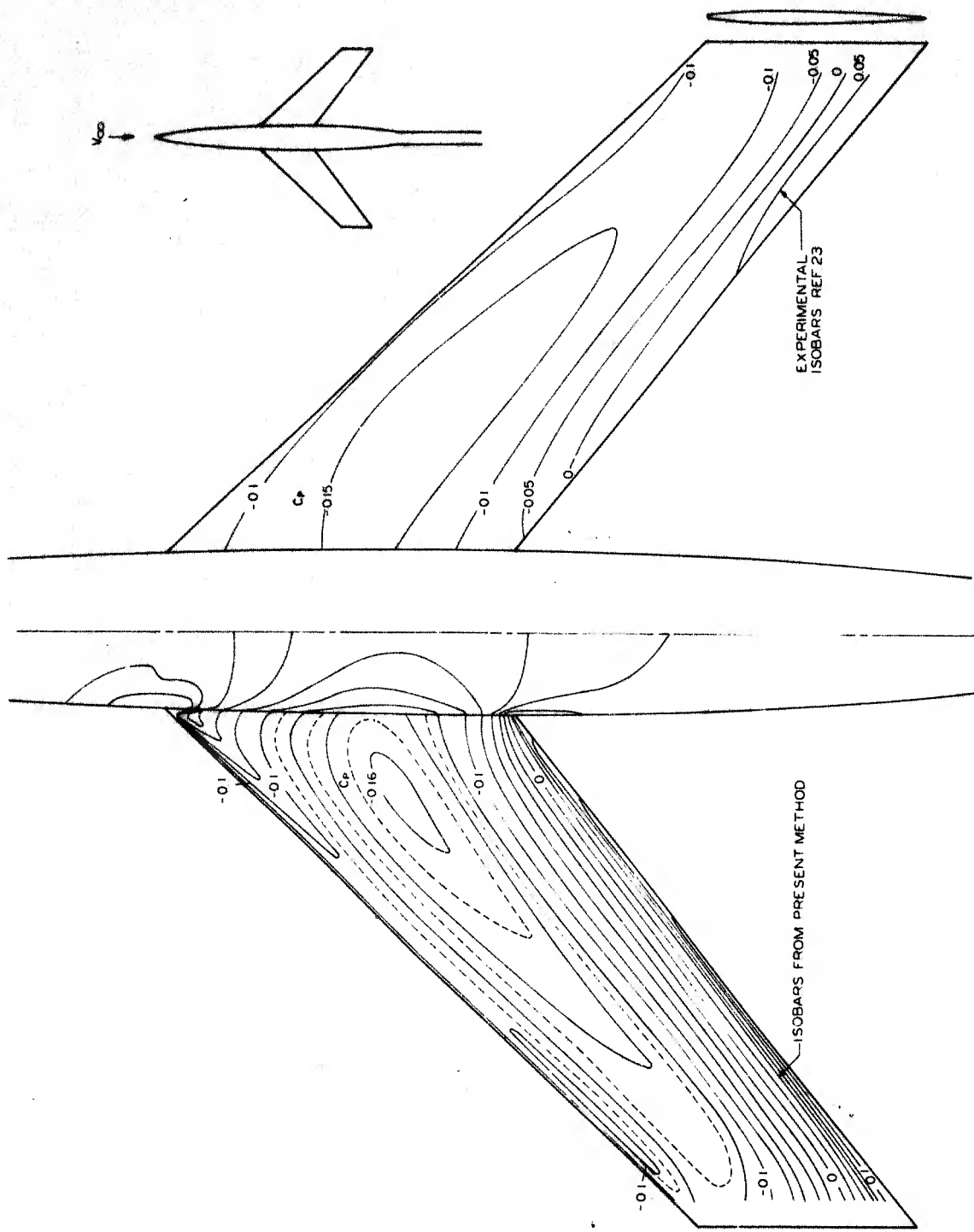


Figure 61. - Comparison of calculated and experimental isobars on an MACA wing mounted on a fuselage at zero lift for a Mach number of 0.6.

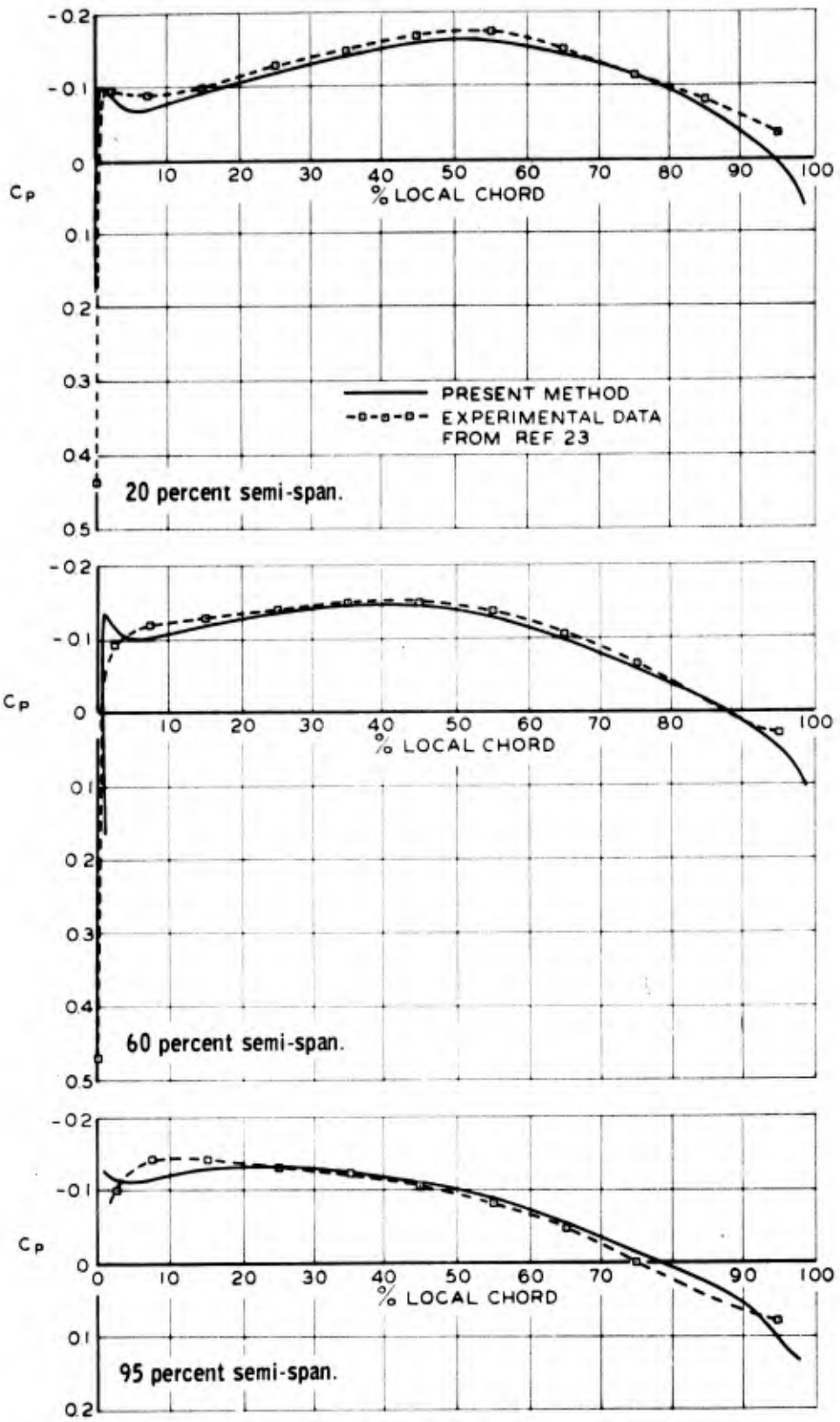


Figure 62. - Comparison of calculated and experimental pressure distributions at three spanwise locations on an NACA wing mounted on a fuselage at zero lift for a Mach number of 0.6.

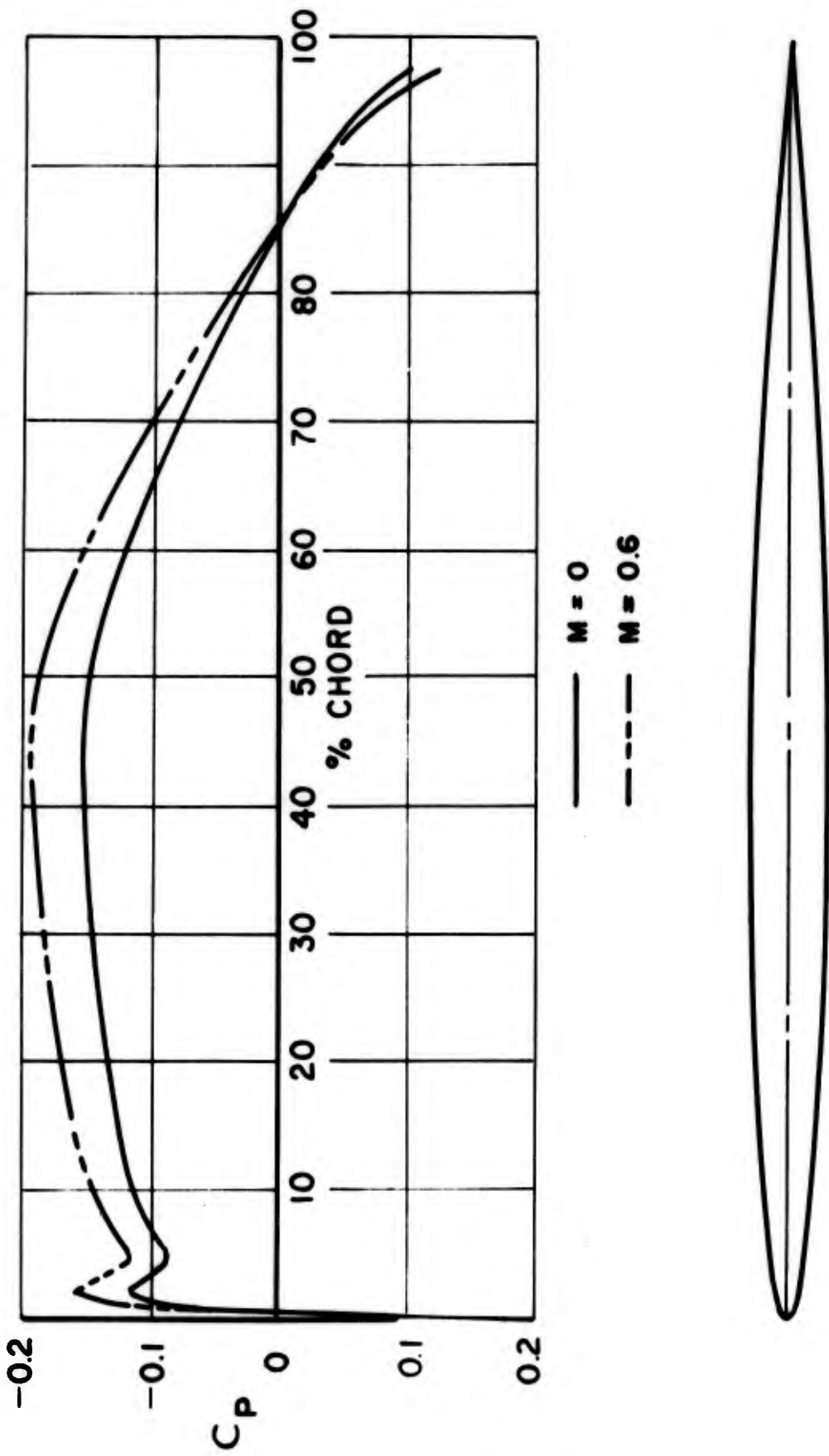


Figure 63. - Calculated two-dimensional pressure distributions on a 6 percent-thick symmetric airfoil at zero lift.

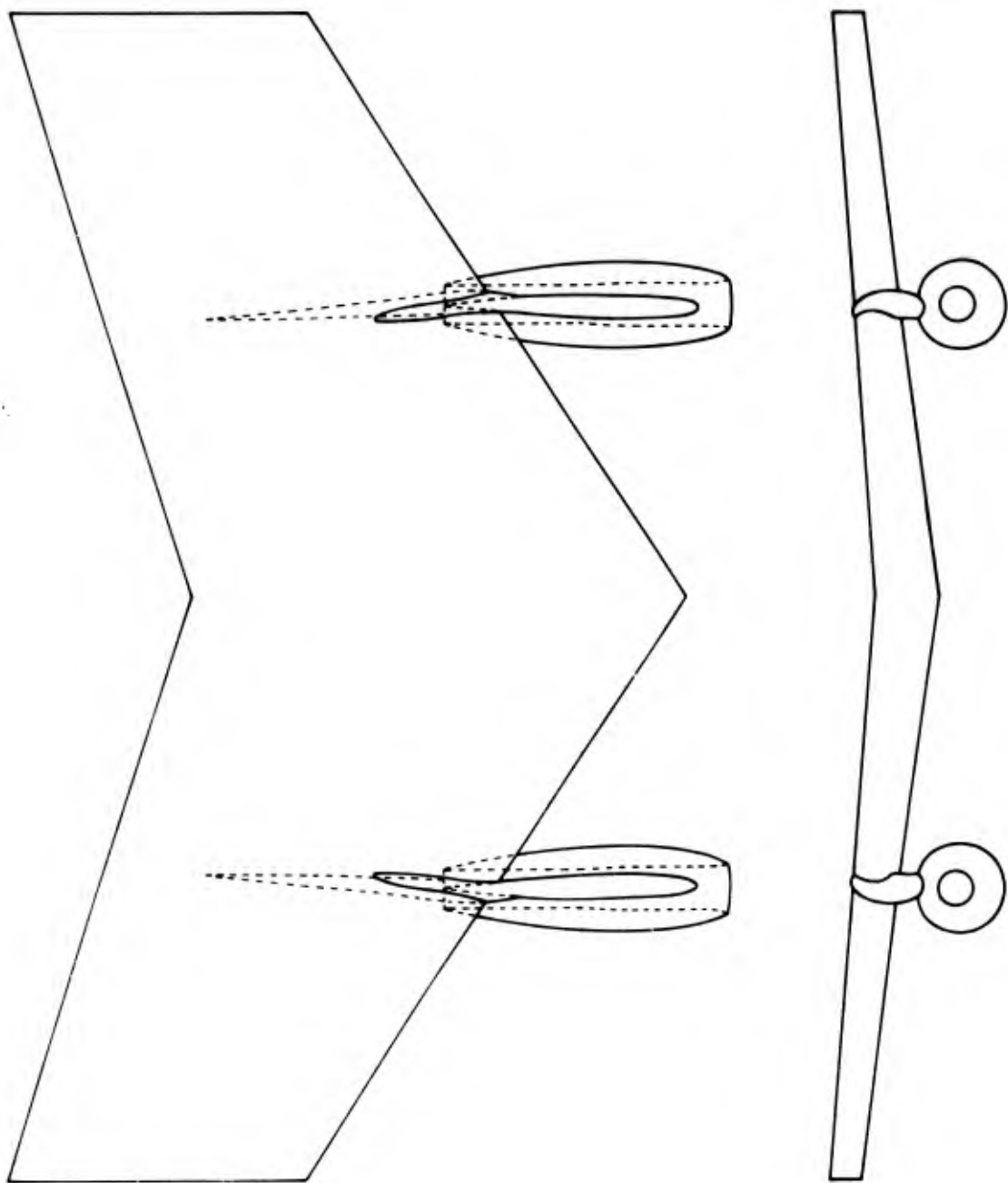


Figure 64.- Adjusted DC-8 wing-pylon-nacelle combination.

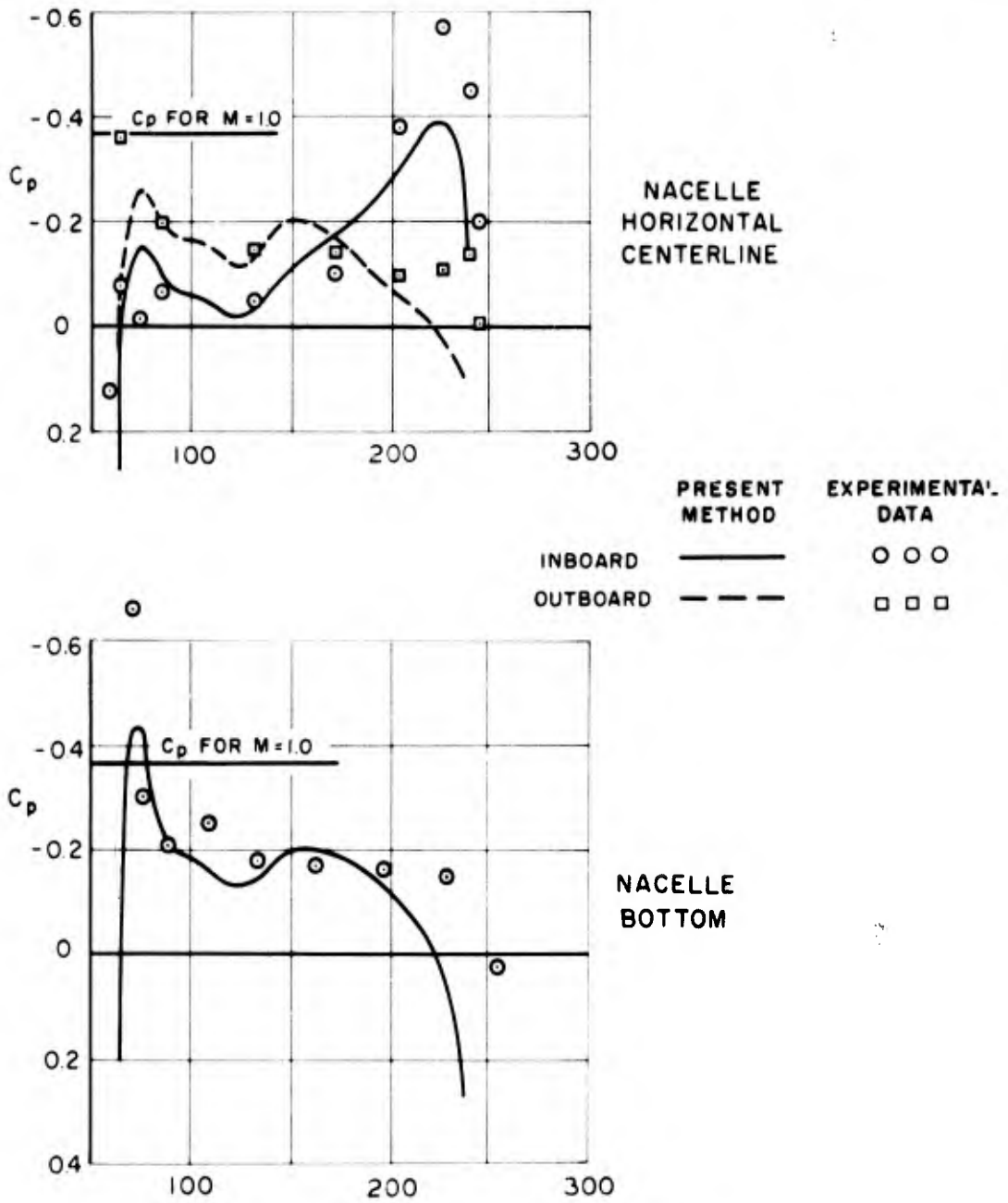
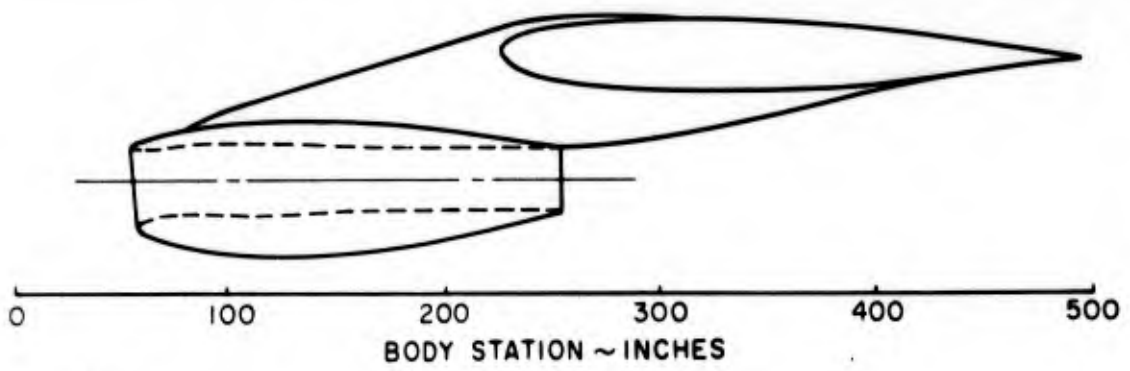


Figure 65. - Comparison of calculated and experimental pressure distributions on a DC-8 nacelle in the presence of the pylon and wing at a Mach number of 0.825 for the zero-lift condition.

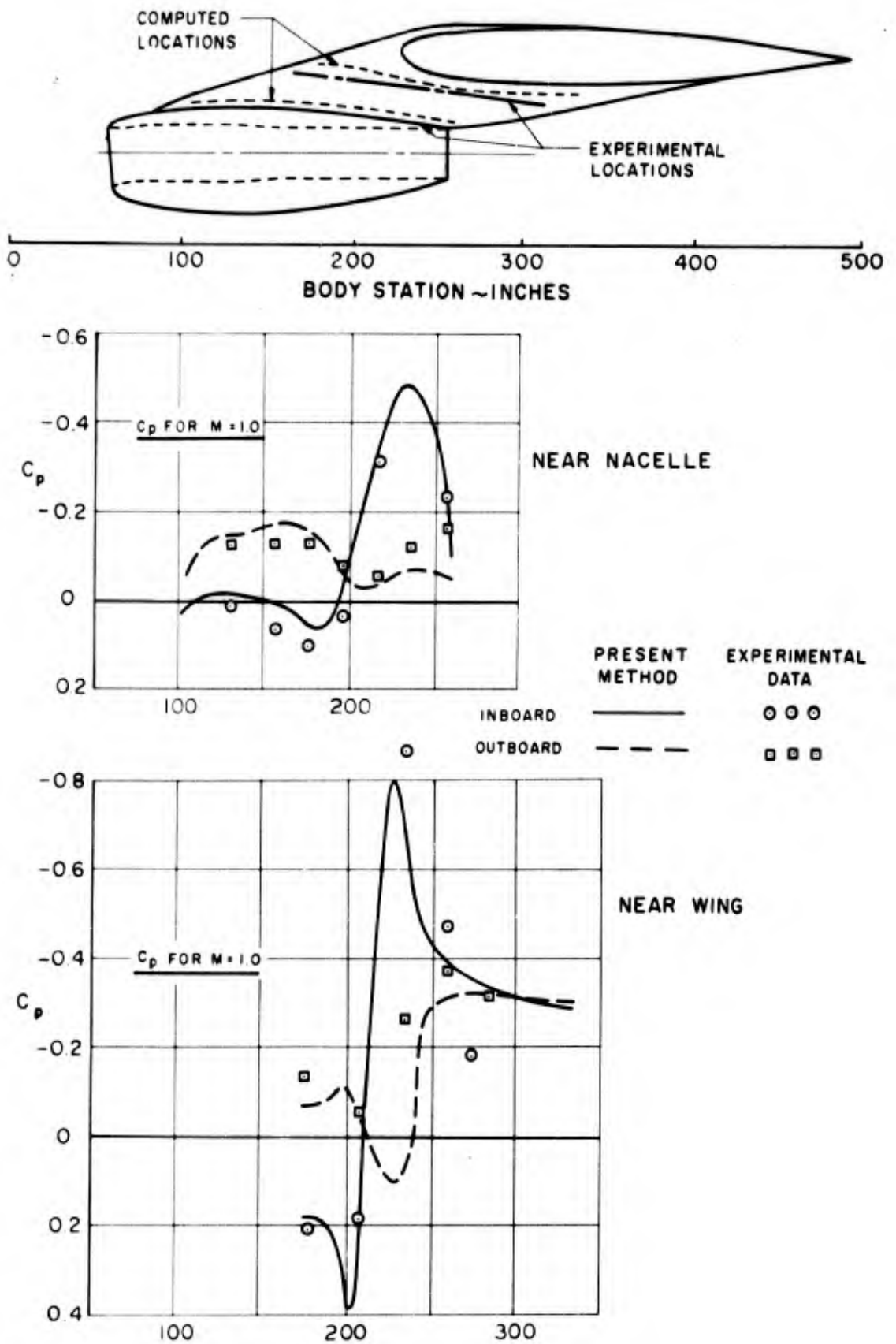


Figure 66. - Comparison of calculated and experimental pressure distributions on a DC-8 pylon in the presence of the nacelle and wing at a Mach number of 0.825 for the zero-lift condition.